

**Design, Formation, and Characterization of
Polymeric Nanoparticles for Drug Delivery**

BY

MAGDALENA SZYMUSIAK

B.S., University of Illinois at Chicago, 2010

THESIS

Submitted as partial fulfillment of the requirements
for the degree of Doctor of Philosophy in Chemical Engineering
in the Graduate College of the
University of Illinois at Chicago, 2016

Chicago, Illinois

Defense Committee:

Ying Liu, Chair and Advisor

Ludwig C. Nitsche

Lewis E. Wedgewood

Ursula Perez-Salas, Physics

Zaijie J. Wang, Biopharmaceutical Sciences

This thesis is dedicated to my husband, Pawel Szymusiak, without whom it would never have been accomplished.

ACKNOWLEDGEMENTS

First of all, I would like to thank my advisor, Dr. Ying Liu for her exceptional guidance and mentorship. She is one of the most inspiring people I have come to know. Her extensive scientific knowledge and very enthusiastic attitude towards research are the most encouraging attributes that have made me quickly delve into my thesis project. What I have experienced and learned from her and being in her research group will certainly benefit my future career.

I would like to thank my thesis committee members, Dr. Ying Liu, Dr. Ludwig C. Nitsche, Dr. Lewis E. Wedgewood, Dr. Zaijie J. Wang, and Dr. Ursula Perez-Salas for their great support, helpful suggestions and discussions during the time of pursuing my Ph.D. degree.

I would like to thank my collaborators, Dr. Zaijie Jim Wang (Biopharmaceutical Sciences, UIC), Dr. Ursula Perez-Salas (Physics, UIC), Dr. Margarita Herrera-Alonso (Materials Science and Engineering, Johns Hopkins University), Dr. James Morrissey (Biochemistry, UIUC), Dr. Stephanie Smith (Biochemistry, UIUC), Dr. Thomas Irving (BioCAT, Argonne National Laboratory), and Dr. Weifeng Shang (BioCAT, Argonne National Laboratory) for the excellent experience of interdisciplinary research.

I would like to thank my labmates, Hao Shen, Vishal Sharma, Alexander Donovan, Ross Ransom, Yuan Zhang, Pin Zhang, Paola Leon Plata, Catalina Mogollon, Joseph Kalkowski, Chang Liu, and Paulina Ciupinski for the incredible lab environment and tremendous help every day.

I also would like to thank my parents, Stanislaw and Stanislaw Rafacz, my siblings, Joanna Rafacz, Zuzanna Deren, and Jakub Rafacz, and my husband, Pawel Szymusiak for their extraordinary love, belief, and support.

The funding comes from National Science Foundation Nanomanufacturing Program (NSF-CMMI-1350731) and the US Army Medical Research and Materiel Command (WQ81XWH-11-2-0021). The animal studies are partially supported by the University of Illinois at Chicago Proof-of-Concept Award.

Magdalena Szymusiak

CONTRIBUTION OF AUTHORS

Two chapters in this thesis use my previously published manuscripts. Chapter 3 represents a published manuscript (Magdalena Szymusiak, Xiaoyu Hu, Paola A. Leon Plata, Paulina Ciupinski, Zaijie Jim Wang, and Ying Liu, Bioavailability of Curcumin and Curcumin Glucuronide in the Central Nervous System of Mice after Oral Delivery of Nano-curcumin, *International Journal of Pharmaceutics*, 2016, doi:10.1016/j.ijpharm.2016.07.027) for which I am the first author and major driver of the research. Xiaoyu Hu, Paola A. Leon Plata, and Paulina Ciupinski assisted me with a few experiments. I generated all figures and tables in the manuscript. My research mentor, Dr. Ying Liu and I composed the manuscript, with editorial contributions from Dr. Zaijie Jim Wang. Chapter 5 represents a published manuscript (Magdalena Szymusiak,* Alexander J. Donovan,* Stephanie A. Smith, Ross Ransom, Hao Shen, Joseph Kalkowski, James H. Morrissey and Ying Liu, Colloidal Confinement of Polyphosphate on Gold Nanoparticles Robustly Activates the Contact Pathway of Blood Coagulation, *Bioconjugate Chemistry*, 27 (1), 102–109, 2016; * these authors contributed equally) for which I am the co-first author. I played a large role in writing the manuscript along with my co-first author, Alexander Donovan, my research mentor, Dr. Ying Liu, our collaborator, Dr. Stephanie A. Smith, and with editorial contributions from Dr. James H. Morrissey. Alexander Donovan and I conceived and conducted most of the experimental procedures and generated the majority of figures for the manuscript (Figure 5-1, 5-2, 5-3, 5-5, and 5-6). Dr. Stephanie Smith performed the experiments involving testing the clotting performance of our nanoparticles by using a mechanical coagulometer and generated Figure 5-4. Ross Ransom, Hao Shen, and Joseph Kalkowski helped with the initial design and some experimental procedures. I also anticipate that some content of Chapter 4 will be ultimately published as a part of a co-authored manuscript

after I leave. I performed the vast majority of the experimental and modeling procedures. The novel brush polymers for the study as well as the NMR and TEM experimental data were provided by our collaborator, Dr. Margarita Herrera Alonso and her student, Hanying Luo.

TABLE OF CONTENTS

ACKNOWLEDGEMENTS	III
CONTRIBUTION OF AUTHORS.....	V
TABLE OF CONTENTS	VII
LIST OF TABLES	IX
LIST OF FIGURES	X
LIST OF ABBREVIATIONS	XIII
SUMMARY	XV
1 INTRODUCTION.....	1
1.1 NANOPARTICLES AS DRUG DELIVERY CARRIERS	1
1.1.1 <i>Encapsulation of Hydrophobic Molecules into Polymeric Nanoparticles to Increase Drug Solubility and Bioavailability.....</i>	3
1.1.1.1 <i>Current Production Methods of Polymeric Nanoparticles Encapsulating Hydrophobic Compounds and Our Process</i>	3
1.1.2 <i>Surface Modification of Nanoparticles for Enhanced Drug Functionality and Targeted Drug Delivery.....</i>	8
1.1.2.1 <i>Prolonging Drug Circulation Time.....</i>	9
1.1.2.2 <i>Enhancing Drug Bioavailability and Functionality.....</i>	10
1.1.2.3 <i>Providing Targeted Drug Delivery.....</i>	10
1.1.3 <i>Characterization Methods of Nanoparticles</i>	12
1.1.3.1 <i>Dynamic Light Scattering (DLS).....</i>	13
1.1.3.2 <i>Transmission Electron Microscopy (TEM)</i>	14
1.1.3.3 <i>Small-angle X-ray and Neutron Scattering (SAXS and SANS).....</i>	15
2 FORMATION OF STABLE POLYMERIC NANOPARTICLES ENCAPSULATING HYDROPHOBIC COMPOUNDS BY FLASH PRECIPITATION AND DRYING (FPAD) PROCESSES	18
2.1 INTRODUCTION	18
2.2 EXPERIMENTAL SECTION.....	21
2.2.1 <i>Materials and Methods</i>	21
2.2.2 <i>Nanoparticle Formation.....</i>	21
2.2.3 <i>Freeze-drying and Spray-drying.....</i>	23
2.2.4 <i>Resuspension of Nanoparticles</i>	23
2.2.5 <i>Nanoparticle Characterization by Dynamic Light Scattering (DLS).....</i>	24
2.3 RESULTS AND DISCUSSION	24
2.4 CONCLUSIONS.....	33
3 BIOAVAILABILITY AND BIOFUNCTIONALITY OF POLYMERIC NANOPARTICLES ENCAPSULATING CURCUMIN	34
3.1 INTRODUCTION	34
3.2 EXPERIMENTAL PROCEDURES	37
3.2.1 <i>Materials and Reagents.....</i>	37
3.2.2 <i>Animals.....</i>	37
3.2.3 <i>Nanoparticle Preparation and Characterization.....</i>	37
3.2.4 <i>Freeze Drying of the Nanoparticle Suspensions and Resuspension of Powders</i>	38

3.2.5	<i>GC-MS Analysis for Residual THF Content in the Dried Powder to Comply with the FDA Regulations</i>	39
3.2.6	<i>Pharmacokinetic Study in Mice</i>	39
3.2.6.1	<i>Plasma and Tissue Collection</i>	39
3.2.6.2	<i>Extraction of Curcumin and Curcumin Glucuronide from Plasma and Tissues</i>	40
3.2.6.3	<i>HPLC and LC-MS Analysis</i>	41
3.3	RESULTS AND DISCUSSION.....	42
3.4	CONCLUSIONS.....	59
4	CHARACTERIZATION OF PHYSICAL STRUCTURES OF POLYMERIC NANOPARTICLES BY USING SMALL ANGLE X-RAY SCATTERING	60
4.1	INTRODUCTION.....	60
4.2	EXPERIMENTAL PROCEDURES.....	62
4.2.1	<i>Materials and Reagents</i>	62
4.2.2	<i>Micelle Formation</i>	62
4.2.3	<i>Dynamic Light Scattering (DLS) Measurements</i>	62
4.2.4	<i>Transmission Electron Microscopy (TEM) Imaging</i>	62
4.2.5	<i>SAXS Measurements</i>	63
4.3	MODELING OF SAXS DATA.....	63
4.4	RESULTS AND DISCUSSION.....	68
4.5	CONCLUSIONS.....	84
5	SURFACE CONJUGATION OF NANOPARTICLES WITH POLYPHOSPHATE	86
5.1	INTRODUCTION.....	86
5.2	EXPERIMENTAL PROCEDURES.....	89
5.2.1	<i>Materials and Reagents</i>	89
5.2.2	<i>Synthesis of PolyP₇₀-Cystamine Ligand</i>	90
5.2.3	<i>Conjugation of PolyP₇₀-Cystamine to GNPs</i>	90
5.2.4	<i>Removal of Unreacted PolyP₇₀</i>	91
5.2.5	<i>Determination of Number of PolyP₇₀ Chains per Particle</i>	92
5.2.6	<i>Transmission Electron Microscopy (TEM)</i>	93
5.2.7	<i>Zeta (ζ) Potential Measurements</i>	93
5.2.8	<i>Clotting Assays</i>	93
5.2.9	<i>A₄₀₅ Turbidity Measurements</i>	94
5.3	RESULTS AND DISCUSSION.....	94
5.4	CONCLUSIONS.....	110
6	CONCLUSIONS	112
	REFERENCES	114
	APPENDIX	122
	VITA	124

LIST OF TABLES

Table 2-1. Conditions of polymeric curcumin nanoparticles.	22
Table 2-2. Resuspension of PLGA-curcumin (1:1) nanoparticles after being freeze-dried with different amounts of excipients. The size of the nanoparticles was determined after resuspending them at low (<20 mg/ml) or high (600 mg/ml) construct concentration. Average diameter of the nanoparticles immediately after formation before freeze-drying was 100.1 nm.	28
Table 2-3. The FPaD process parameters and size distribution of nanoparticles encapsulating a variety of small and large MW hydrophobic compounds.	32
Table 3-1. Quality-control samples for extraction of curcumin from plasma, brain, and spinal cord with ethyl acetate.	47
Table 3-2. Quality-control samples for extraction of curcumin glucuronide from plasma, brain, and spinal cord with acetonitrile.	48
Table 3-3. Pharmacokinetic parameters of curcumin levels in plasma, brain, and spinal cord after oral delivery of nano-curcumin (20 mg/kg) and pure curcumin suspensions (20 mg/kg and 400 mg/kg).	52
Table 3-4. Pharmacokinetic parameters for curcumin glucuronide in plasma after oral administration of low-dose (20 mg/kg) nano-curcumin, low-dose (20 mg/kg) pure curcumin, and high-dose (400 mg/kg) pure curcumin.	57
Table 4-1. Percentage of PEG on the surface of micelles by NMR.	66
Table 4-2. Scattering length densities (SLDs) of water and polymers.	67
Table 4-3. Linear and brush polymers and the corresponding nanoparticle information.	70
Table 4-4. Parameters obtained from fitting the SAXS data into the core-shell sphere model.	75
Table 4-5. Parameters obtained from fitting the SAXS data of brush amphiphilics into the core-shell models.	82
Table 5-1. Experimental conditions for conjugation of polyP ₇₀ -cystamine to GNPs.	91
Table 5-2. Size-dependent centrifugation conditions.	92
Table 5-3. Conjugation efficiency of polyP ₇₀ and cystamine at various pH conditions.	96
Table 5-4. Free cystamine concentration (μ M) before and after pH adjustment.	96
Table 5-5. Synthesized polyP ₇₀ -GNPs.	101
Table 5-6. Zeta (ζ) Potential measurements of the synthesized samples.	105

LIST OF FIGURES

Figure 1-1. The examples of leading (A) organic and (B) inorganic nanocarrier platforms.....	2
Figure 1-2. The general FPaD process of producing polymeric nanoparticles encapsulating hydrophobic compounds for <i>in vivo</i> and <i>in vitro</i> studies. Nanosuspensions are generated via flash nanoprecipitation in the multi inlet vortex mixer (MIVM). The nanoparticles are further freeze- or spray-dried together with excipients to obtain stable and dried product that can be conveniently resuspended at desired time and concentration for <i>in vitro</i> or <i>in vivo</i> animal studies.	8
Figure 1-3. Surface modification of gold nanoparticles with polyphosphate (polyP) for enhanced drug functionality and targeted drug delivery.	12
Figure 1-4. General schematic of small-angle x-ray (SAXS) technique.....	17
Figure 2-1. Molecular structures of the main model hydrophobic compound, curcumin, and the polymers investigated in the study.	20
Figure 2-2. Molecular structures of the compounds used in this thesis study. (A) N1-(3-chlorophenyl)-2-cycloheptylidenehydrazine-1-carbothioamide (BTB05119). (B) 2-chlorobenzaldehyde 1-(4-phenyl-1,3-thiazol-2-yl)hydrazone hydrochloride (ML00176). (C) Myr-FEEERA. (D) Ecumicin.....	21
Figure 2-3. Schematic representation of a multi-inlet vortex mixer (MIVM).	22
Figure 2-4. (A) Size distribution of PEG- <i>b</i> -PLA-curcumin nanoparticles immediately after mixing. (B) Size distribution of PLGA-curcumin nanoparticles immediately after mixing. (B) Growth kinetics of polymeric nanoparticles encapsulating curcumin.	26
Figure 2-5. Resuspension of PLGA-curcumin NPs at high concentration via (A) vortexing for 10 minutes and (B) bath sonication for 10minutes.	31
Figure 2-6. Lognormal size distribution of nanoparticles right after mixing in the MIVM (AM), and resuspended after freeze drying (AF) and spray drying (AS).	31
Figure 3-1. (A)The size distribution of nano-curcumin before, resuspended right after, and resuspended 16 months after freeze-drying (FD). (B) Nano-curcumin in powder format.....	43
Figure 3-2. GC-MS analysis of THF. (A) Representative chromatogram for THF standard with 0.1 % concentration in water. (B) Representative chromatogram for resuspended nanoparticle in water. The construct concentration was 420 mg/ml. The drug concentration was 1 mg/ml. (C) Linearity of the calibration standards. (D) Comparison between calculated value of THF content per applied daily dose in mice and the permitted daily exposure.	43
Figure 3-3. Examples of calibration curves with and without IS for curcumin (A, B) and curcumin glucuronide (C, D) standards extracted from plasma.	46
Figure 3-4. Quantification of curcumin in plasma using internal and external calibrations. No significant differences were observed.	47
Figure 3-5. Representative chromatograms of curcumin extracted from (A) brain and (B) spinal cord. The top one (in red) is the chromatogram of blank tissues. The middle one (in blue) is the chromatogram of curcumin extracted from tissues spiked with curcumin standard. The bottom one (in green) is the chromatogram of curcumin extracted from tissue samples 15 minutes after oral delivery of low-dose (20 mg/kg) nano-curcumin. The analysis uses ion transition for curcumin (367.1>216.9).....	50
Figure 3-6. The amount of curcumin measured in (A) brain, (B) spinal cord, and (C) plasma after oral administration of low-dose (20 mg/kg) nano-curcumin (black symbols and lines), low-dose (20 mg/kg) pure curcumin (blue symbols and lines), and high-dose (400 mg/kg) pure curcumin (red symbols and lines). All values are reported as the mean \pm S.E.M (n=4).	54
Figure 3-7. Identification of the major curcumin metabolite in plasma. (A) Detection of curcumin glucuronide by negative and positive ionization. (B) Confirmation of the molecular weight by the accurate mass calculator.	55
Figure 3-8. (A) MS/MS spectrum of curcumin glucuronide showing precursor to product ion transition. (B) The amount of curcumin glucuronide measured in plasma after oral administration of low-dose (20 mg/kg) nano-curcumin, low-dose (20 mg/kg) pure curcumin and high-dose (400 mg/kg) pure curcumin. All values are reported as the mean \pm S.E.M (n=4). (C) Representative chromatograms for	

blank plasma, blank plasma spiked with curcumin glucuronide standard, and plasma, brain and spinal cord tissue samples collected 15 minutes after oral delivery of low-dose (20 mg/kg) nano-curcumin. The analysis used ion transition for curcumin glucuronide (543.1>175).....	56
Figure 4-1. Molecular structures of the main types of polymers used in the study and their schematic representations.....	69
Figure 4-2. Size distribution (measured by the DLS) of polymeric micelles formed from linear diblock copolymers. The diameters were volume weighted.	71
Figure 4-3. Size distribution of polymeric micelles formed from polymeric brushes. The measurements were performed by using the DLS and the diameters were volume weighted.	72
Figure 4-4. (A) SAXS data and model fitting for PEG ₁₁₄ - <i>b</i> -PCL ₃₂ . (B) The corresponding $p(r)$ distribution function for PEG ₁₁₄ - <i>b</i> -PCL ₃₂ . (C) SAXS data and model fitting for PEG ₁₁₄ - <i>b</i> -PLA ₅₃ . (D) The corresponding $p(r)$ distribution function for PEG ₁₁₄ - <i>b</i> -PLA ₅₃	73
Figure 4-5. (A) SAXS data and model fitting for PEG ₄₅ - <i>b</i> -PLA ₁₆₉ . (B) The corresponding $p(r)$ distribution function for PEG ₄₅ - <i>b</i> -PLA ₁₆₉ . (C) SAXS data and model fitting for PEG ₇₅ - <i>b</i> -PLA ₁₆₇ . (D) The corresponding $p(r)$ distribution function for PEG ₇₅ - <i>b</i> -PLA ₁₆₇	74
Figure 4-6. (A) SAXS data and model fitting for PGMA ₆₈ - <i>g</i> -PEG ₁₆ /PLA ₁₇ nanoparticles produced at 0.2wt% polymer starting concentration. (B) The corresponding distance distribution function $p(r)$. 76	
Figure 4-7. (A) SAXS data and model fitting for PGMA ₇₂ - <i>g</i> -PEG ₄₅ /PLA ₃₃ nanoparticles produced at 0.27 wt% polymer starting concentration. (B) The corresponding $p(r)$ distribution function of (A). (C) SAXS data and model fitting for PGMA ₇₂ - <i>g</i> -PEG ₄₅ /PLA ₃₃ nanoparticles produced at 2 wt% polymer starting concentration. (D) The corresponding $p(r)$ distribution function of (C).	77
Figure 4-8. (A) SAXS data and model fitting for PGMA ₇₂₁ - <i>g</i> -PEG ₄₅ /PLA ₂₉ nanoparticles produced at 0.27 wt% polymer starting concentration. (B) The corresponding $p(r)$ distribution function of (A). (C) SAXS data and model fitting for PGMA ₇₂₁ - <i>g</i> -PEG ₄₅ /PLA ₂₉ nanoparticles produced at 2 wt% polymer starting concentration. (D) The corresponding $p(r)$ distribution function of (C).	79
Figure 4-9. (A) SAXS data and model fitting for PGMA ₆₄ - <i>r</i> -(PPEG ₂₂ Ma) ₅ nanoparticles produced at 0.27 wt% polymer starting concentration. (B) The corresponding $p(r)$ distribution function of (A). (C) SAXS data and model fitting for PGMA ₆₄ - <i>r</i> -(PPEG ₂₂ Ma) ₅ nanoparticles produced at 2 wt% polymer starting concentration. (D) The corresponding $p(r)$ distribution function of (C).	81
Figure 4-10. Typical TEM images of (A) PGMA ₆₈ - <i>g</i> -PEG ₁₆ /PLA ₁₇ , (B) PGMA ₇₂ - <i>g</i> -PEG ₄₅ /PLA ₃₃ , and (C) PGMA ₇₂₁ - <i>g</i> -PEG ₄₅ /PLA ₂₉ micelles.	83
Figure 4-11. Comparison of the micelle sizes measured by the SAXS and by the DLS.	84
Figure 5-1. The process of synthesizing GNPs conjugated with polyP ₇₀ . (A) PolyP ₇₀ is conjugated to cystamine. (B) PolyP ₇₀ -cystamine is attached to the surface of GNPs.....	95
Figure 5-2. Control centrifugation experiments for 10nm GNPs: (A) Percent GNP recovery after one time (1x) centrifugation of a mixture of polyP ₇₀ at different concentrations (100 mM, 50 mM, and 5 mM) with 10nm GNPs. (B) Percent polyP ₇₀ removed after single centrifugation (1x). The values are reported as the mean \pm S.E. (n=3).	99
Figure 5-3. Typical transmission electron micrographs of 10nm polyP ₇₀ -GNPs. (A) polyP ₇₀ -GNPs are spherical and largely free of aggregation several days after synthesis. Scale bar: 20nm. (B) A trio of polyP ₇₀ -GNPs with the crystal lattices very apparent. Scale bar: 2nm.....	100
Figure 5-4. Shortening of clotting time of polyP ₇₀ -GNPs in human plasma when assayed for contact activation as a function of monoP and GNP concentration. (A) Reduction in clotting time of 10nm polyP ₇₀ -GNPs and 50nm polyP ₇₀ -GNPs compared to equivalent concentration of molecularly dissolved polyP ₇₀ and heterogeneous long-chain polyP ₈₀₀ . (B) Reduction of clotting time of 10nm polyP ₇₀ -GNPs compared to the equivalent concentration of 10nm bulk-GNPs and 10nm PEG-GNPs. (C) Shortening of clotting time of 50nm polyP ₇₀ -GNPs compared against the same concentration of 50nm bulk-GNPs and 50nm PEG-GNPs.	103
Figure 5-5. Control absorbance experiments: (A) Actual (not normalized) absorbance traces of 10nm and 50nm polyP ₇₀ -GNPs at 5 μ M monoP. (B) Absorbance traces (at 405nm) of 10nm and 50nm polyP ₇₀ -GNPs incubated at high concentration with plasma over time. (C) 50nm polyP ₇₀ -GNPs after one	

hour incubation in PNP (without CaCl_2). (D) 10nm polyP₇₀-GNPs after one hour incubation in PNP (without CaCl_2). (E) Linearity of 10nm-GNP concentration with A_{405} . (F) Linearity of 50nm-GNP concentration with A_{405} 107

Figure 5-6. Procoagulant activity of polyP₇₀-GNPs assayed by A_{405} turbidity in PNP. (A) Normalized absorbance traces of 10nm polyP₇₀-GNPs at 2.5 μM monoP (n=3, \pm S.E.) compared to PEGylated GNP and citrate GNP with the same GNP concentration, and molecularly dissolved polyP₇₀; (B) Normalized absorbance traces of 10nm and 50nm polyP₇₀-GNPs at 5 μM monoP (n=3, \pm S.E.) compared to molecularly dissolved polyP₇₀. (C) Differential clotting activation of colloiddally-anchored and solution-phase polyP₇₀. Colloidal clustering of polyP promotes rapid initiation of the contact pathway of clotting by serving as a surface for the assembly of the primary complex, whereas polyP₇₀ in solution is only marginally capable of FXII zymogen activation. 109

LIST OF ABBREVIATIONS

API	active pharmaceutical ingredient
AUC	area under the curve
CMC	critical micelle concentration
CNS	central nervous system
DI	deionized
DLS	dynamic light scattering
EDAC	(N-(3-Dimethylaminopropyl)- <i>N'</i> -ethylcarbodiimide hydrochloride)
ES	external standard
FDA	Food and Drug Administration
FNP	flash nanoprecipitation
FPaD	flash precipitation and drying
GC-MS	gas chromatography-mass spectrometry
GNP	gold nanoparticle
HPLC	high-performance liquid chromatography
IS	internal standard
LC-MS	liquid chromatography-mass spectrometry
MIVM	multi inlet vortex mixer
MPS	mononuclear phagocytic system
MW	molecular weight
NP	nanoparticle
PCL	poly(caprolatone)
PEG	poly(ethylene glycol)
PEG- <i>b</i> -PCL	poly(ethylene glycol)-block- poly(caprolatone)
PEG- <i>b</i> -PLA	poly(ethylene glycol)-block-poly(lactic acid)
PEG- <i>b</i> -PLGA	poly(ethylene glycol)-block-poly(lactic-co-glycolic acid)
PGMA	poly(glycidyl methacrylate)

PGMA- <i>g</i> -PEG/PLA	poly(glycidyl methacrylate)-graft-poly(ethylene glycol)/poly(lactic acid)
PGMA- <i>r</i> -(PPEGMA)	poly(glycidyl methacrylate)-repeat-(poly(ethylene glycol)methacrylate)
PLA	poly(lactic acid)
PLGA	poly(lactic-co-glycolic acid)
PNP	pooled normal plasma
polyP	polyphosphate
Re	Reynolds number
R _g	radius of gyration
RESS	rapid expansion of supercritical solution
SANS	small-angle neutron scattering
SAS	small-angle scattering
SAXS	small-angle x-ray scattering
SLD	scattering length density
TEM	transmission electron microscopy
THF	tetrahydrofuran
wt%	weight percent
vol%	volume percent

SUMMARY

Recent developments in the field of nanotechnology have shown nanoparticles' attractive potential for enhanced drug bioavailability and functionality. Although the research of developing and producing nanoparticle-based medicines has undergone rapid expansion, numerous challenges lie ahead in terms of long-term stability, reproducibility, and scalability, being major limiting factors for their direct clinical translation. We have developed an integrated process of flash nanoprecipitation (FNP) in a custom-made multi inlet vortex mixer (MIVM) and freeze/spray drying (process referred to as Flash Precipitation and Drying - FPaD) in order to achieve high drug loading and long-term stability of polymeric nanoparticles encapsulating hydrophobic compounds. The process was first developed for a model hydrophobic compound – curcumin, and later applied and optimized for a variety of other hydrophobic compounds – both small-molecule drugs and macromolecule peptides. The effects of the physical parameters such as polymer to drug ratio and the nanoparticle to excipient ratio were investigated in order to achieve optimized formulations. The viability of the nanoformulations was verified in mice and bioavailability of curcumin and its major metabolite in plasma and central nervous system (CNS) of mice after oral delivery of nano-curcumin (curcumin encapsulated in PLGA nanoparticles) was precisely measured. A 20-fold reduction of dose requirement was observed when compared with the unformulated drug to achieve similar plasma and CNS tissue concentrations. The structures of a wide variety of polymeric micelles composed of simple linear diblock copolymers and novel brush amphiphilics as potential drug carriers were characterized by using small-angle x-ray scattering (SAXS). This method offers more benefits of polymeric nanoparticle characterization over conventional techniques such as dynamic light scattering (DLS) or transmission electron microscopy (TEM), providing *in situ* detailed internal features of the

nanoparticles (i.e. core radius, shell thickness, and aggregation number). Furthermore, surface modification of nanoparticles for enhanced functionality and targeted drug delivery was demonstrated by a facile conjugation of a therapeutic procoagulant hydrophilic polymer, polyphosphate (polyP), on the surface of gold nanoparticles (GNPs). The polyP-GNPs were found to be markedly superior contact-pathway activators compared to molecularly dissolved, platelet-sized polyP (of equivalent polymer chain length).

1 INTRODUCTION

1.1 Nanoparticles as Drug Delivery Carriers

In recent years, we have observed the unprecedented growth and development of research in the area of nanotechnology for biomedical applications and more specifically drug delivery. The submicron-size objects, due to their unique properties and large surface to volume ratio, have become an important class of materials capable of improving pharmacologic activities of conventional therapeutics.¹⁻³ Only careful and thoughtful design of these nanoparticles could lead to development of smart drug delivery vehicles, capable of increasing the stability and bioavailability of the drug as well as providing controlled release at the desired site and time of action.

Nanoparticles as drug delivery carriers could be classified into a variety of different groups. The most general way of classification is based on the nature of the material – organic vs. inorganic, as well as specific placement of the drug molecule within the nanoparticles. Organic nanoparticles differ significantly from inorganic nanoparticles mainly due to the principles of their fabrication and their intermolecular interactions.⁴ While most of the organic nanoparticles (e.g. liposomes, surfactant and polymeric micelles, polymersomes) are formed from at least several molecules through a self-assembly driven mechanism,⁵⁻⁷ inorganic nanoparticles (e.g., gold and iron oxide nanoparticles, quantum dots) are synthesized through the inorganic salt precipitation resulting in a formation of three dimensional structures of linked atoms. The much stronger interatomic interaction of the inorganic nanoparticles contrasts with a more dynamic-like structure of the organic nanoparticles. Furthermore, a drug or a medicinal compound of interest could be dissolved in certain region, entrapped/encapsulated in the core, or attached on the surface of nanoparticles. Organic nanoparticles such as the polymeric/surfactant

micelles or liposomes have the ability of the drug encapsulation inside the core of the structures with the surface being functionalized with targeting molecules. The inorganic nanoparticles usually display interesting optical,^{8,9} magnetic¹⁰⁻¹² or fluorescent^{13,14} properties within the solid structure that make them attractive as imaging or diagnostic particles, and the active and/or targeting compounds are functionalized on their surfaces.

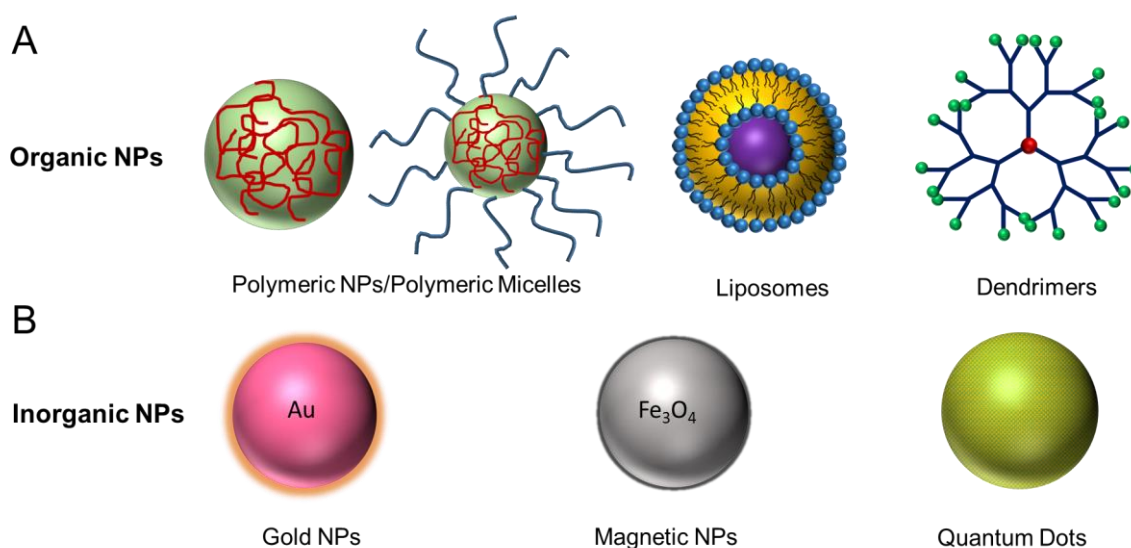


Figure 1-1. The examples of leading (A) organic and (B) inorganic nanocarrier platforms.

The majority of this thesis focuses on the development and characterization of organic polymeric nanoparticles for encapsulation of hydrophobic drugs in order to increase drug solubility and oral bioavailability. The surface modification of inorganic nanoparticles with therapeutic polymers is also discussed as an important implementation of improved drug functionality and targeted drug delivery.

1.1.1 Encapsulation of Hydrophobic Molecules into Polymeric Nanoparticles to Increase Drug Solubility and Bioavailability

The delivery of hydrophobic drug molecules has been considered a tremendous challenge due to their limited aqueous solubility and therefore bioavailability. The poor bioavailability depends on the dissolution kinetics where the dissolution rate is directly proportional to the surface area of the drug mass.¹⁵ Unformulated hydrophobic compounds in aqueous environments quickly form micron-sized or larger precipitates that would result in minimal drug absorption. Nanoparticles have been studied and considered as an effective way of enhancing the solubility of the hydrophobic compounds. Among them polymeric nanoparticles are particularly important due to their ability to provide higher drug loading capacity and greater stability upon dilution in biological fluids when compared with other drug delivery carriers such as surfactant micelles, liposomes, and dendrimers (**Figure 1-1**).

1.1.1.1 Current Production Methods of Polymeric Nanoparticles Encapsulating Hydrophobic Compounds and Our Process

Various methods of producing polymeric nanoparticles have been proposed and developed to date such as supercritical-fluid process, emulsification-based technologies, and nanoprecipitation. However, low drug loading, lack of control over the nanoparticle physicochemical properties, and problems associated with process reproducibility and scalability have still been considered as major hurdles in clinical translation of the polymeric nanoparticle-based medicines.

(1) Supercritical-fluid technology

Supercritical-fluid technology, which involves the use of solvents at temperatures and pressures above their critical point, has been considered as one of the important ways to produce

nanoparticles. The attractiveness of the process comes from utilizing environment-safe solvents that minimize the contamination of the final product. Two major super critical fluid technologies, rapid expansion of supercritical solution (RESS) and supercritical anti-solvent (SAS) process, have been commonly studied and used.¹⁶

(a) RESS

In the RESS process, the compounds of interest can be dissolved in a supercritical fluid followed by the expansion of the solution through a nozzle. The most commonly used supercritical solvents are water and carbon dioxide.¹⁶ The major disadvantage of this method is the limited solubility of the high-molecular weight polymers in those solvents that makes it a rather impractical method.

(b) SAS

The SAS method on the other hand, solves the problem of the limited compound solubility in a supercritical solvent by dissolving the polymer and drug compounds in an organic solvent. The supercritical solvent serves as an anti-solvent to precipitate them. After precipitation, the anti-solvent flows through a vessel removing the residual solvent. The vessel is depressurized and the solid product is collected.^{17, 18} Although this method is a continuous process, which is desired for large-scale production, it has a drawback of limited control over the nanoparticle size and surface properties.¹⁹

(2) Emulsification-based technology

The emulsification-based technology is another important nanoparticle formulation technology. Depending on the polymer properties and the miscibility of the organic phase with the aqueous phase, three major emulsification methods have been identified.

(a) Emulsification-solvent evaporation

This technique was first proposed by Gurny et al. in 1981.²⁰ The polymer and the compound of interest are first dissolved in water immiscible solvents such as chloroform, methyl chloride or ethyl acetate, and the solution is further emulsified through high-speed homogenization or sonication into the aqueous phase (i.e. water) to form an oil-in-water emulsion. The formation of nanoparticles starts during solvent evaporation that is achieved under reduced pressure or constant stirring.

(b) Emulsification-solvent diffusion

The emulsification-solvent diffusion technique (first described by Leroux et al.)²¹ is a modified method of the aforementioned production process. It utilizes the partially-water miscible solvent or the mixture of a water-immiscible organic solvent and a water-miscible organic solvent that is slowly added into the aqueous phase under constant stirring. Fast diffusion of the water-miscible solvent results in the formation of smaller emulsion droplets and thus smaller nanoparticles. The remaining solvent is then evaporated.²²

(c) Salting-out

The third emulsification-based method is called salting-out. In this method, more environment-friendly water-miscible solvents such as acetone or ethanol are used. The direct mixing of the organic phase and the aqueous phase is prevented by saturating the aqueous phase with salts (e.g. ammonium acetate, calcium chloride, magnesium acetate, etc.) that results in phase separation and emulsification. Subsequent dilution of the emulsion results in faster diffusion of the organic solvent. The organic solvents and the salts are then removed by cross-flow filtration.^{23, 24}

Although, the problem of using toxic chlorinated solvents in emulsification technology can be solved through the use of the modified salting-out method, the scale-up of the

emulsification-based methods that demand high-energy homogenization/sonication is rather challenging. Furthermore, the limited drug loading (<20%) and large polydispersity of nanoparticles are other drawbacks of this technology.

(3) Nanoprecipitation/Solvent displacement

Nanoprecipitation, first proposed by Fessi et al.,²⁵ has been considered one of the easiest and most economic ways of synthesizing polymeric nanoparticles. The method, also known as the solvent displacement technique, utilizes water-miscible organic solvents (e.g., dimethyl sulfoxide, acetonitrile, acetone, tetrahydrofuran, etc.) to dissolve polymer and hydrophobic drugs, and usually water as an anti-solvent for subsequent precipitation. Both the drug and the polymer are first dissolved in an organic solvent and then added drop-wise to a large amount of a water solution, followed by the organic solvent removal. Alternatively, the organic solution containing both the polymer and the drug compound can be dialyzed against large amount of water until complete removal of the organic solvent is achieved. Although the nanoparticle properties can be controlled by manipulating process parameters such as drug to polymer ratios or species' starting concentrations, the slow mixing of the process results in the limited drug entrapment efficiency as well as relatively large polydispersity in nanoparticle size.

(4) Flash Nanoprecipitation

Flash Nanoprecipitation (FNP) is a process that was first proposed by Prud'homme and coworkers²⁶ to reproducibly generate polymeric nanoparticles encapsulating hydrophobic drugs with high drug loading, controllable size, and surface properties. This process manipulates non-equilibrium structures of nanoparticles via kinetic control of sophisticated and fast mixing. Therefore, high drug loading could be achieved. The fast mixing results in uniform solvent displacement and nanoparticle properties depend on the competitive kinetics of the polymer

micellization and the hydrophobic compound nucleation and growth. A confined impinging jet mixer (CIJ) was first developed for the process.²⁶ However, the mixer necessitates equal momentum of two rapid jet streams that can indeed lead to a relatively fast nanoparticle growth. This geometry limitation has been further resolved by Liu et al.²⁷ who developed a multi-inlet vortex mixer (MIVM), which gave the flexibility of using multiple compounds of distinct solvent solubilities and manipulating solvent to anti-solvent ratios to achieve various supersaturation rates.

In this thesis we have developed and investigated the integrated process of FNP in the MIVM with freeze/spray-drying (process referred to as Flash Precipitation and Drying - FPd), which in addition to providing high drug loading can lead to long-term stabilization of the nanoparticles. Producing dry powders prevents further growth of nanoparticles, which can be later conveniently resuspended in aqueous buffers at desired concentrations for both *in vitro* and *in vivo* studies (**Figure 1-2**).

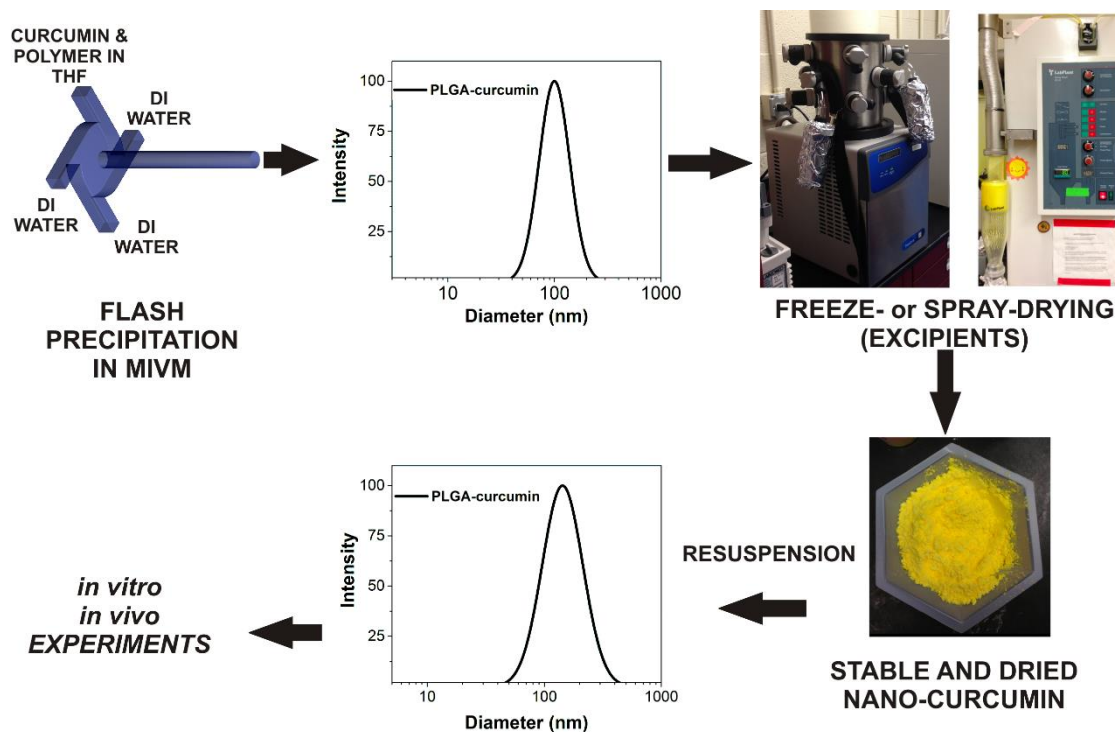


Figure 1-2. The general FPaD process of producing polymeric nanoparticles encapsulating hydrophobic compounds for *in vivo* and *in vitro* studies. Nanosuspensions are generated via flash nanoprecipitation in the multi inlet vortex mixer (MIVM). The nanoparticles are further freeze- or spray-dried together with excipients to obtain stable and dried product that can be conveniently resuspended at desired time and concentration for *in vitro* or *in vivo* animal studies.

1.1.2 Surface Modification of Nanoparticles for Enhanced Drug Functionality and Targeted Drug Delivery

Surface modification of nanoparticles plays a significant role in tailoring their therapeutic actions and dictating particle *in vivo* behavior as the biological systems respond strongly to the surface components of the nanoparticles. A wide variety of both natural and synthetic ligands (such as proteins, nucleic acids, and polymers) have been attached to the surface of

nanoparticles.²⁸⁻³⁰ The major goals of surface modification of the nanoparticles are increasing drug circulation time, enhancing drug bioavailability and functionality, and most importantly providing targeted drug delivery.

1.1.2.1 Prolonging Drug Circulation Time

Nanoparticles without proper surface functionalization may be recognized as foreign entities inside the body, quickly taken up by the mononuclear phagocytic system (MPS) and further excreted from the body.³¹ The surface modification of nanoparticles with hydrophilic polymers can lead to their longer circulation time inside the body as the stealth effect results in limited protein adsorption and inhibition of the uptake through the macrophages. One of the most commonly used polymers is poly(ethylene glycol) (PEG). It has been previously reported that surface density and length of PEG directly impact the extent of nanoparticle opsonization.³¹ For polymeric micelles composed of amphiphilic polymers, PEGylation is an instantaneous process that occurs during nanoparticle formation. The other types of nanoparticles, especially inorganic nanoparticles, rely on a two-step method the majority of time, where the nanoparticles are formed first and PEG is subsequently conjugated to their surface. Numerous approaches have been undertaken to introduce PEG with a functional group that can be covalently reacted with the complementary moiety on the nanoparticle surface. The PEGylation reaction with magnetic iron oxide nanoparticles has been previously demonstrated by the use of commercially available PEG-silane.³² The functional silane group of the polymer reacted with the hydroxyl groups on the nanoparticle surface resulting in PEGylated magnetic nanoparticles that exhibited reduced nanoparticle uptake by the macrophages.³² The surface modification of the gold nanoparticles with PEG was achieved by the conjugation of thiolated PEG on their surface.³³ The PEG-silica

nanoparticles have been previously prepared by reacting alkyl-hydroxyl groups on the surface of silica nanoparticles with carboxyl-modified PEG.³⁴

1.1.2.2 Enhancing Drug Bioavailability and Functionality

For many nanoparticles and more specifically inorganic solid-core nanoparticles, the outer nanoparticle surface serves as a drug conjugation and entrapment platform. Various covalent and non-covalent approaches have been studied and discussed to attach small molecular drugs as well as larger biomolecules such as proteins, peptides, or nucleic acids to the surfaces of nanoparticles.^{35, 36} The idea behind this surface decoration with therapeutic compounds is to increase drug functionality and bioavailability. Attachment of drugs to nanomaterials can maximize the drug exposure by prolonging drug persistence in blood circulation. Many *in vitro* and *in vivo* studies have indicated that drug efficacy was significantly enhanced when the drug was confined on nanoparticle surface. Tethering a small anti-cancer drug – doxorubicin on the surface of both gold nanoparticles as well as iron oxide nanoparticles resulted in much greater inhibition of the growth of multi-drug-resistant cancer cells when compared with the free form of the drug, owing to the higher cellular-uptake efficiency of nanoparticles, and subsequent acid-mediated drug release.^{37, 38} Other examples of enhanced drug functionality and bioavailability have been reported in literature.^{39, 40}

1.1.2.3 Providing Targeted Drug Delivery

Targeted drug delivery is essential to enhance the drug therapeutic effect at specific sites and minimize the undesired toxicity in the other tissues inside the body. This can be achieved by linking cell-specific ligands such as monoclonal antibodies and aptamers on the surface of nanoparticles. Introducing targeting ligands on the surface of nanoparticles can be achieved by

utilizing adsorption or covalent binding.⁴¹ A very common approach is to use hydrophilic block of the polymer (i.e. PEG) that is first functionalized with different reactive groups such as hydroxyl, amino, and carboxyl. Upon nanoparticle formation, the PEG with its functional group is exposed on the nanoparticle surface and available for other surface chemistry. As an example, this method was successfully applied to introduce A10 RNA aptamers on the surface of PLGA nanoparticles. This aptamer binds the prostate specific membrane antigen (PSMA). The carboxylated PEG-PLGA nanoparticles were formed first via nanoprecipitation and the amine – terminated aptamers were subsequently attached to the carboxyl groups on PEG via EDAC (N-(3-Dimethylaminopropyl)-*N'*-ethylcarbodiimide hydrochloride)-catalyzed reaction. It has been observed that the delivery of these aptamer-functionalized nanoparticles was significantly enhanced to the tumor sites when compared with the nanoparticles without any surface modification.⁴²

In this thesis, we presented a facile phosphoramidate conjugation chemistry to immobilize a hydrophilic polymer – polyphosphate on the surface of gold nanoparticles (GNPs). Polyphosphate has been known for its versatile procoagulant effects. The nanoparticle's hemostatic ability to initiate the contact pathway of blood coagulation was investigated and compared with the molecularly-dissolved polyphosphate of the same length. (**Figure 1-3**).

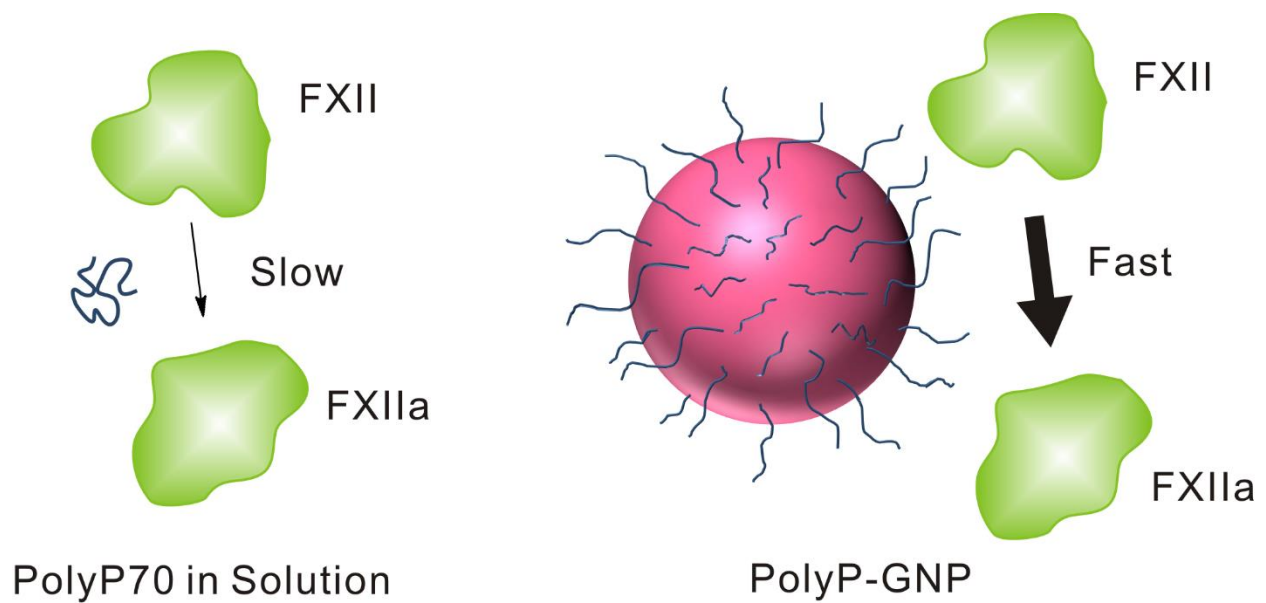


Figure 1-3. Surface modification of gold nanoparticles with polyphosphate (polyP) for enhanced drug functionality and targeted drug delivery.

1.1.3 Characterization Methods of Nanoparticles

Precise characterization of nanoparticle physicochemical properties is essential for design, development and optimization of nanoparticles for drug delivery applications. It is necessary to precisely determine the size and morphology of nanostructures at their native states, as these are also considered key factors affecting their *in vivo* behavior. Many conventional methods of nanoparticle characterization such as dynamic light scattering (DLS) or transmission electron microscopy (TEM) have been commonly used to determine the size and structural information of the nanoparticles. In recent years, small-angle scattering techniques such as small-angle x-ray scattering (SAXS) and small-angle neutron scattering (SANS) have become very fundamental techniques to reveal detailed internal features of nanostructures.

1.1.3.1 Dynamic Light Scattering (DLS)

Dynamic light scattering is a well-established technique that looks at the size distribution of nanoparticles in their native aqueous environment.^{43, 44} The Brownian motion of the nanoparticles results in the laser light to be scattered at various intensities that autocorrelate. The autocorrelation function $C(t)$ is,

$$C(t) = Ae^{-2\Gamma t} + B$$

where t is the delay time and A is an optical constant that is determined based on the instrument design. By increasing the delay time, the correlation function approaches constant background B .

Γ is related to the relaxation of the intensity fluctuations according to the following formula,

$$\Gamma = Dq^2$$

where D is the translational diffusion coefficient and q is the value obtained from the wavelength of the laser (λ_0), the scattering angle (θ) and the refraction index (n) of the liquid by the following equation,

$$q = \frac{2\pi n}{\lambda_0} 2 \sin\left(\frac{\theta}{2}\right)$$

By assuming spherical morphology, the particle diameter (d) is related to D according to the Stokes-Einstein relation:

$$D = \frac{k_B T}{3\pi\eta d}$$

where k_B is the Boltzmann's constant, T is the measurement temperature, and η is the viscosity of the medium in which the particles are suspended.

The size of the particles is outputted as the hydrodynamic diameter. This hydrodynamic diameter is defined as the diameter of an equivalent hard sphere that diffuses at the same rate as the structure being investigated. In case of polymeric micelles, the unique core-shell morphology

cannot be distinguished as the technique provides an overall micellar size (i.e. diameter of the core together with the thickness of the shell).

1.1.3.2 Transmission Electron Microscopy (TEM)

Transmission electron microscopy (TEM) is another well-established technique to look at the size and morphological features of nanoparticles.⁴⁵⁻⁴⁷ For conventional TEM, the beam of electron is passed through a thin grid that contains dried nanoparticles. The interaction of the electrons transmitted through the nanostructures results in the formation of an image that is focused onto an imaging or detecting device (e.g. fluorescent screen, photographic film, or CCD camera). The sample preparation for TEM can be a relatively complex procedure that is also very sample specific. The use of high atomic number staining has been commonly applied in this technique to enhance the imaging contrast. However, it should be noted that the process of drying of nanostructures on the grid and/or non-specific particle-substrate interaction often causes altering of their native structures and shapes. Cryo-TEM has also been extensively used in exploring nanostructures of soft-matter materials and biological samples.^{48, 49} However, “freezing” of the samples by liquid helium or nitrogen does not always guarantee the preservation of their native structures. Moreover, in both conventional TEM and Cryo-TEM the nanoparticles are prone to the electron beam damage. A novel approach of TEM measurement and analysis has been recently proposed and developed where a biological or nanoparticle sample can be encapsulated between two layers of monolayer-graphene sheets and captured within a liquid cell.⁵⁰ This newly developed liquid-cell TEM not only provides a more robust way of nanoparticle characterization in their solvent environment but also has an advantage of reducing the effects of the electron beam damage through use of graphene sheets. However,

sample preparation for liquid-cell TEM is difficult and requires special techniques and delicate setups.

1.1.3.3 Small-angle X-ray and Neutron Scattering (SAXS and SANS)

Small-angle scattering (SAS) techniques such as small angle x-ray scattering (SAXS) or small-angle-neutron scattering (SANS) have become essential characterization methods to provide insights into the morphological features of the nanoparticles with core-shell structures in their native states (i.e. aqueous suspensions).⁵¹ The difference of the electron densities or neutron scattering length densities between the micelles and their surrounding medium as well as the difference between the core material and the shell material can give sufficient contrast to obtain unique internal structural information of the micelles.

Small-angle scattering patterns are typically represented by the scattered intensity that is a function of the magnitude of the scattering vector q :

$$q = \frac{4\pi \sin \theta}{\lambda}$$

where 2θ is the scattering angle between the incident x-ray or neutron beam and the detector and λ is the wavelength. The most general equation describing the scattered intensity is as follows,

$$I(q) = nV^2\Delta\rho^2P(q)S(q)$$

where n is the number density of particles, V is the volume of the particles, $\Delta\rho$ is the scattering length density contrast, $P(q)$ is the particle form/shape factor, and $S(q)$ is the interparticle structure factor. For a sufficiently dilute system, the interparticle interaction is negligible and $S(q)$ is equal to 1. The $P(q)$ function has been previously derived for a wide variety of particle morphologies including simple shapes and more complex multilayer structures such as core-shell assemblies.

Radius of gyration (R_g) is the characteristic size determined by SAXS. For a given dilute system of the particles in the low q regime, the scattering intensity can be estimated based on the Guinier approximation according to,⁵²

$$I(q) = I(0)\exp\left(-\frac{1}{3}q^2R_g^2\right)$$

where $I(0)$ is the intensity extrapolated to $q=0$ and R_g is the radius of gyration. This expression is true only when the multiplication of q_{\max} and R_g is less than or equal to 1.3

Both techniques of SAXS and SANS have their advantages and disadvantages and often are used as complementary methods. SANS is a sample non-destructive technique that is sensitive to light elements and can use a contrast variation by selective deuteration to reveal the unique features of nanoparticles. SANS can also reveal the polymer chain exchange under equilibrium condition.⁵³ Although, this characterization method has its advantages as listed above, it is only available at large neutron facilities. Moreover, it requires a relatively large amount of sample volume and the effects of the sample deuteration may have some variable effects on its native structure. Furthermore, temporal resolution of time resolved-SANS (TR-SANS) is low (more than 100 milliseconds) compared to TR-SAXS.^{53, 54} On the other hand, SAXS can be used both in a laboratory and at synchrotron. Some of the main advantages of the method include shorter measurement time and little sample volume requirement. The limitations can come from the possibility of radiation damage and limited electron density contrast between certain components of more complex multi-layer structures.

In this thesis, we performed characterization of a variety of polymeric micelles as potential drug delivery carriers by using SAXS to reveal their internal features (**Figure 1-4**). The study looked for the first time at the structural information of polymeric micelles formed from

novel brush amphiphiles. DLS and TEM were used as complementary characterization techniques.

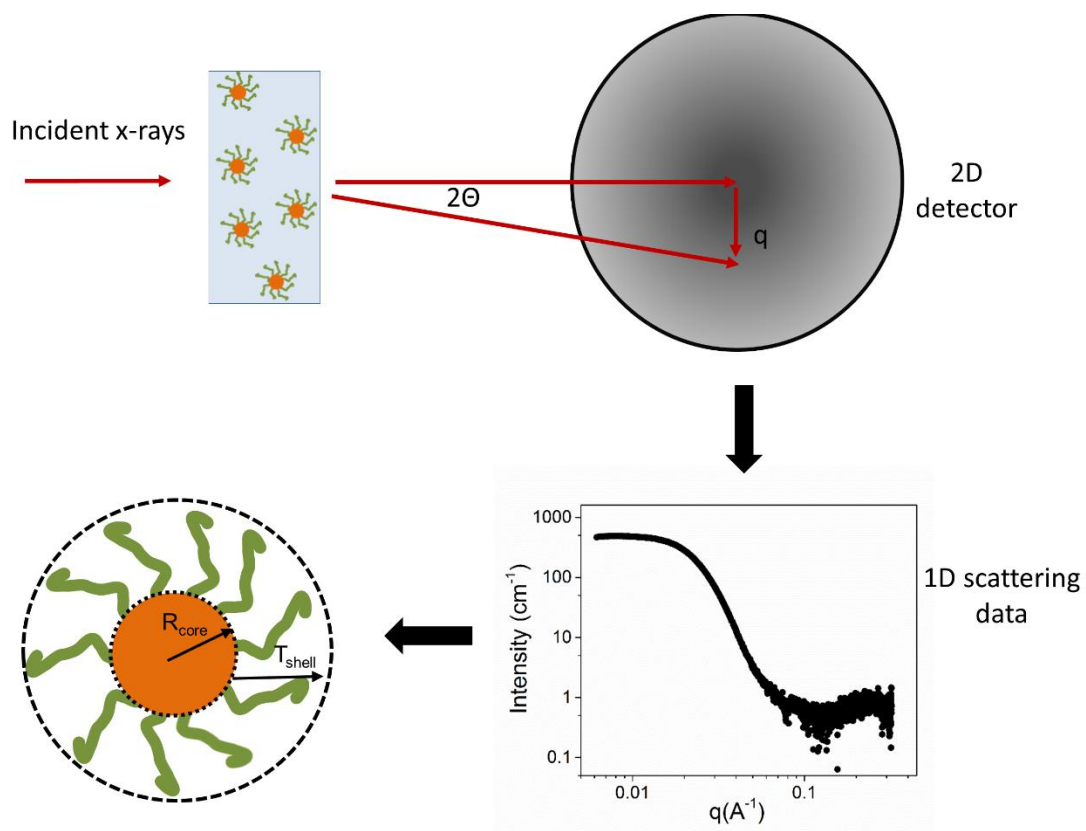


Figure 1-4. General schematic of small-angle x-ray (SAXS) technique.

2 FORMATION OF STABLE POLYMERIC NANOPARTICLES ENCAPSULATING HYDROPHOBIC COMPOUNDS BY FLASH PRECIPITATION AND DRYING (FPAD) PROCESSES

2.1 Introduction

It has been estimated that nearly 40% of currently marketed drugs and the vast majority of the drug compounds that are newly discovered and in development are hydrophobic.^{55, 56, 57} Delivery of these hydrophobic therapeutic compounds has been extremely challenging. Minimum solubility and thus bioavailability limit their clinical applications. In recent years, the vibrantly expanding field of nanotechnology has brought the possibility of overcoming these difficulties with the use of polymeric nanoparticles as drug carriers. These nanoparticles have the ability to increase the solubility of hydrophobic compounds, improve pharmacokinetics through sustained drug release, protect sensitive therapeutics from enzymatic or low pH environments, and provide targeted delivery of compounds of interest.^{58, 59}

Many methods have been established to produce polymeric nanoparticles encapsulating hydrophobic compounds. However, most of the conventional methods of nanoparticle preparation are limited by low drug loading (<20%) and broad particle size distribution. Furthermore, it is challenging to reproducibly generate stable nanoparticles with small size distribution and controllable surface properties, which are desired for translation into clinical applications. We have developed an integrated process, Flash Precipitation and Drying (FPaD) to successfully address these problems. The process manipulates the structures of nanoparticles via kinetic control of sophisticated and fast mixing in a multi-inlet vortex mixer (MIVM), resulting in high drug loading and small size distribution.⁶⁰ Further stabilization is achieved by freeze- or spray-drying of the nanosuspensions into powders to achieve long term stability of

nanoformulations. The process of drying the material is an important step that allows for subsequent preparation of drug formulations at desired concentrations for both *in vitro* and *in vivo* experiments.

The FPaD process was employed first to encapsulate a model compound - curcumin. Curcumin is a natural compound that can be extracted from Turmeric roots and has been recognized for a plethora of important biomedical functionalities, e.g. antioxidant, anti-inflammatory, antimicrobial, cancer preventive, and neuroprotective properties.⁶¹⁻⁶³ Recently, we have reported a novel functionality of curcumin to attenuate opioid tolerance and dependence.^{64, 65} Despite its great pharmacological activities, curcumin is highly hydrophobic which results in very low bioavailability. We have formulated this hydrophobic compound into stable polymeric nanoparticles by optimizing the process parameters of FPaD. The molecular structures of curcumin and investigated polymers are reported in **Figure 2-1**. A similar approach was also taken with a variety of other hydrophobic compounds, both small molecular weight drugs including several anti-viral candidate compounds (**Figure 2-2 A and B**) and larger molecular weight peptides such as anti-coagulant Myr-FEEERA and anti-tuberculosis ecumicin (**Figure 2-2 C and D**).

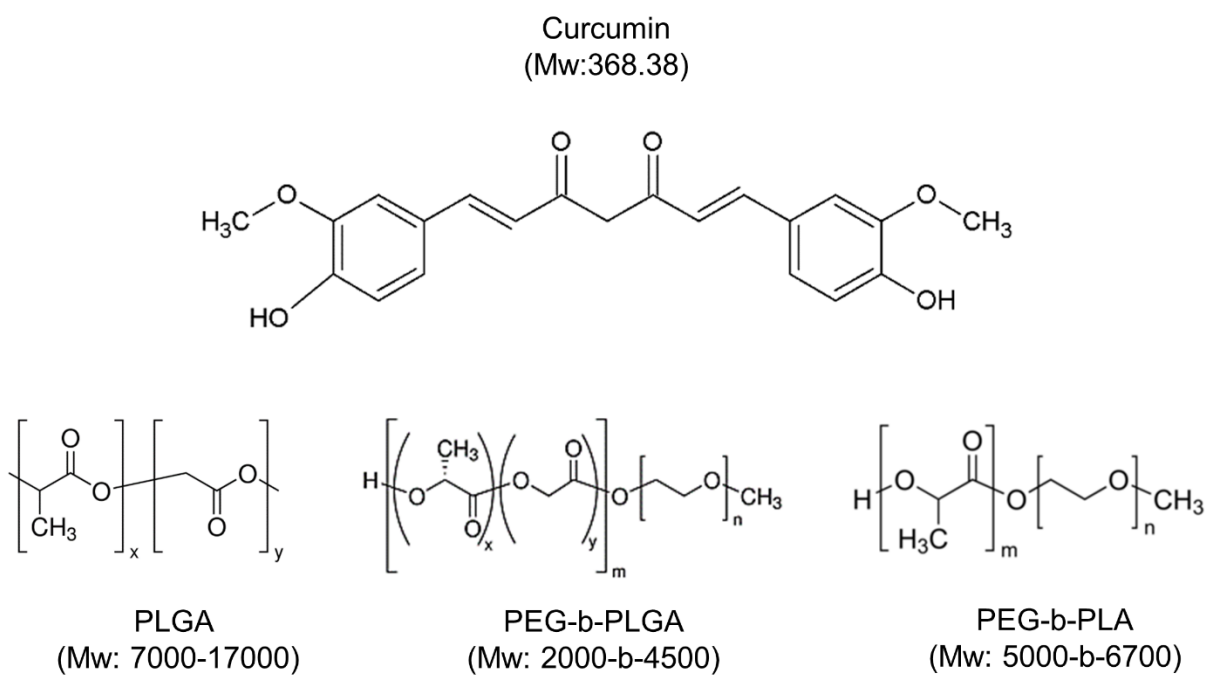


Figure 2-1. Molecular structures of the main model hydrophobic compound, curcumin, and the polymers investigated in the study.

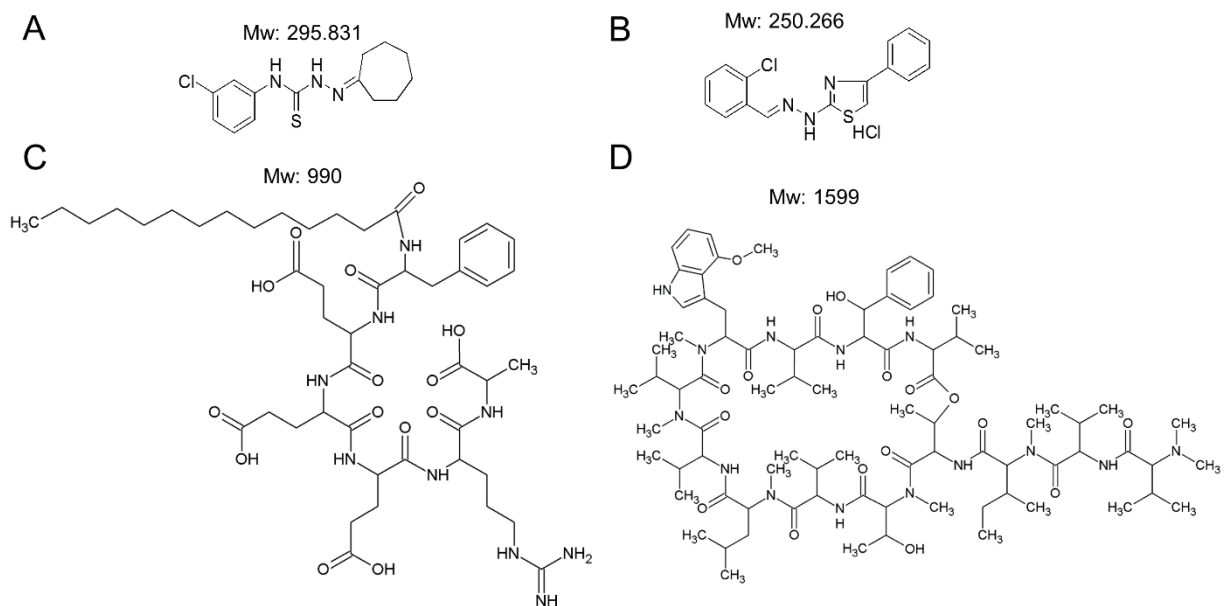


Figure 2-2. Molecular structures of the compounds used in this thesis study. (A) N1-(3-chlorophenyl)-2-cycloheptylidenhydrazine-1-carbothioamide (BTB05119). (B) 2-chlorobenzaldehyde 1-(4-phenyl-1,3-thiazol-2-yl)hydrazone hydrochloride (ML00176). (C) Myr-FEEERA. (D) Ecumicin.

2.2 Experimental Section

2.2.1 Materials and Methods

PLGA (acid terminated; PLA:PGA 50:50 w/w; Mw 7000-17000, Mw/Mn=1.8), PEG-*b*-PLGA (Mn 2000-*b*-4000), curcumin, tetrahydrofuran (THF), trehalose, leucine, ethanol, and methanol, were purchased from Sigma-Aldrich (St Louis, MO). PEG-*b*-PLA (Mn 5000-*b*-6700, Mw/Mn = 1.08) was purchased from Polymer Source (Dorval, Canada). Ecumicin (H14 peptide) was a kind gift of the Franzblau Lab (Institute for Tuberculosis Research, UIC). Myr-FEEERA peptide was a kind gift from the Du Lab (Department of Pharmacology, UIC). The anti-viral candidate compounds, N1-(3-chlorophenyl)-2-cycloheptylidenhydrazine-1-carbothioamide (BTB05119), 2-chlorobenzaldehyde 1-(4-phenyl-1,3-thiazol-2-yl)hydrazone hydrochloride (ML00176), 2-benzylidene-10,13,17-trimethyl perhydro cyclopenta[*a*]phenanthrene-3,17-diol (NRB03879), 4-benzhydryl-N-butyltetrahydro pyrazine-1(2H)-carboxamide (HTS00668) were kind gifts from the Rong Lab (Department of Microbiology and Immunology, UIC)

2.2.2 Nanoparticle Formation

Polymeric nanoparticles encapsulating hydrophobic curcumin were generated via flash nanoprecipitation in a MIVM (**Figure 2-3**). Information of the samples was summarized in **Table 2-1**.

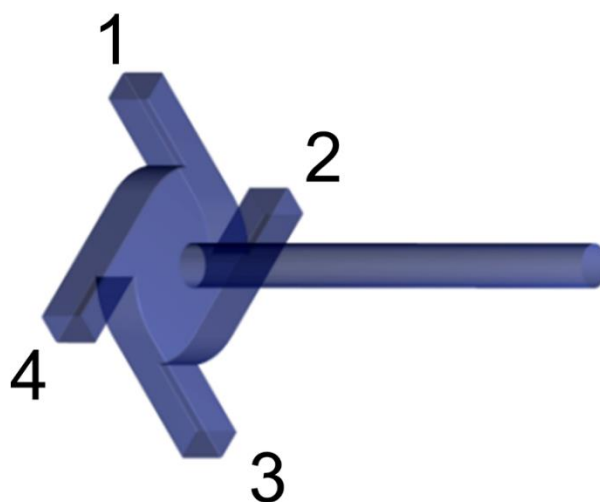


Figure 2-3. Schematic representation of a multi-inlet vortex mixer (MIVM).

Table 2-1. Conditions of polymeric curcumin nanoparticles.

Compound	Starting Drug Concentration	Polymer	Drug:Polymer Weight Ratio
curcumin	0.2wt%	PLGA	1:1
	0.2wt%	PEG- <i>b</i> -PLA	1:1
	0.2wt%	PEG- <i>b</i> -PLGA	1:1, 1:2, 1:5

During the process of flash precipitation, one of the four inlet streams consisted of the polymer and curcumin dissolved in THF. The other three inlet streams consisted of deionized water as an anti-solvent to precipitate both the drug compound and the polymer. The flow rate of stream 1 (organic stream) and 3 was set to be 6 ml/min and 54 ml/min for streams 2 and 4. The nanoparticles were collected into a beaker containing aqueous solutions with excipients under constant stirring. To freeze-dry the suspension, the collected nanoparticles were immediately

transferred into 20 ml glass scintillation vials (half-way filled) and flash-frozen in the ethanol-dry ice bath. To spray-dry the solutions the suspension after collection were directly pumped into the spray dryer.

2.2.3 Freeze-drying and Spray-drying

To maintain long-term stability of the nanoparticles and to conveniently generate suspensions at various nanoparticle concentrations, freeze drying and spray drying were applied and optimized. In order to prevent the nanoparticles from aggregation, various amounts of excipient molecules such as trehalose and/or leucine were added to the nanoparticle suspensions. These act as spacers and prevent the collision of neighboring nanoparticles. The details of the optimized amount of excipients used were reported in the **Results and Discussion** section (**Section 2.3**). The freeze-drying process lasted 3 days in a freeze dryer (Labconco, FreeZone 1 Liter Console Freeze Dry Systems, Kansas City, MO) at a vacuum pressure and -47 °C.

The spray-drying process was carried out by integrating the MIVM with a spray dryer (LABPlant, SD-05 Spray Dryer, North Yorkshire, UK) as previously described and reported.^{64, 66} Ethanol (60% (v/v)) was added to lower the inlet temperature of the spray dryer. Process conditions included air inlet temperature of 75 °C and a feed rate of 10 ml/min.

2.2.4 Resuspension of Nanoparticles

The dried nanoparticles were resuspended at low (<20 mg/ml) and high (600 mg/ml) construct concentrations. Two methods of nanoparticle redispersion, vortex mixing and bath sonication (Branson, CPX1800, Taiwan), were tested. Bath sonication was used for the resuspension of nanoparticles (NPs) at higher construct (including NPs and excipients) concentrations (600 mg/ml). The resuspension time was 10 minutes.

2.2.5 Nanoparticle Characterization by Dynamic Light Scattering (DLS)

Nanoparticle size and size distribution right after mixing and after resuspension of dried powder in deionized water were measured by dynamic light scattering (DLS) (Brookhaven, NanoDLS, Holtsville, NY). The size of the particles was reported as the intensity-weighted diameter. The values for viscosity and refractive index were set to be 0.890 cP and 1.331, respectively.

2.3 Results and Discussion

Polymer micellization is a spontaneous self-assembly process. Critical micelle concentration (CMC) of the polymers used for drug delivery is usually vanishingly small. Over the last decade, it is characterized that the polymer chain exchange is exceedingly slow and equilibrium may never be achieved on a global scale. Therefore the initial conditions and the solvent exchange conditions are critically important to decide the metastable structure of the polymeric nanoparticles which directly influence particle drug loading and long-term stability. Conventional methods of polymeric nanoparticle synthesis emphasizing on polymer chemistry and matching precipitation kinetics without considering flow field and mixing conditions have demonstrated clear limitations in drug loading capacity. FNP is a technique employing kinetic control of nanoparticle formation that utilizes high-speed velocity streams of a solvent and an anti-solvent to create the turbulent flow field necessary for homogenous mixing and rapid coprecipitation of both polymer and drug. Furthermore, the unique four-tangential stream geometry of the MIVM allows for the control of supersaturation rates and the final solvent quality after mixing, as well as enabling separation of various reactive agents if their solubility is limited in the same solvent.²⁷ The process parameters have been previously studied for a wide range of polymers and small molecules.^{60, 66} In this thesis study, we have optimized the operational

conditions and material initial concentrations for the interesting compounds of the study. For the mixing parameters, it has been previously reported that at $Re > 2000$, the nanoparticle size was independent of mixing velocity.^{27, 60} Furthermore, higher anti-solvent (water) to solvent (organic solvent) ratio resulted in smaller particle size due to higher supersaturation rates resulting in generation of more nucleation sites.⁶⁰

Although, high drug loading can be relatively easily achieved via FNP by careful selection of the materials and process parameters, and the initial unimodal particle size distribution could be recorded (**Figure 2-4A and B**), the nanoparticle stability over time in suspension generates another challenge. Highly loaded nanoparticles (with ~50% drug loading) can undergo rapid growth over short periods of time resulting in large aggregates (**Figure 2-4C**).

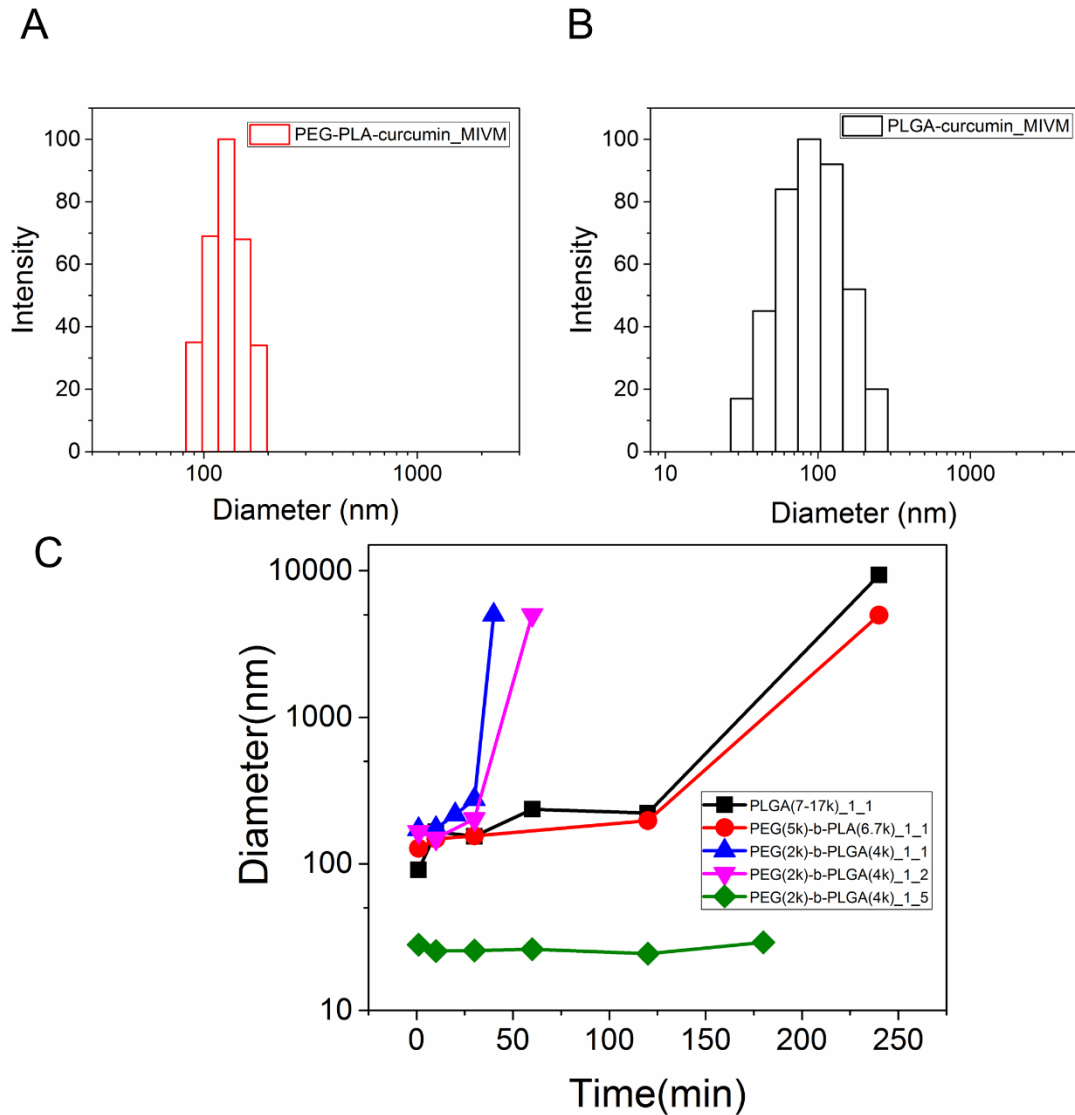


Figure 2-4. (A) Size distribution of PEG-*b*-PLA-curcumin nanoparticles immediately after mixing. (B) Size distribution of PLGA-curcumin nanoparticles immediately after mixing. (C) Growth kinetics of polymeric nanoparticles encapsulating curcumin.

Our results demonstrated that the nanoparticle growth is very evident for PEG-*b*-PLGA (Mw 2k-*b*-4k) nanoparticles encapsulating curcumin at 1:1 and 1:2 drug to polymer ratio. The possible reason is that the polymer with a short block length of each block may not be able to provide enough surface coverage for the nanoparticles, causing their rapid growth. The ratio was

then further increased to 1:5 and much better stability was achieved. On the other hand, PEG-*b*-PLA (Mw 5k-*b*-6.7k) and PLGA (Mw 7-17k) at 1:1 drug to polymer ratios resulted in more stable nanosuspensions up to 2 hrs. Nevertheless, the growth kinetics showed the necessity of further stabilization of the nanoformulations. The poor aqueous stability of the nanoparticles can be partially explained by the relatively small partition coefficient (logP) of curcumin (logP=3).⁶⁷,⁶⁸ It has been previously reported that the drug compounds with higher logP values (>6) (i.e. more hydrophobic/lipophilic nature) such as beta-carotene⁶⁹ or bifenthrin⁷⁰ exhibited superior aqueous stability after flash nanoprecipitation. The proposed mechanism for the limited suspension stability over time is based on the weaker hydrophobic interaction of curcumin and the hydrophobic part of the polymer causing it to slowly move to the surface of nanoparticles, leak, and recrystallize over time.⁶⁷

Freeze-drying was the primary drying technique applied and optimized in this study to prolong the lifetime of the nanoparticles. It consists of first freezing a sample below its freezing point and then lowering the surrounding pressure, so the frozen sample sublimates. Although the small amount of organic solvent is present after mixing (5 vol%), the sample can be still relatively easily freeze-dried. Previous studies reported that the non-aqueous co-solvent freeze-drying could have the benefits of faster sublimation rates with the right choice of the solvent.⁷¹ The stresses that are present during freezing and desiccation steps can cause irreversible aggregation of nanoparticles. The use of cryoprotectant and lyoprotective agents prevents undesired nanoparticle agglomeration.⁷² Generally, the higher concentration of the excipients and the quicker the freezing process is and the better the nanoparticle resuspension afterwards. Various excipients such as sucrose,^{73, 74} mannitol,⁷⁵ glucose,^{76, 77} and trehalose^{74, 78, 79} have been investigated for freeze-drying of nanoparticles. Among these, trehalose has been considered to

have more advantages due to lower chemical reactivity and higher glass transition temperature. Furthermore, the absence of the hydrogen bonding inside its structure allows for the flexible formation of the hydrogen bonds with the nanoparticles.^{80, 81}

The nanoparticle suspensions were quickly frozen in the ethanol-dry ice bath immediately following mixing to quench further nanoparticle growth. Various amounts of excipients were tested to see if the nanoparticles were able to be redispersed back to their original size. When tested at lower construct concentration (<20 mg/ml), the nanoparticles were able to be suspended homogenously when the trehalose to nanoparticle ratio was greater than 180. However, the resuspension at higher construct concentrations (600 mg/ml), which may be desired for achieving maximized dose for measuring animal pharmacokinetics, resulted in the presence of a few visible micron-sized particles when the trehalose to NP ratio was 180. A mixture of trehalose and leucine was found to help the redispersion at higher concentrations, reproducing almost the original size distribution of the nanoparticles. Leucine, in addition to increasing the viscosity of the suspension as in case of trehalose, has been previously reported to act as the surface stabilizing/coating agent preventing leakage of curcumin from nanoparticles.⁸²

Table 2-2. Resuspension of PLGA-curcumin (1:1) nanoparticles after being freeze-dried with different amounts of excipients. The size of the nanoparticles was determined after resuspending them at low (<20 mg/ml) or high (600 mg/ml) construct concentration. Average diameter of the nanoparticles immediately after formation before freeze-drying was 100.1 nm.

Excipient	Nanoparticle	Average diameter (nm)
Used	to Excipient	at low (<20 mg/ml) and high 600 mg/ml)
	Weight Ratio	

		construct concentration
trehalose	1:20	>1 μ m (low)
trehalose	1:50	>1 μ m (low)
trehalose	1:100	>1 μ m (low)
trehalose	1:180	180nm (low) & >1 μ m (high)
trehalose & leucine	1:200 & 1:3	141.2nm (high)
trehalose & leucine	1:300 & 1:5	121nm (high)

Another common technique used to produce nanoparticle powder and investigated here was spray drying. This method uses a spray nozzle to disperse a solution into small-size droplets (20 to 180 μ m) which are further heated with air or nitrogen to evaporate the solvent. Small size of the droplets allows for maximizing heat transfer and vaporization of the liquid. Several parameters, such as the temperature of the incoming hot stream and the amount of the excipients, need to be justified carefully to achieve stable powders. The conditions of the spray drying were previously optimized, indicating that large excipient amount was necessary to achieve good redispersion after drying.⁶⁶ The same conditions were applied for the preparation of the nanoparticles in this thesis study.

Two drying techniques discussed here have both advantages and disadvantages. Certain criteria (such as the amount of the final product needed, availability/accessibility and cost of the active pharmaceutical ingredients (API), and processing time) need to be taken into account in order to decide which would be more suitable to use. Although spray-drying could be integrated with the upstream processes (such as precipitation) to be continuous, scalable, and rapid, on a small laboratory scale it has a major drawback of limited yield (<50%) which is not desired when

the compound or polymer availability is limited. Furthermore, the high temperature of the drying stream can cause irreversible changes of the active compounds or the polymers and caution needs to be taken in order to prevent from losing their natural properties. On the other hand, freeze-drying is a less invasive technique that maintains and preserves the products due to low temperature operation. The yield of the process can reach nearly 100%. However, it is a more time- and energy-consuming, and thus more expensive.

The resuspension of the nanoparticles was tested via simple vortexing as well as bath sonication. Although, the samples at low NP concentrations were resuspended homogeneously via simple vortexing for 10 minutes, it was not sufficient for the higher concentration samples which resulted in heterogeneous resuspension with visible micron-sized particles (**Figure 2-5**). Bath sonication, providing uniform application of sound energy to agitate nanoparticles, was more appropriate to homogeneously resuspend nanoparticles at higher concentrations (close to the solubility limit of trehalose). The size distributions of the PLGA and PEG-*b*-PLA nanoparticles immediately after FNP and resuspended after freeze- or spray-drying were reported in **Figure 2-6**. The size slightly increased after the drying processes and subsequent resuspension. However, it was still in a suitable range that all of them should be able to go through sterile filtration.

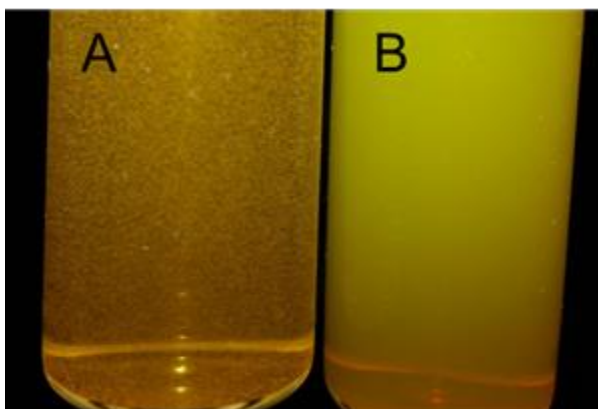


Figure 2-5. Resuspension of PLGA-curcumin NPs at high concentration via (A) vortexing for 10 minutes and (B) bath sonication for 10 minutes.

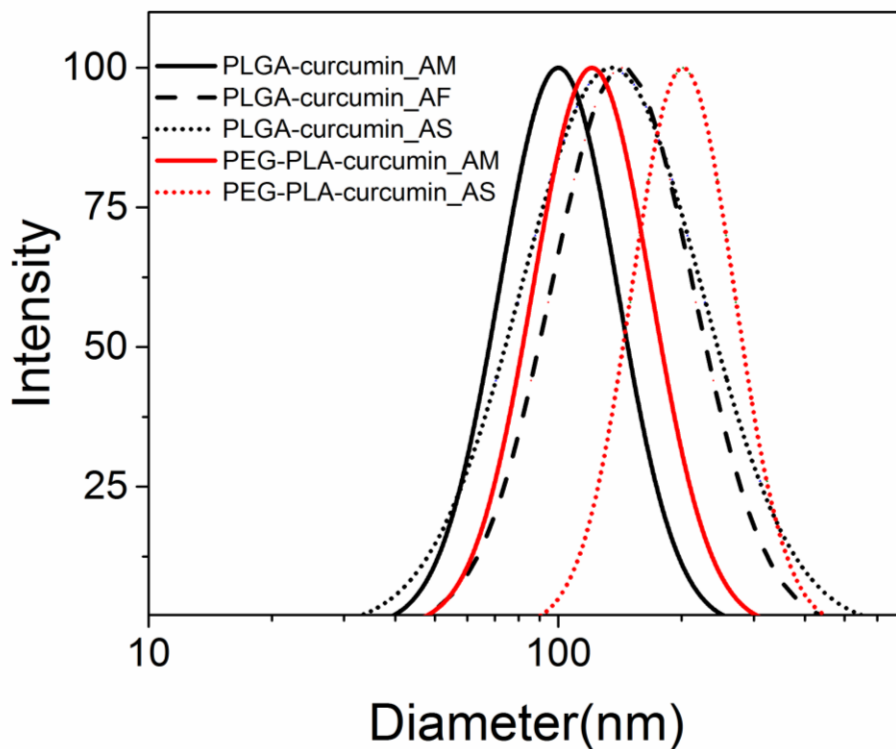


Figure 2-6. Lognormal size distribution of nanoparticles right after mixing in the MIVM (AM), and resuspended after freeze drying (AF) and spray drying (AS).

A similar approach of nanoparticle stabilization via the integrated process of FPaD was further taken for other types of hydrophobic compounds. Testing different small molecular drug candidates as well large molecular-weight peptides is essential to prove the feasibility of the FPaD process.

The mixing conditions in the MIVM were similar as for the formation of the curcumin nanoparticles. The drug compounds and the polymers were both dissolved in THF and rapidly

precipitated. The exception was given for the anticoagulant Myr-FEEERA peptide that could not be dissolved in THF. The unique four-stream design of the MIVM allowed for the separation of the drug and polymer streams. The flow streams were organized in the following way. Stream 1 was PLGA dissolved in THF, stream 3 was Myr-FEEERA dissolved in methanol, and streams 2 and 4 consisted of DI water. The same flow rates were chosen as before. Due to the limited availability of the drug compound, freeze-drying was applied as the post-mixing process to preserve the precious sample. The formation conditions and size characterizations for the nanoparticles were reported in **Table 2-3**. The nanoparticles were redispersed back to their original size with the proper amount of excipients. Moreover, it could be also observed that the nanoparticles formed at 1:1 polymer to drug ratio (indicating 50% drug loading) required higher amount of the excipients to retain their size after drying and resuspension, while for the PLGA-ecumicin nanoparticles at 6:1 polymer to drug ratio (corresponding to 14% drug loading), 50 times trehalose was sufficient to stabilize the nanoparticles when redispersed at high construct concentration (600mg/ml). The close proximity of the drug to the surface of the nanoparticles that are highly loaded could result in induced aggregation during resuspension at high construct concentrations.

Table 2-3. The FPaD process parameters and size distribution of nanoparticles encapsulating a variety of small and large MW hydrophobic compounds.

Compound	Starting Drug Concentration	Drug:PLGA Weight Ratio	Nanoparticle to Trehalose(T) or Leucine (L) Weight Ratio	Size after Mixing	Size After Resuspension
BTB05119	0.02 wt%	1:1	1:300 T, 1:5 L	236 nm	243.5 nm

ML00176	0.02 wt%	1:1	1:300 T, 1:5 L	-	208.8 nm
Myr-FEEERA	0.02 wt%	1:1	1:300 T, 1:5 L	197.4 nm	208.7 nm
Ecumicin	0.05 wt%	1:6	1:50 T	110.4 nm	116.2 nm

2.4 Conclusions

In this chapter, we have discussed the development of an integrated process, FPaD, for the production of stable nanoparticles encapsulating poorly water soluble medicinal compounds at high drug loading and for long-term storage. The study demonstrated that FPaD is a unique technique capable of producing nanoparticles encapsulating both small molecules and large peptides at high drug loading. Long-term stabilization was achieved by applying drying processes such as freeze-drying and spray-drying to the nanoparticle suspensions. The choice of the drying process depends on the API availability and cost, and the requirement of processing time. The use of excipients was essential to preserve the nanoparticle characteristic size during the drying processes. Although, the size was slightly increased after nanoparticles were resuspended in aqueous solutions, all the nanoparticles could still go through sterile filtration and be in the size range appreciated for applications of drug delivery. For the samples with lower polymer to drug ratio (i.e., higher drug loading), more drug could be exposed closer to the surface of the nanoparticles; therefore, the higher quantity of excipients was required to achieve better resuspension. Furthermore, the resuspension of the nanoparticles at high construct concentrations close to the solubility limit of the major excipient, trehalose, required the use of sonication rather just simple vortexing.

3 BIOAVAILABILITY AND BIOFUNCTIONALITY OF POLYMERIC NANOPARTICLES ENCAPSULATING CURCUMIN

Reprinted with permission from Magdalena Szymusiak, Xiaoyu Hu, Paola A. Leon Plata, Paulina Ciupinski, Zaijie Jim Wang, and Ying Liu, Bioavailability of Curcumin and Curcumin Glucuronide in the Central Nervous System of Mice after Oral Delivery of Nano-curcumin, *International Journal of Pharmaceutics*, 2016, doi:10.1016/j.ijpharm.2016.07.027

3.1 Introduction

Curcumin is a naturally occurring phenolic compound that can be isolated from Turmeric roots. In recent years, a plethora of interesting and very promising bioactivities has been identified or attributed to curcumin, notably antioxidant,^{83, 84} anti-inflammatory,⁶³ antimicrobial,^{62, 85} and neuroprotective⁸⁶ properties. Our previous studies also suggested that curcumin could attenuate or even reverse opioid antinociceptive tolerance and dependence in mice.^{64, 65} However, the hydrophobic nature of the drug limits its aqueous solubility and bioavailability, hindering curcumin's clinical translation into a useful therapeutic agent.

Several strategies have been employed to increase solubility and oral bioavailability of curcumin. Chemical conjugation of curcumin with phospholipids, proteins, or polysaccharides has been demonstrated as one way to enhance its solubility.^{87, 88} The use of adjuvant molecules such as piperine, quercetin, or silibinin and their concomitant administration with curcumin has been implemented and shown to improve the oral absorption of curcumin by inhibiting metabolic conjugation such as conjugation with glucuronic acid.^{89, 90} However, in most of these cases curcumin is not fully protected and could be rapidly degraded. Furthermore, the strategies discussed above do not provide the ability to target curcumin into specific sites of action. More recently, encapsulation of curcumin in polymeric nanoparticles and lipid carriers has been

extensively studied to develop formulations that could not only improve solubility of the drug, but also provide protection from enzymatic and pH degradation, prolong drug circulation inside the body after initial oral absorption, and with additional surface modification provide sustained drug release at the target tissue. The most common polymeric carriers for curcumin reported in literature include poly(lactic-co-glycolic acid) (PLGA), poly(ethylene glycol)-*b*-poly(lactic acid) (PEG-*b*-PLA), and poly(ethylene glycol)-*b*-poly(lactic-co-glycolic acid) (PEG-*b*-PLGA) polymeric particles.⁹¹⁻⁹⁴ Curcumin encapsulated in phospholipid vesicles composed of soybean lecithins (SLP-WHITE and SLP-PC70, 1,2-Dimyristoyl-*sn*-glycero-3-phosphocholine (DMPC), 1,2-Dimyristoyl-*sn*-glycero-3-phospho-*rac*-(1-glycerol) (DMPG) has also been investigated.⁹⁵⁻⁹⁷ However, the methods that were used for the production of the aforementioned formulations (such as emulsion-based encapsulation or co-solvent evaporation) suffered from low drug loading (<15%) and broad particle size distribution.

We employed the FPaD process to generate stable polymeric nanoparticles encapsulating curcumin as described in the previous section. The nanoparticles in dry-powder format could be stable more than 12 months. Rapid co-precipitation of hydrophobic compounds and block copolymers overcomes thermodynamic limit of drug loading, resulting in “kinetically frozen” nanostructures with high drug loading (~50%) and almost 100% encapsulation efficiency. Furthermore, our process is highly reproducible and scalable for the increased demand of curcumin nanoparticles.^{66, 98}

Using the nano-curcumin (curcumin encapsulated in poly(lactic-co-glycolic acid) (PLGA) nanoparticles) as the platform, we demonstrated the efficacy of nano-curcumin in both prevention and reversal of morphine tolerance and dependence in mice at a relatively low oral dose.^{64, 65} Furthermore, it was determined the observed behavioral effects in the rodent models

correlated with curcumin's inhibition of CaMKII α activity in the brain, suggesting an underlying mechanism involving the presence of curcumin in the central nervous system (CNS) to suppress the activity of CaMKII α that is critically important in the development and maintenance of opioid tolerance and dependence.^{65, 99, 100} A pharmacokinetic study was then carried out to quantify curcumin in the CNS and in blood plasma after its oral administration, so that nanoparticle format of curcumin could be further adopted as the platform to completely elucidate the underlying mechanism and to eventually become an essential part of a tool kit for severe pain management.

Although many studies reported the pharmacokinetics of curcumin in rodents or humans, a lot of them did not separately analyze curcumin and its metabolites, causing overestimation of curcumin availability in blood or tissues. It has been observed that these studies usually lacked analytical details such as high-performance liquid chromatography (HPLC)/ liquid chromatography-mass spectrometry (LC-MS) chromatogram data or blood/tissue collection and treatment protocols. Since curcumin can be quickly metabolized, the lack of specificity may mislead investigators when designing nanoparticle formulations and evaluating the therapeutic mechanisms and efficacy.

In this work, curcumin bioavailability in plasma, brain and for the first time spinal cord tissue after oral administration of nano-curcumin and curcumin was investigated by employing a highly sensitive LCMS/MS method. Furthermore, the examination of the main curcumin metabolite, curcumin glucuronide, upon oral administration, was conducted using a novel methodology of direct extraction and quantification without hydrolyzing the glucuronide moiety. The obtained results correlate well with our previous reports of nano-curcumin's efficacy of attenuating morphine tolerance and dependence based on behavioral studies in mice models.

3.2 Experimental Procedures

3.2.1 Materials and Reagents

PLGA (acid terminated; PLA:PGA 50:50 w/w; Mw 7000-17000, Mw/Mn=1.8), tetrahydrofuran (THF), dimethyl sulfoxide (DMSO), trehalose, leucine, methanol, acetonitrile, and ethyl acetate were purchased from Sigma-Aldrich (St Louis, MO). Curcumin (>98%) was purchased from ChromaDex (Irvine, CA). Curcumin glucuronide standard was purchased from TLC PHARMACHEM (Ontario, Canada).

3.2.2 Animals

Male ICR mice (20-25g, Harlan Laboratories, Indianapolis, IN) were maintained on a 14/10h light/dark cycle with access to food and water *ad libitum* prior to experimental procedures. All experiments were performed with an approval by the Animal Care and Use Committee of the University of Illinois at Chicago and in accordance with the policies and recommendations of the National Institutes of Health guidelines for the handling and use of laboratory animals.

3.2.3 Nanoparticle Preparation and Characterization

Nanoparticles of curcumin encapsulated in PLGA were generated by flash nanoprecipitation in the MIVM. One of the four inlet streams was 0.2 wt% PLGA together with 0.2wt% curcumin in THF. The other three inlet streams consisted of deionized water as the anti-solvent to precipitate both the drug compound and the polymer. The flow rate of stream 1 (organic stream) and 3 was set to be 6 ml/min and 54 ml/min for streams 2 and 4. Thus nanoparticles were prepared at Reynolds number of 8100 to ensure homogeneous micromixing and kinetically-controlled assembly of nano-curcumin.⁶⁴ Particles were collected into a beaker

containing sugar solutions under constant stirring and the samples were flash-frozen in an ethanol-dry ice bath and further freeze-dried to obtain dry powder.

To test drug loading and encapsulation efficiency of curcumin in nanoparticles, the nanoparticle suspension after mixing was first diluted with DI water, filtered with 0.45 μm filter, and freeze-dried as previously reported.¹⁰¹ Curcumin not encapsulated in the nanoparticles would form large drug aggregates that would be filtered-out. The dried powder was first redissolved in DMSO at the solid construct concentration of 10mg/ml and quantified by UV-Vis spectrophotometry at the absorbance wavelength of 420 nm. Drug loading (DL) and encapsulation efficiency (EE) were defined as follows,

$$DL (\%) = \frac{\text{Amount of curcumin encapsulated in nanoparticles}}{\text{Total weight of nanoparticles}} \times 100\% \quad \text{and}$$

$$EE (\%) = \frac{\text{Amount of curcumin encapsulated in nanoparticles}}{\text{Feeding amount of curcumin}} \times 100\% , \text{ respectively.}$$

Nanoparticle sizes and size distribution were measured by the DLS (Brookhaven, NanoDLS, Holtsville, NY). The size of the particles was reported as the intensity-weighted diameter. The values for viscosity and refractive index were set to be 0.890 cP and 1.331, respectively.

3.2.4 Freeze Drying of the Nanoparticle Suspensions and Resuspension of Powders

The purpose and main steps of the freeze-drying process were described in Chapter 2. It was found that the curcumin nanoparticles could be completely resuspended homogeneously when nanoparticle to trehalose and leucine weight ratio was greater than 1:200 and 1:3, respectively.

The freeze-drying process lasted 2-3 days in a freeze dryer (Labconco, FreeZone 1 Liter Console Freeze Dry Systems, Kansas City, MO) at a vacuum pressure and -47 °C to ensure that majority of the organic solvent was removed. The amount of organic residue was measured using a gas chromatography coupled with a mass spectrometry (GC-MS). The dried powders were resuspended at high construct concentration (420 mg/ml) by using a water bath sonicator for 5 minutes (Branson, CPX1800, Taiwan) and immediately orally dosed to mice through a gavage.

3.2.5 GC-MS Analysis for Residual THF Content in the Dried Powder to Comply with the FDA Regulations

Headspace analysis with GC-MS was carried out on a Joel (JCMS-GCmateII) GC-MS system (Peabody, MA) equipped with an Agilent HP-5MSUI column (Santa Clara, CA). THF standards (0.001vol% to 0.5vol%) were prepared in deionized water. Nanoparticles were resuspended in water at the same construct concentration (420 mg/ml) as for dosing animals. The standards and samples were first heated up at 85°C for 15min and 5 µl of each one was directly injected into the GC-MS instrument. MS was scanned from 10- to 850m/z. Identification and quantification of THF was achieved by using a suitable ion transition (72 →42).

3.2.6 Pharmacokinetic Study in Mice

3.2.6.1 Plasma and Tissue Collection

Separate groups of mice received nano-curcumin (PLGA nanoparticles encapsulating curcumin) by gastric gavage at a dose of 20 mg/kg or aqueous suspension of pure curcumin at a dose of 20 mg/kg and 400 mg/kg. At eight different time points (3min, 5min 7.5min, 15min, 30min, 1hr, 2hr, and 4hr), four mice per time point were sacrificed and the blood was withdrawn via cardiac puncture with a heparinized syringe. The collected blood samples were centrifuged at

3,000 rpm for 10 minutes to separate plasma. Immediately following blood collection, perfusion with normal saline was performed. Brain and spinal cord tissues were collected, rinsed with ice-cold saline and stored at -80°C until further analysis. At the day of analysis all tissues were homogenized with normal saline.

3.2.6.2 Extraction of Curcumin and Curcumin Glucuronide from Plasma and Tissues.

The extraction of curcumin from plasma, brain and spinal cord was performed by liquid-liquid extraction with ethyl acetate. Briefly, 1000 µl of ethyl acetate was added into 125 µl of plasma or tissue homogenate and vortexed at high speed for 5 minutes. The mixture was further centrifuged at 3500 rpm for 10 minutes to achieve a suitable phase separation. The supernatant was collected. A different extraction protocol was used for the curcumin metabolite since ethyl acetate was not an efficient solvent for its extraction. Briefly, 62.5 µl of 5M ammonium acetate was added into 125 µl plasma or tissue homogenate and mixed for 1 minute. 1000 µl of acetonitrile was added into each sample and vortexed for 5 minutes. The mixture was further centrifuged at 3500 rpm for 10 minutes and the supernatant was collected. The supernatant was further evaporated by using a vacufuge (Ependorf, Hauppauge, NY) and reconstituted with a smaller amount of methanol. The concentrated samples were analyzed using a liquid chromatography – mass spectrometry (LC-MS) and high-performance liquid chromatography (HPLC) as described in the next section. Standards were prepared by spiking a known concentration of curcumin, curcumin glucuronide, and hesperetin (internal standard) into plasma or tissue homogenates followed by the extraction protocol described for harvested samples.

3.2.6.3 HPLC and LC-MS Analysis.

HPLC analysis was carried out on a Shimadzu HPLC system (Columbia, MD). The chromatographic separation was performed on a Thermo Scientific Hypersil Gold C18 column (2.1 x 50 mm, 5 μ m). Liquid chromatographic (LC) conditions consisted of a gradient method starting with 5% acetonitrile and 95% 0.1% formic acid in water and reaching 95% acetonitrile and 5% 0.1% formic acid in water over 8 minutes, followed by 4 minutes of equilibration. The flow-rate was set to be 0.3 ml/min. The wavelength of detection was at 420 nm.

Further experiments to identify metabolites involved the scanning instrument Shimadzu LC-MS (LC20ADXR)-IT-TOF (Columbia, MD) that coupled with atmospheric pressure ionization with Ion –Trap (IT) and Time-of-Flight (TOF) technologies. Liquid chromatographic (LC) conditions consisted of a gradient method starting with 5% acetonitrile and 95% 0.1% formic acid in water and reaching 100% acetonitrile over 10.5 minutes, followed by 4.5 minutes of equilibration. Thermo Scientific Hypersil Gold C18 column (2.1 x 50 mm, 5 μ m) was used for the measurements. The flow rate was set to be 0.25 ml/min. Photodiode array (PDA) was scanned 200-800 nm over the entire LC run. MS was scanned (m/z 100-1000) in both positive and negative mode.

Both curcumin and its metabolite (curcumin glucuronide) were quantified by negative ion tandem mass spectroscopy. Analysis was performed by using a Triple Quad LC Mass Spectrometer (Agilent, 6410 QQQ, Santa Clara, CA). Separation was achieved with the same conditions as described above for LCMS-IT-TOF. Identification and quantification of curcuminoids was done by multiple reaction monitoring (MRM) using suitable transitions (curcumin 367->216.9, curcumin glucuronide 543->175 and hesperetin (IS) 301.1>163.9) after

initial full scan acquisition. Other obtained ion transitions for curcumin (367.1->148.9) and curcumin glucuronide (543->217 and 543->367) were used as qualifiers.

3.3 Results and Discussion

Polymeric PLGA nanoparticles encapsulating hydrophobic curcumin (which we call nano-curcumin) were produced by the FPaD process (described in Chapter 2). The size of the nanoparticle was characterized by the DLS and reported in **Figure 3-1**. The drying process caused certain level of permanent aggregation, so the particle size distribution is broader and the average size shifted from ~100 nm to ~125 nm after resuspension (**Figure 3-1**). After the freeze-drying process, the particles are in powder format (**Figure 3-1B**), which can be maintained stable for more than a year. The calculated drug loading and encapsulation efficiency were 47.3% and 94.7%, respectively. The final amount of curcumin in the dried-powder (nanoparticles plus excipients) was 2.4 μ g/mg.

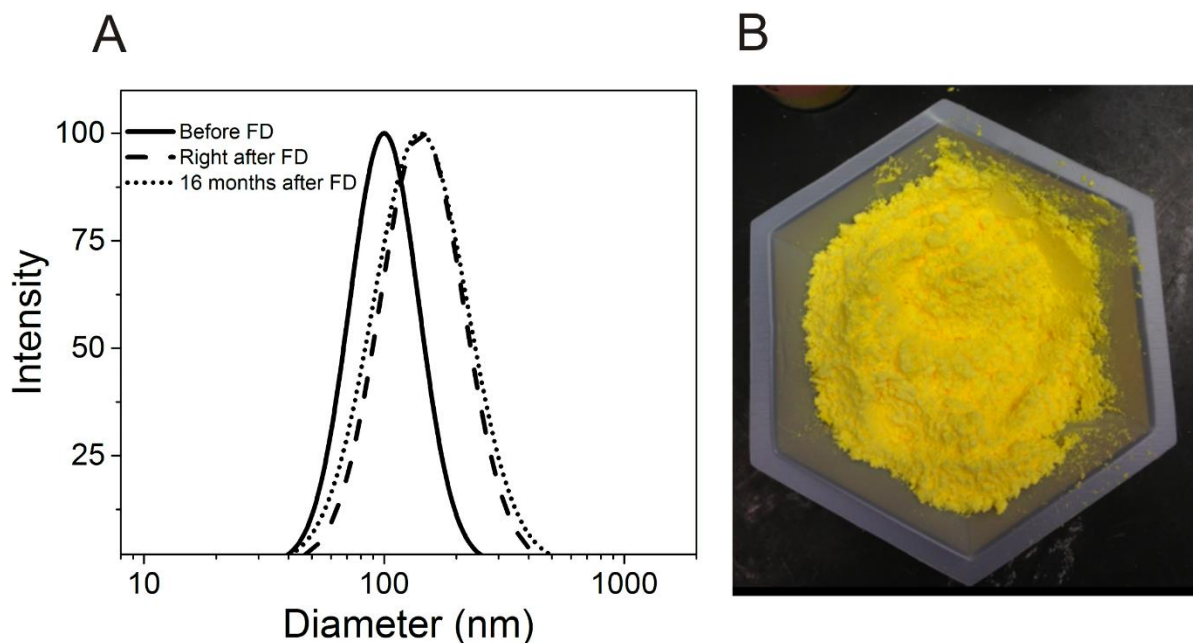


Figure 3-1. (A) The size distribution of nano-curcumin before, resuspended right after, and resuspended 16 months after freeze-drying (FD). (B) Nano-curcumin in powder format.

According to the US Pharmacopeia and Food and Drug Administration (FDA) regulations, THF has been classified as a class II solvent which needs to be limited due to its irreversible toxicity. Therefore, the final drug product has to be tested for the residual solvent content in order to comply with the set regulations. For THF, the permitted daily exposure (PDE) is 7.2mg. Our results indicated that the residual amount of THF was present in the dried powder. However, its calculated value based on the drug product applied dose was below the PDE limit (Figure 3-2).

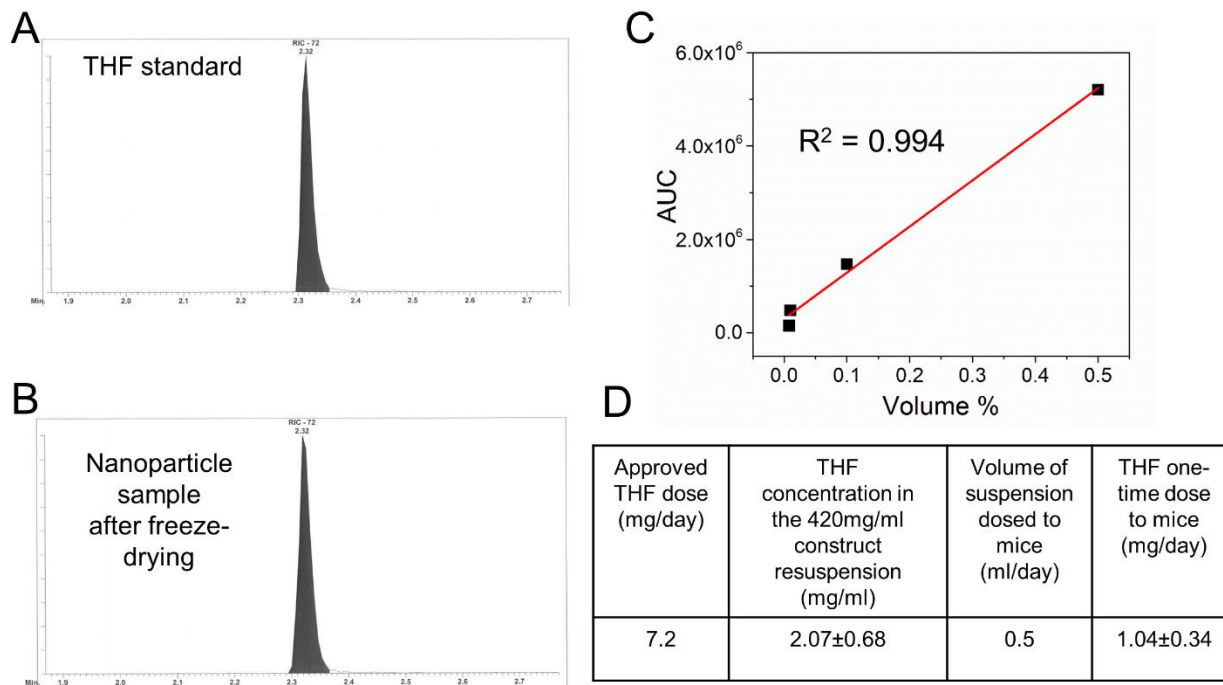


Figure 3-2. GC-MS analysis of THF. (A) Representative chromatogram for THF standard with 0.1 % concentration in water. (B) Representative chromatogram for resuspended nanoparticle in

water. The construct concentration was 420 mg/ml. The drug concentration was 1 mg/ml. (C) Linearity of the calibration standards. (D) Comparison between calculated value of THF content per applied daily dose in mice and the permitted daily exposure.

Pharmacokinetic studies after oral delivery of curcumin or curcumin formulations have been commonly performed to determine bioavailability of the compound in blood plasma and tissues. However, there has been some controversy regarding the reported results. First, curcumin is known to be highly metabolized through intestinal and hepatic glucuronidation,^{102, 103} which implies a significant biotransformation after oral administration. Literatures have reported the improved bioavailability of curcumin in plasma that was pre-treated with β -glucuronidase, resulting in hydrolysis of the glucuronide moiety.^{95, 104, 105} Detected levels of curcumin if including its metabolites do not really represent the true bioavailability of the native drug and could be misleading since the activity of the metabolites could be significantly altered as suggested by several *in vitro* studies.^{106, 107} Furthermore, the lack of detailed protocols in various pharmacokinetic studies regarding the sample pre-treatment and HPLC or LC-MS procedures that actually reported larger quantities of curcumin in plasma makes it extremely hard to understand whether curcumin was measured individually or as a combination of the native drug and its metabolites.^{94, 108}

The majority of the published work on pharmacokinetic studies of native curcumin in both rodent and human models has consistently shown poor oral bioavailability of the compound as indicated by extremely low or even undetectable concentrations in plasma. When aqueous suspension of curcumin was given at a relatively high dose of 1 g/kg in rats, the maximum detectable plasma concentration was 22 ng/ml.⁹³ On the other hand, a much lower dose (50 mg/kg) of curcumin-loaded PLGA nanoparticles has shown curcumin maximum rat plasma level

of 44 ng/ml indicating improved bioavailability.⁹³ A separate study of curcumin level in rat plasma after oral administration of curcumin loaded in low molecular weight PLGA (MW: 5-15k) nanoparticles at 50 mg/kg curcumin dose reported a peak plasma concentration of 42 ng/ml at 30 minutes after administration, which rapidly vanished to concentrations below 20 ng/ml after 1 hour.⁹¹ To the best of our knowledge only one article besides our study reported a very low dose of curcumin (23 mg/kg) encapsulated in PEG-*b*-PLA nanoparticles used to measure curcumin bioavailability in blood plasma after oral administration in mice.¹⁰⁹ In the study, dried PEG-*b*-PLA – curcumin nanoparticles were administered to mice to observe the time dependent curcumin and tetrahydrocurcumin levels in plasma and brain tissue. It was established that at an early time point of 10 minutes, the mean concentration of curcumin in plasma was found to be quite high (400 ng/ml) but with large standard deviation. However, it then quickly diminished to approximately 10 ng/ml levels around 40 minutes. The curcumin level in brain for this low oral dose peaked at 20 ng/g, which is an evidence that curcumin crossed the blood-brain barrier (BBB).¹⁰⁹

The dose tested here for our nano-curcumin is relatively low (20 mg/kg) as this is a feasible amount of curcumin that could be safely administered daily in humans without undesired side effects.¹¹⁰ Furthermore, we have recently demonstrated that nano-curcumin at this relatively low dose (20 mg/kg) was highly efficacious in attenuating morphine tolerance and dependence in rodent models.^{64, 65} At the same dosing level, negligible amount of curcumin can be detected after oral administration of the unformulated curcumin. As a comparison, a much higher dose (400 mg/kg) of aqueous suspension of native curcumin has to be used to achieve comparable amount of curcumin in plasma, brain, and spinal cord.

Quantification of curcumin and curcumin glucuronide was obtained and extrapolated on the calibration curve. The calibration lines were shown to be linear from 0.122 ng/ml to 250 ng/ml ($r^2 > 0.99$) for curcumin and 0.98 ng/ml to 2000 ng/ml ($r^2 > 0.991$) for curcumin glucuronide standards extracted from plasma, brain, and spinal cord homogenates (**Figure 3-3**). Internal standard (IS) calibration was also used to quantify the results (**Figure 3-3B** and **3-3D**). However, no significant difference in data quality was found when comparing both internal and external standardization (ES) (**Figure 3-4**).

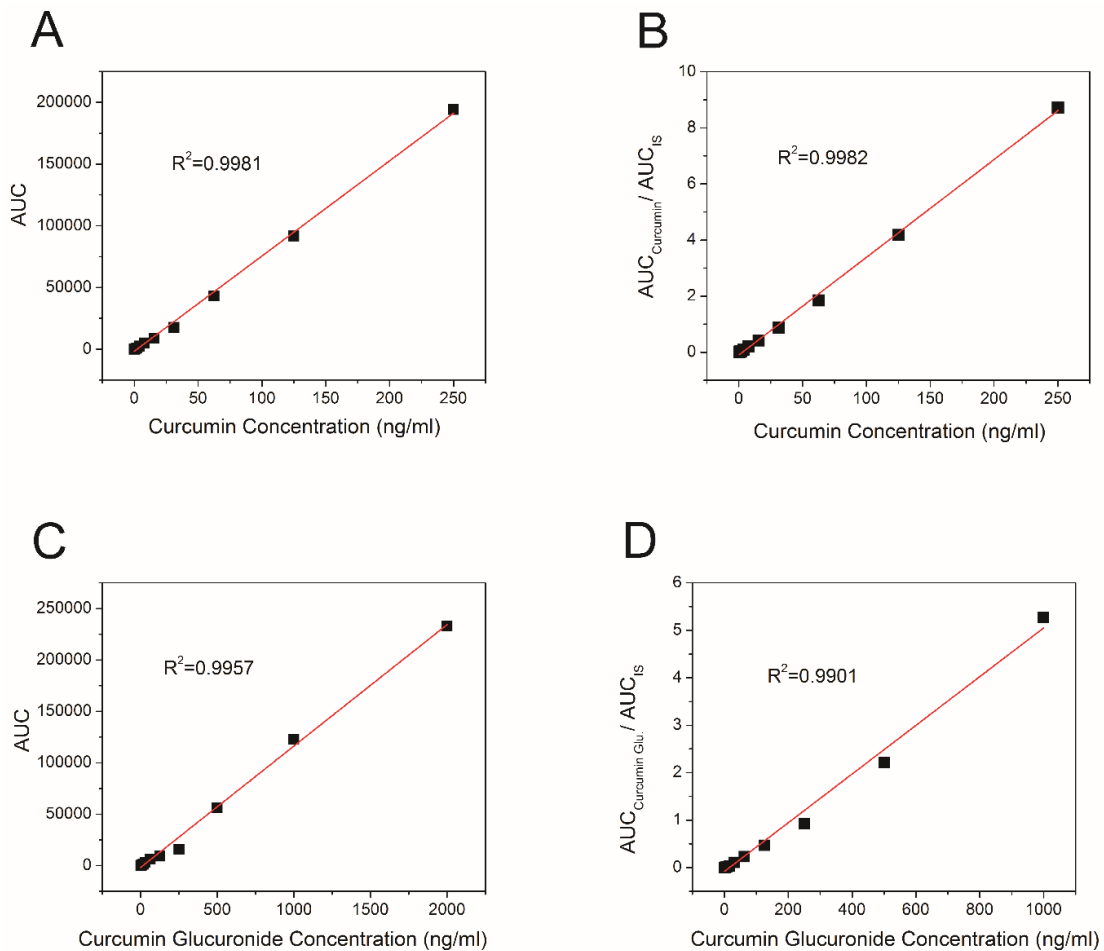


Figure 3-3. Examples of calibration curves with and without IS for curcumin (A, B) and curcumin glucuronide (C, D) standards extracted from plasma.

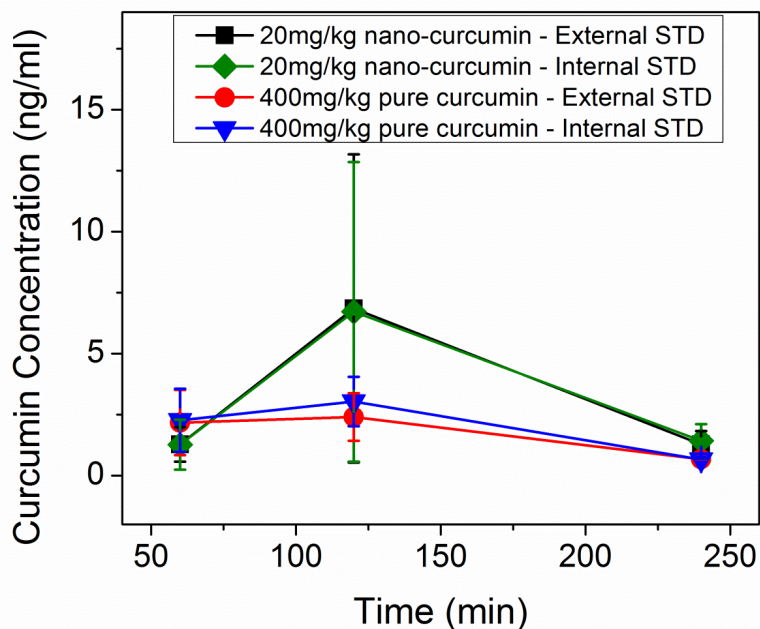


Figure 3-4. Quantification of curcumin in plasma using internal and external calibrations. No significant differences were observed.

The method of quantification was validated by performing quality control experiments. The known concentrations of curcumin and its metabolites were first spiked into blank plasma and tissues and extracted. The percentile of extraction was calculated for curcumin and curcumin glucuronide and reported in **Table 3-1** and **Table 3-2**, respectively.

Table 3-1. Quality-control samples for extraction of curcumin from plasma, brain, and spinal cord with ethyl acetate.

Quality Control	Nominal Concentration (ng/ml)	Trial 1	Trial2	Trial3	Average	% Extraction	% Error (+/-)
Plasma Q1	15.63	17.38	15.80	14.60	15.93	101.95	4.70
Plasma Q2	3.906	4.64	3.91	3.76	4.10	105.03	4.34

Plasma Q3	0.98	0.99	0.98	0.96	0.98	100.28	1.50
Brain Q1	15.63	16.93	16.82	16.94	16.89	108.12	0.40
Brain Q2	3.91	4.91	3.65	3.69	4.08	104.55	6.11
BrainQ3	0.98	1.03	0.99	0.95	0.99	101.34	2.36
Spinal Cord Q1	15.63	15.72	17.45	-	16.59	106.15	3.93
Spinal Cord Q2	3.91	3.92	4.08	-	4.00	102.48	1.47
Spinal Cord Q3	0.98	1.15	0.89	-	1.02	104.56	9.25

Table 3-2. Quality-control samples for extraction of curcumin glucuronide from plasma, brain, and spinal cord with acetonitrile.

Quality Control	Nominal Concentration (ng/ml)	Trial 1	Trial2	Average	% Extraction	% Error (+/-)
Plasma Q1	250.00	208.10	170.66	189.38	75.75	7.49
Plasma Q2	62.50	46.16	47.41	46.78	74.85	1.00
Plasma Q3	15.63	13.51	11.74	12.62	80.79	5.68
Plasma Q4	1.95	1.45	1.58	1.51	77.55	3.25
Brain Q1	250.00	186.74	168.27	177.51	71.00	3.69
Brain Q2	62.50	46.04	44.85	45.44	72.70	0.95
BrainQ3	15.63	11.79	13.07	12.43	79.56	3.51
BrainQ3	1.95	1.24	1.29	1.27	64.92	0.30

Spinal Cord Q1	250.00	200.05	162.24	181.14	72.46	7.56
Spinal Cord Q2	62.50	44.16	48.40	46.28	74.05	3.39
Spinal Cord Q3	15.63	12.89	11.79	12.34	79.00	3.51
Spinal Cord Q3	1.95	1.31	1.32	1.31	67.20	0.30

The specificity of the method was further confirmed by comparing chromatograms of the control samples (curcumin extracted from the blank plasma/brain/spinal cord spiked with curcumin standards) and the measured samples (curcumin extracted from plasma/brain/spinal cord after oral delivery of nano-curcumin). The example of the specificity, demonstrating that there is no interference from the brain and spinal cord matrix components, was presented in **Figure 3-5**. The figure also demonstrated that curcumin infiltrated through the blood-brain barrier (BBB) as it was present in the brain and the spinal cord at early time-points when the mice were administered with a small dose (20 mg/kg) of nano-curcumin.

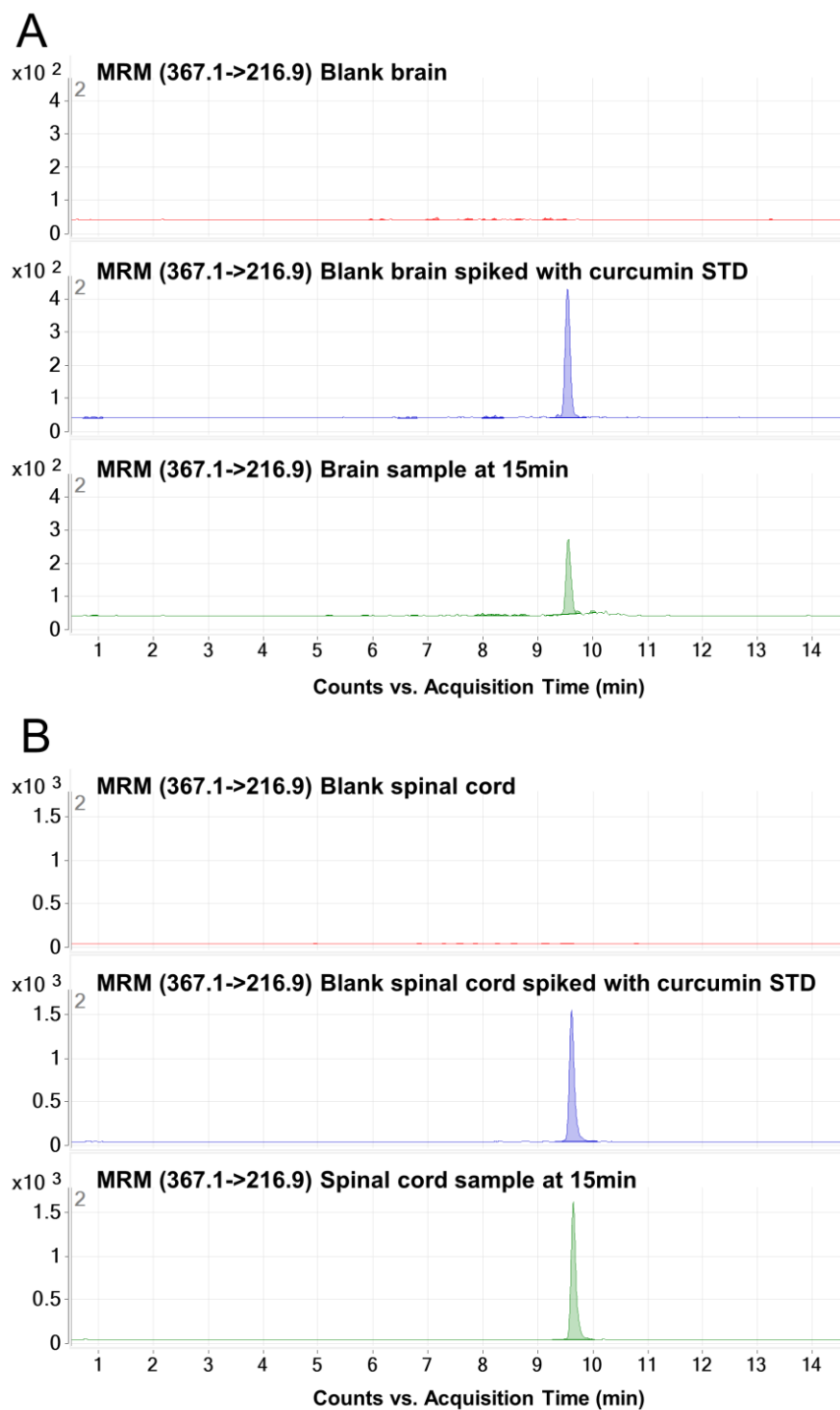


Figure 3-5. Representative chromatograms of curcumin extracted from (A) brain and (B) spinal cord. The top one (in red) is the chromatogram of blank tissues. The middle one (in blue) is the chromatogram of curcumin extracted from tissues spiked with curcumin standard. The bottom

one (in green) is the chromatogram of curcumin extracted from tissue samples 15 minutes after oral delivery of low-dose (20 mg/kg) nano-curcumin. The analysis uses ion transition for curcumin (367.1>216.9).

The amount of curcumin measured in the CNS at various time points was presented in **Figure 3-6A** and **B**. The LC-MS analysis revealed comparable curcumin levels in both brain and spinal cord tissues after oral delivery of low dose (20 mg/kg) nano-curcumin and high dose (400 mg/kg) native curcumin. This correlates with our previous studies of mouse behaviors that showed similar efficacy of low dose nano-curcumin (20 mg/kg) and high dose curcumin (400 mg/kg) on blocking morphine tolerance and dependence.^{64, 65}

In order to compare with the efficacy studies in rodent animals, it is important to unambiguously determine the amount of curcumin in CNS within 15 minutes after dosing. This early pharmacokinetic time frame is of great importance since the effects on morphine tolerance and dependence reversal and prevention in both acute and chronic models were observed when nano-curcumin or pure curcumin were administered orally 15 minutes prior to tested doses of morphine.⁶⁵

The presence of curcumin in both brain and spinal cord in the first 30 minutes after the dosages (**Figure 3-6**) provided another support of our hypothesis that curcumin in the CNS suppressed the function of CaMKII α that was implicated in the development of opioid tolerance and dependence.¹¹¹ The curcumin plasma levels were reported in **Figure 3-6C**. The results indicated that curcumin was readily absorbed in the blood stream and rapidly distributed in the tissues due to its lipophilic nature. The fast decrease of curcumin concentration in plasma could also be an indication of its quick metabolism.

The critical pharmacokinetic parameters including the peak concentration (C_{max}), the time of the peak concentration (T_{max}), and the area under the curve (AUC) were presented in **Table 3-3**. The area under the curve for the investigated time (0-240 min) (AUC_{0-240}) was calculated using a linear trapezoid rule. The AUC_{0-250} values for nano-curcumin (20 mg/kg) in plasma, brain, and spinal cord were approximately 78, 3, and 6 times higher when compared with the unformulated curcumin at the same dose (20 mg/kg).

Table 3-3. Pharmacokinetic parameters of curcumin levels in plasma, brain, and spinal cord after oral delivery of nano-curcumin (20 mg/kg) and pure curcumin suspensions (20 mg/kg and 400 mg/kg).

	20 mg/kg nano-curcumin	20 mg/kg pure curcumin	400 mg/kg pure curcumin
Brain			
T_{max} (min)	3.00	15.00	5.00
C_{max} (ng/ml)	12.71±6.63	2.03±0.69	30.32±3.10
AUC_{0-240} (ng/g x min)	185.55±71.56	58.86±31.12	252.52±110.71
Spinal cord			
T_{max} (min)	7.50	7.50	5.00
C_{max} (ng/ml)	85.88±54.27	23.49±11.57	129.16±63.12
AUC_{0-240} (ng/g x min)	2878.64±973.82	454.59±237.51	5154.62±2055.07
Plasma			
T_{max} (min)	3.00	15.00	3.00
C_{max} (ng/ml)	41.33±16.03	0.60±0.44	79.82±49.00
AUC_{0-240} (ng/ml x min)	686.14±366.22	8.73±5.43	618.83±269.04

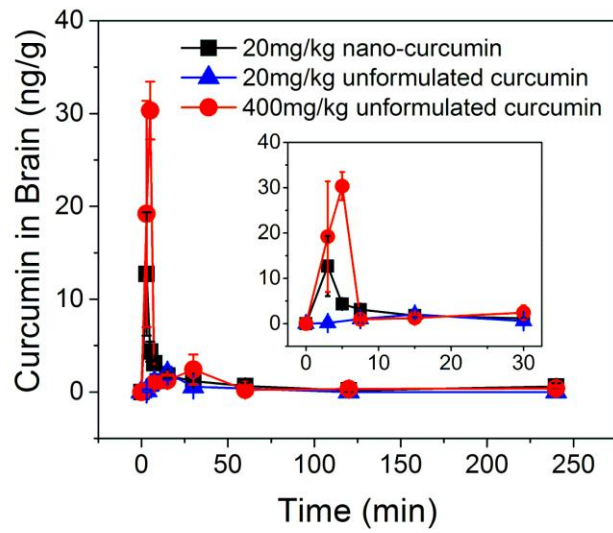
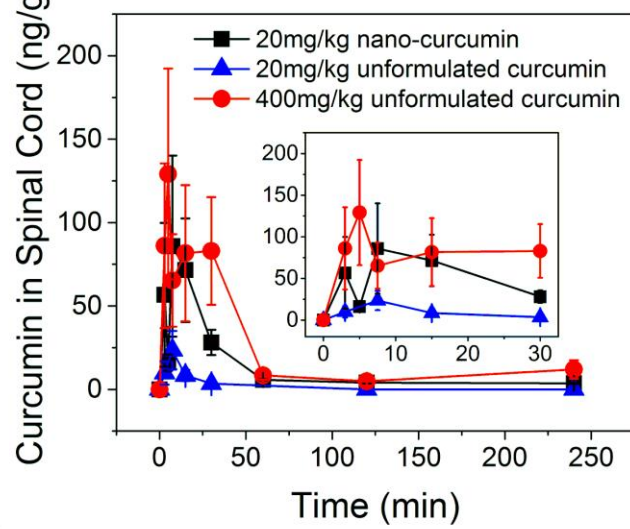
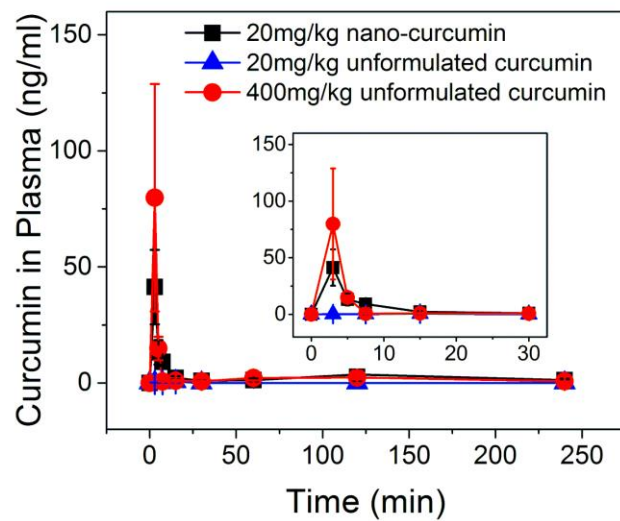
A**B****C**

Figure 3-6. The amount of curcumin measured in (A) brain, (B) spinal cord, and (C) plasma after oral administration of low-dose (20 mg/kg) nano-curcumin (black symbols and lines), low-dose (20 mg/kg) pure curcumin (blue symbols and lines), and high-dose (400 mg/kg) pure curcumin (red symbols and lines). All values are reported as the mean \pm S.E.M (n=4).

The LC-MS analysis also proved that curcumin was quickly metabolized after oral administration. Large quantities of curcumin glucuronide reaching $\mu\text{g/ml}$ levels were detected in plasma after oral dosage of nano-curcumin. On the other hand, low-dose and high-dose of native curcumin resulted in much lower concentrations of the metabolite with maximum concentrations of 10n g/ml and 282 ng/ml, respectively (**Figure 3-8B and Table 3-4**). The area under the concentration curve increased approximately 450 and 4.7 times for nano-curcumin when compared with the unformulated curcumin at the same dose and 20 times higher dose, respectively (**Table 3-4**). The most likely reason was that the sustained release of curcumin from nanoparticles supports constant metabolism of the compound, while native curcumin after oral dosage is quickly eliminated from the body. No metabolite was detected in brain or spinal cord tissues. It is noteworthy that the method used here for the quantification of curcumin metabolite allows for its direct measurement without the need for the hydrolysis of the glucuronide moiety. This offered a more robust and reliable way of compound characterization with the benefits of rapid sample preparation and better accuracy, as the hydrolysis might result in incomplete deconjugation and non-specific matrix binding in the hydrolytic environment.

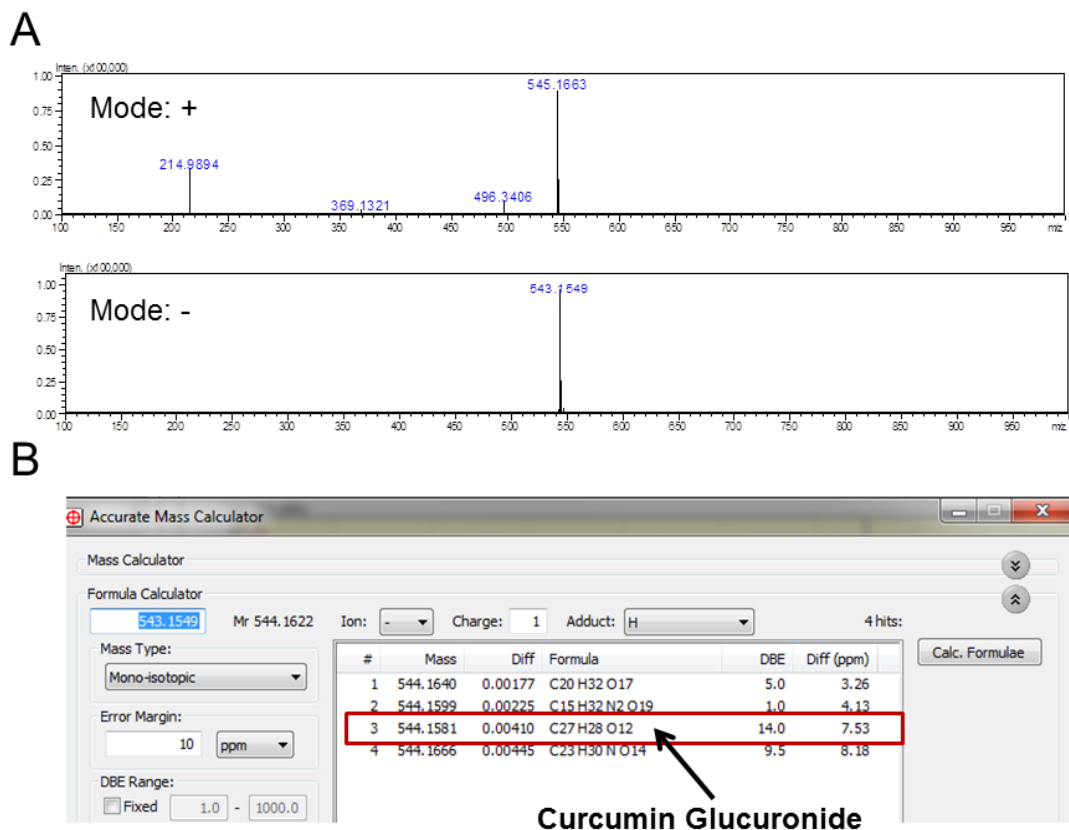


Figure 3-7. Identification of the major curcumin metabolite in plasma. (A) Detection of curcumin glucuronide by negative and positive ionization. (B) Confirmation of the molecular weight by the accurate mass calculator.

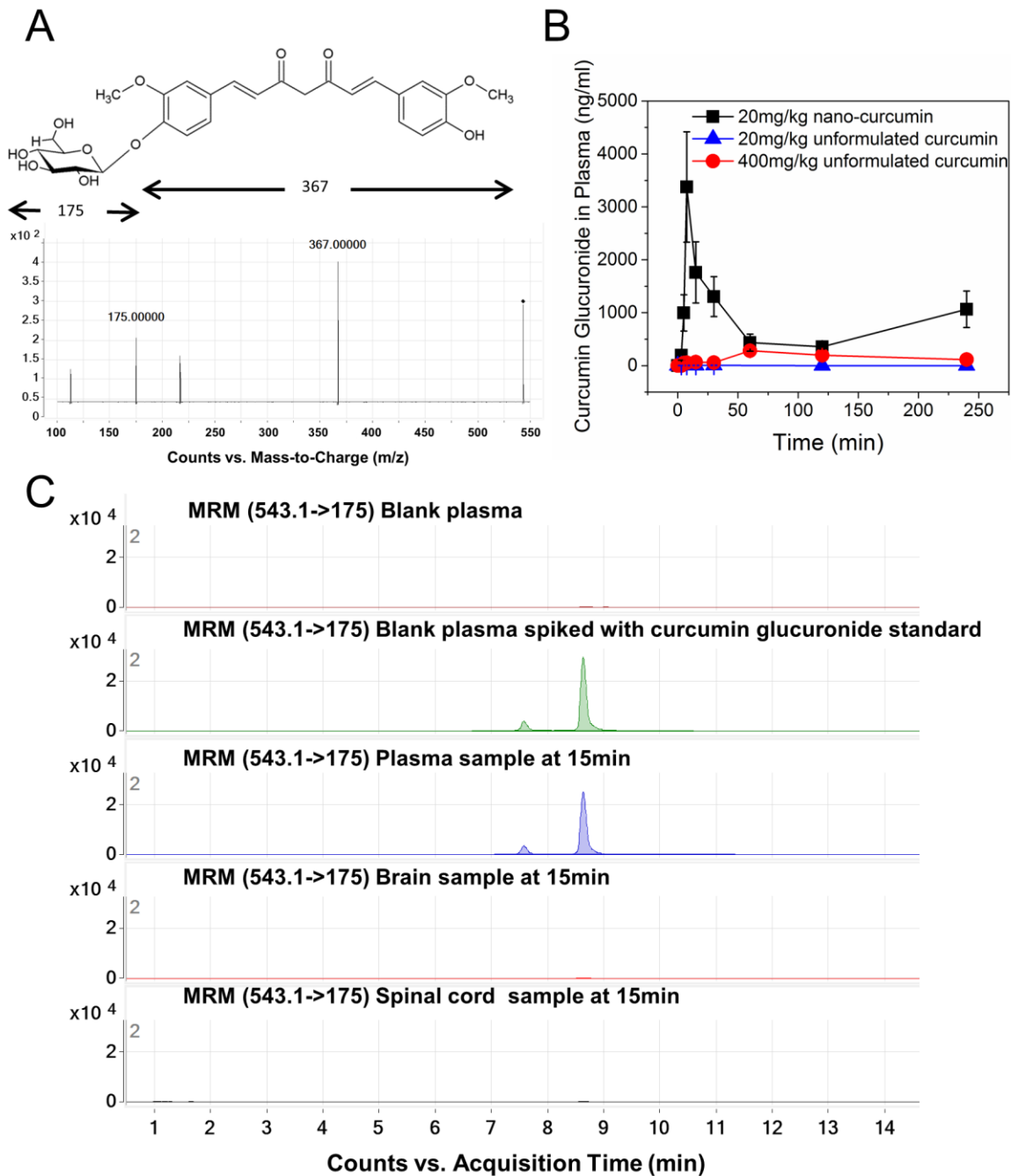


Figure 3-8. (A) MS/MS spectrum of curcumin glucuronide showing precursor to product ion transition. (B) The amount of curcumin glucuronide measured in plasma after oral administration of low-dose (20 mg/kg) nano-curcumin, low-dose (20 mg/kg) pure curcumin and high-dose (400 mg/kg) pure curcumin. All values are reported as the mean \pm S.E.M (n=4). (C) Representative chromatograms for blank plasma, blank plasma spiked with curcumin glucuronide standard, and

plasma, brain and spinal cord tissue samples collected 15 minutes after oral delivery of low-dose (20 mg/kg) nano-curcumin. The analysis used ion transition for curcumin glucuronide (543.1>175).

Table 3-4. Pharmacokinetic parameters for curcumin glucuronide in plasma after oral administration of low-dose (20 mg/kg) nano-curcumin, low-dose (20 mg/kg) pure curcumin, and high-dose (400 mg/kg) pure curcumin.

Plasma	20mg/kg nano-curcumin	20mg/kg pure curcumin	400mg/kg pure curcumin
T _{max} (min)	7.50	30	60.00
C _{max} (µg/ml)	3.38±1.04	0.01±0.00	0.28±0.05
AUC ₀₋₂₄₀ (µg/ml x min)	184.24±52.55	0.41±0.07	39.60±9.22

It is important to precisely detect the level of curcumin glucuronide separately. The *in vitro* efficacy of curcumin glucuronide has been investigated by several groups. However, no empirically satisfactory conclusion has been drawn regarding its potency. It has been observed that while curcumin exhibited a great anticancer activity resulting in 100% cell death, its metabolite (curcumin glucuronide) did not show any suppression of cell proliferation against KBM-5, U266, or Jurkat cell lines.¹⁰⁶ Shoji et al. compared the effects of curcumin and curcumin glucuronide in human hepatocellular carcinoma (HepG2) cells and found much weaker effects of the metabolite when compared with the native drug. The difference in the activity between curcumin and curcumin glucuronide was mainly caused by the different rate of cell uptake of the compounds.¹¹² On the contrary, some initial investigations suggested that polyphenol glucuronide compounds could play an active role in the treatment of some of the diseases and

medical conditions through natural deconjugation into a parent compound at the site of inflammation or necrotic regimes of certain types of human tumors.¹¹³⁻¹¹⁵ The mechanism allowing for this action involved overexpression of β -glucuronidase – an enzyme that is responsible for cleavage of the glucuronide moiety in these microenvironments. The glucuronide conjugates of compounds, such as quercetin and luteolin that come from the same polyphenol, functional food family as curcumin, were studied and reported to be capable of deconjugation. In inflammation, β -glucuronidase is known to be released from granulocytes including neutrophils.¹¹⁶ When human neutrophils were incubated with ionomycin/cytochalasin B (inflammation inducers), the luteolin glucuronide was converted to the native drug. Furthermore, it was demonstrated that deconjugation was achieved *in vivo* by feeding mice or rats with quercetin or luteolin, and treating (by intraperitoneal injection) them with liposaccharides (LPC), which are known to lead to inflammation. The levels of the free native and conjugated form of the drug were tested after sacrificing the animals. It was determined that the plasma and tissue levels of the metabolite were significantly reduced upon the inflammatory response, clearly indicating its deconjugation.^{113, 114}

The levels of curcumin glucuronide captured here in our study were remarkably higher for the low-dose nano-curcumin samples when compared to high-dose unformulated curcumin. This significantly higher bioavailability of the curcumin glucuronide in plasma when using nanoparticles might present a novel therapeutic strategy by employing deconjugation of the metabolite at the specific sites such as inflammation.

3.4 Conclusions

In this study, we investigated the bioavailability of curcumin and curcumin glucuronide in blood plasma and CNS after oral intake of nano-curcumin and native curcumin in mice. The highly sensitive and validated methods of detection distinguished curcumin from its major metabolite, curcumin glucuronide. The results showed similar concentrations of curcumin in CNS tissues after oral dosage of nano-curcumin 20 times lower compared to the dosage of unformulated curcumin, which fully support the conclusions drawn by our previous study of curcumin effects of preventing and reversing morphine tolerance and dependence using animal behavioral models.⁶⁵ The presence of curcumin in CNS in the first 15 – 30 minutes is essential for suppressing the activity of CaMKII α for the development of opioid tolerance and dependence. The detected curcumin glucuronide level in blood plasma was significantly higher using the nano-curcumin compared to 20 times higher dose of native curcumin, which might provide a chance to further increase curcumin bioavailability by deconjugation of curcumin glucuronide triggered by codelivery of β - glucuronidase at a specific site such as inflammation.

4 CHARACTERIZATION OF PHYSICAL STRUCTURES OF POLYMERIC NANOPARTICLES BY USING SMALL ANGLE X-RAY SCATTERING

4.1 Introduction

Amphiphilic polymers have become an incredibly important class of polymers in recent years due to their spontaneous self-assembly in aqueous solutions into polymeric micelles of core-shell structure.^{117, 118} The core of this particular kind of the particles composes of a collapsed hydrophobic part of the polymer while the shell is represented by the hydrophilic polymer blocks. This core-shell structure of polymeric assemblies has been considered a desired morphology for delivery of hydrophobic compounds.^{119, 120} The hydrophobic core of the particles represents a cargo space for the incorporation of hydrophobic drugs into a dense polymer matrix. The outer shell, on the other hand, serves as a stabilizing barrier between the core of the particle and the external environment.

Many studies have demonstrated the use of polymeric core-shell assemblies for biomedical applications. The most common and well-studied systems are represented by the core-shell particles from simple linear di- or tri-block copolymers such as poly(ethylene oxide)-*b*-poly(caprolactone) (PEO-*b*-PCL), poly(ethylene oxide)-*b*-poly(lactic acid) (PEO-*b*-PLA), poly(ethylene oxide)-*b*-polystyrene (PEO-*b*-PS), poly(lactic acid)-*b*- poly(ethylene oxide)-*b*-poly(lactic acid) (PLA-*b*-PEO-*b*-PLA), and the whole class of pluronics.¹²¹⁻¹²⁴ These types of particles have been routinely used for the encapsulation of hydrophobic compounds and further implementation in studies of *in vitro* solubility and release and *in vivo* pharmacokinetics. In addition, the studies of structural and morphological features of these particular systems by

means of various techniques such as DLS, static light scattering (SLS), TEM as well as more sophisticated structure characterization with small angle x-ray or neutron scattering techniques (SAXS or SANS) are known and reported in literature.^{117, 125-127}

While simple linear block copolymer micelles have gained a lot of attention as valuable drug carriers, much less was explored for polymeric core-shell particles composed of more complex macromolecular building blocks such as brush amphiphiles, also known as graft copolymers. Some initial investigations showed that the micelles composed of the graft copolymers had the ability of higher drug encapsulation and sustaining drug release when compared with their linear analogs.¹²⁸ Furthermore, one recent study demonstrated a wide morphological diversity of these polymeric assemblies by manipulating the ratios and lengths of the amphiphilic graft copolymers and their self-assembly conditions. The structural information in this study was given by the TEM images. Although the overall structure of the particles could be relatively easily observed by this technique, the internal core-shell architecture is not possible to be distinguished.¹²⁹ No further studies are known to report the internal structural features of these types of particles.

Herein, we investigated the internal structures of the polymeric micelles formed from simple linear diblock copolymers, and for the first time we studied the assemblies of novel brush amphiphiles by employing state-of-the-art SAXS measurements. The ability of the SAXS to test samples in their liquid environments and fast measurement time makes it a desired technique of nanostructure characterization. The core-shell modeling was applied to fit the acquired SAXS data and allowed for high structural information content revealing the size of the core, shell, and the aggregation number of the polymeric micelles. Two distinct morphologies for the studied polymeric micelles, core-shell spheres and core-shell cylinders, were identified.

4.2 Experimental Procedures

4.2.1 Materials and Reagents

THF was purchased from Sigma-Aldrich (St Louis, MO). PEG-*b*-PCL (Mn 5000-*b*-3600) and PEG-*b*-PCL (Mn 5000-*b*-6000) were purchased from Polymer Source (Dorval, Canada). Linear PEG-*b*-PLA polymers and all brush polymers were a kind gift of Dr. Margarita Herrera-Alonso (Johns Hopkins University, Baltimore, MD, US).

4.2.2 Micelle Formation

Amphiphilic linear or brush polymers were first dissolved in THF. The concentrations are reported in the **Results and Discussion** section (**Table 4-3**). The self-assembly of the nanoparticles was carried out in a MIVM. One of the four inlet streams had polymer dissolved in THF. The other three inlet streams consisted of deionized water as an anti-solvent to precipitate the polymer. The flow rate of stream 1 (organic stream) and 2 was set to be 9 ml/min and 36 ml/min for streams 3 and 4. The final ratio of THF to water was 1:9.

4.2.3 Dynamic Light Scattering (DLS) Measurements

Polymeric micelle sizes and size distribution were measured by DLS (Brookhaven, NanoDLS, Holtsville, NY). The size of the particles was reported as the volume-weighted diameter. The values for viscosity and refractive index were set to be 0.890 cP and 1.331, respectively.

4.2.4 Transmission Electron Microscopy (TEM) Imaging

Carbon-coated copper TEM grids (Electron Microscopy, Hatfield, PA) were ionized under plasma before sample preparation. A 20 μ L drop of nanoparticle suspension was placed on the carbon grids, which was left for 5 minutes before washing with five (20 μ L) drops of DI

water. A drop containing 2% aqueous uranyl acetate solution was then placed on the carbon grids for 30 seconds before the excess solution was absorbed with the filter paper. The samples were allowed to dry at room temperature prior to imaging.

4.2.5 SAXS Measurements

The SAXS measurements were performed at the synchrotron X-ray beam line BioCAT 18ID at Argonne National Laboratory. The exception was for two linear PEG-*b*-PLA samples that were tested at DND-CAT 5ID at Argonne National Laboratory. The samples were flown into a capillary cell by a programmed pump (Hamilton, MICROLAB® 500 Series, Reno, NV). The detector (Pilatus 1M) was positioned 2.5 m away from the samples resulting in the range of Q from 0.006 \AA^{-1} to 0.35 \AA^{-1} . The X-ray exposure time and acquisition time were 0.2 s and 5 s, respectively. Ten images were taken for each sample to obtain good statistics. The buffer (dialysis water) was run before an actual sample, so the scattering patterns of the buffer could be subtracted from the scattering patterns of the samples to result the scattering information solely from the polymeric nanostructures. Furthermore, the empty capillary as well as the capillary filled with Millipore water was also tested in order to calculate the absolute scaling of the data.

4.3 Modeling of SAXS Data

The post-experimental analysis for the samples was done by using ATSAS Primus¹³⁰ and SasView software (open access: <http://www.sasview.org/>). ATSAS Primus was mainly applied to manipulate the experimental SAXS data and apply operations such as averaging, merging, scaling, subtracting of a blank (buffer solution without any nanoparticles), estimating the radius of gyration of the nanoparticles, and obtaining nanoparticle structural features in the form of a pair distribution function $p(r)$. The SasView software was further implemented to perform core-

shell modeling of the data by using the non-linear-least-squares method to reveal structural features of the polymeric micelles.

The micelles in this study were expected to be of either spherical or cylindrical shape with unique core-shell architecture. Therefore, a core-shell sphere and core-shell cylinder models were used.

The scattering intensity $I(q)$ is proportional to the product of $S(q)$ and $P(q)$, where $S(q)$ is a structure factor that determines the interparticle interactions and $P(q)$ is a form factor determining the nanostructure size and shape. Since the micelles are diluted, the $S(q)$ can be neglected ($S(q)=1$) and the $I(q)$ will be proportional to $P(q)$ only. The core-shell sphere model provides the form factor $P(q)$ that is normalized by the particle volume. The scattering intensity is then calculated by the following equation,⁵²

$$P(q) = \frac{scale}{V_s} \left[3V_c(\rho_c - \rho_s) \frac{[\sin(qR_c) - qR_c \cos(qR_c)]}{(qR_c)^3} + 3V_s(\rho_s - \rho_{solv}) \frac{[\sin(qR_s) - qR_s \cos(qR_s)]}{(qR_s)^3} \right]^2 + bkg$$

where V_s and V_c are the volumes of the outer shell and core, respectively; R_s and R_c are the radii of the shell and core, respectively; ρ_s , ρ_c , and $\rho_{solvent}$ are the scattering length densities of the shell core, and solvent, respectively; $scale$ is a scale factor that equals to volume fraction when the data are on an absolute scale, and the bkg is the background level.

In the cylindrical core-shell model, the form factor $P(q,\alpha)$ is calculated according to the formula,¹³¹

$$P(q, \alpha) = \frac{scale}{V_s} f^2(q) + bkg$$

$$f(q) = 2(\rho_c - \rho_s)V_c \frac{\sin \left[qL \cos \left(\frac{\alpha}{2} \right) \right]}{\left[qL \cos \left(\frac{\alpha}{2} \right) \right]} \frac{J_1[qR_c \sin(\alpha)]}{[qR_c \sin(\alpha)]}$$

$$+ 2(\rho_s - \rho_{solvent})V_s \frac{\sin \left[q(L + 2t) \cos \left(\frac{\alpha}{2} \right) \right]}{\left[q(L + 2t) \cos \left(\frac{\alpha}{2} \right) \right]} \frac{J_1[q(R_c + t) \sin(\alpha)]}{[q(R_c + t) \sin(\alpha)]}$$

$$V_s = \pi(R_c + t)^2(L + 2t)$$

where α is the angle between the axis of the cylinder and the q -vector, V_s and V_c are the volumes of the outer shell (i.e. the total volume, including the shell) and core, respectively; L is the length of the core, t is the thickness of the shell, R_c is the radius of the core, ρ_s , ρ_c , and $\rho_{solvent}$ are the scattering length densities of the shell, core, and solvent, respectively, $scale$ is a scale factor, and the bkg is the background level, and J_1 is the first order Bessel function.

Molecular constrains are used in the fits in order to reduce the number of fitting parameters. For both models, the parameters such as $\rho_{solvent}$ and ρ_c were known and fixed. Since the samples were dialyzed against DI water, the $\rho_{solvent}$ represents the scattering length density of water. The scattering length density of the core (ρ_c) should correspond to the scattering length density of the hydrophobic part of copolymer. For simple diblock copolymer micelles, it is reasonable to assume that was close to 100% of the hydrophobic copolymer (PCL or PLA) collapses to form a densely packed core while the majority of the hydrophilic PEG remains in the micelle corona. For the brush polymers, the hydrophobic core consists of the hydrophobic backbone PGMA as well as the hydrophobic arms of PLA. Since PGMA polymer corresponds only to a small volume fraction of the core (~10%), the scattering length density of the hydrophobic core could be approximated to be the one for PLA. Furthermore, the NMR measurements of the PEG surface content revealed that some % of hydrophilic PEG could get

incorporated into the core of the nanoparticles (**Table 4-1**) slightly lowering its scattering length density.

Table 4-1. Percentage of PEG on the surface of micelles by NMR.

Brush Polymer	% PEG on micelles surface
PGMA _{68-g} -PEG ₁₆ /PLA ₁₇	43.33
PGMA _{72-g} -PEG ₄₅ /PLA ₃₃	71.4
PGMA _{721-g} -PEG ₄₅ /PLA ₂₉	87.75
PGMA _{64-r} -(PPEG ₂₂ Ma) ₅	92.98

The scattering length density of the core was first fixed to correspond to the PLA scattering length density value and manipulated accordingly if necessary to achieve the best fit. The lower limit of the scattering length density of the core was calculated according to the following linear combination,

$$\rho_c = x_{PGMA}\rho_{PGMA} + x_{PLA}\rho_{PLA} + x_{PEG}\rho_{PEG}$$

where x_{PGMA} , x_{PLA} , and x_{PEG} are the volume fraction of PGMA, PLA, and PEG in the core and ρ_{PGMA} , ρ_{PLA} , and ρ_{PEG} are their corresponding scattering length densities. The scattering length densities of the main species used in the study with their corresponding mass densities are reported in **Table 4-2**. These values were computed using the following relation,

$$\rho_{sld} = \frac{\rho N_a \sum c_i b_i}{MW}$$

where ρ is the bulk density of the compound, N_A is Avogadro's number, a_i is the stoichiometric coefficient of atom i , f_i is the scattering length contribution of atom i , and MW is the molecular weight of the monomer subunit.

Table 4-2. Scattering length densities (SLDs) of water and polymers.

Chemical Name	Formula	Density (d) (g/cm ³)	SLD (ρ) (Å ⁻²)
Water	H ₂ O	1.00	9.45e-06
Poly caprolactone (PCL)	(C ₆ H ₁₀ O ₂) _n	1.145	1.06e-05
Poly lactic acid (PLA)	(C ₃ H ₄ O ₂) _n	1.29	1.16e-05
Poly(glycidyl methacrylate) (PGMA)	(C ₇ H ₁₀ O ₃) _n	0.805	7.33e-06
Poly(ethylene glycol) (PEG)	H(C ₂ H ₄ O) _n -OH	1.13	1.05e-05

The scale factor (*scale*) is another parameter that is held constant during analysis. We performed absolute scaling of our data in order to minimize the amount of parameters that need to be fitted. The absolute scaling was done by using water as a calibration standard as previously reported.¹³² This allowed us to fix the *scale* to be equal to the volume fraction of the micelles in the suspensions.

Size polydispersity was also included in the modeling by a lognormal distribution of the core radius. The polydispersity data obtained from the DLS measurements allowed to hold this parameter fixed during the fitting procedures.

The parameters that are left floating during the analysis for both models include t ($t = R_s - R_c$), R_c , L , and the ρ_s . These fit parameters are further used to calculate some important structural parameters of the micelles according to the following guidelines.

- (1) Use obtained fitted parameters (R_c , t , L) to calculate V_c and V_s .

(2) Calculate the aggregation number ($Agg\#$) according to the formula,

$$Agg\# = \frac{V_c}{V_{hydrophobic\ unit\ from\ single\ polymer}}$$

(3) Calculate the total volume of PEG in the shell,

$$V_{s-PEG} = Agg\# V_{PEG\ from\ single\ polymer}$$

(4) Calculate %PEG in the shell,

$$\%PEG = 100 \frac{V_{s-PEG}}{V_s}$$

(5) Compute the scattering length density of the shell (ρ_s) based on the volume fraction of

PEG (x_{PEG}) in the shell (remaining part is water),

$$\rho_s = x_{PEG} \rho_{PEG} + (1 - x_{PEG}) \rho_{water}$$

(6) Compare the calculated ρ_s with the fitted value of ρ_s .

(7) If the difference between the calculated and fitted ρ_s is large or the statistical variance in the form of χ^2 is large, modify the fixed parameters such as ρ_c , and perform subsequent modeling and computation procedures.

4.4 Results and Discussion

SAXS is a powerful technique for nanostructure characterization. The difference in the electron density of hydrophobic and hydrophilic components of the polymers and the surrounding medium can give enough contrast to distinguish unique internal features of the core-shell assemblies. These internal characteristics such as the size of the core and the thickness of the shell are here of great importance since they directly influence nanoparticle properties such as drug loading and stability. Larger core size has the benefit of greater cargo space with higher drug loading capability. The shell thickness and the surface density of the hydrophilic polymer

impact colloidal stability of nanoparticles in solution as well their biodistribution fate and pharmacokinetic parameters.¹³³ In this study, we have looked at equilibrium structures of polymeric micelles that were composed of simple linear diblock copolymers and for the first time more complex macromolecular building block such as brush polymers. The molecular structures of the studied polymers were listed in **Figure 4-1**. Polymers composed of different lengths of the hydrophobic and hydrophilic blocks were summarized in **Table 4-3**.

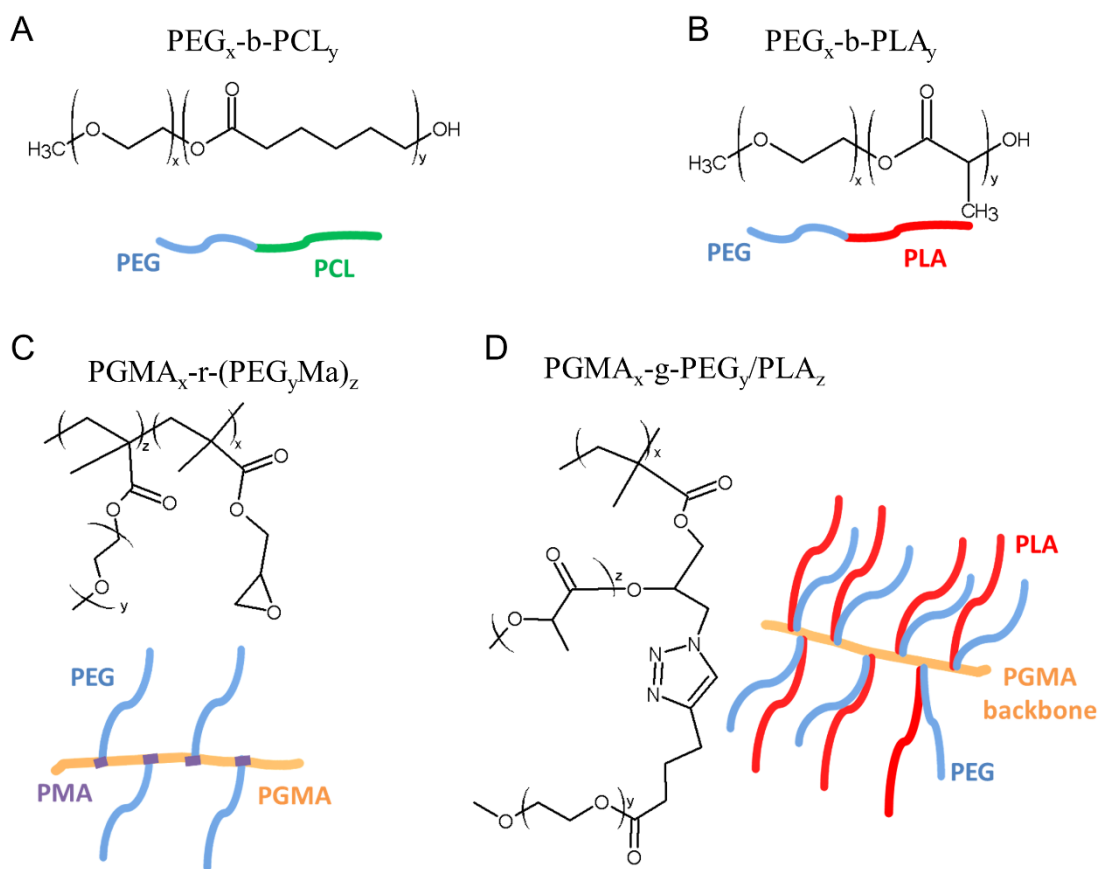


Figure 4-1. Molecular structures of the main types of polymers used in the study and their schematic representations.

Self-assembly of the polymers was achieved by rapid mixing in the MIVM. The fast solvent exchange during the FNP ensured homogenous micro-mixing environment to produce micelles with narrow size distribution.^{27, 134} The size and the size distribution of the polymeric micelles was also investigated by using the DLS. The hydrodynamic and the volume-weighted sizes of the nanoparticles were reported in **Table 4-3** and **Figures 4-2 & 4-3**. The hydrodynamic radius provided an overall micellar size without distinguishing its core or shell radii. On the other hand, the Guinier approximation of the SAXS scattering data provided the information on the radius of gyration of the nanoparticles (**Table 4-3**) which was based on the mass weighted distance from the center of the micelle to its individual mass element.

Table 4-3. Linear and brush polymers and the corresponding nanoparticle information.

Polymer	Starting Polymer Concentration (wt%)	Micelle hydrodynamic radius (DLS) (nm)	Micelle Radius of gyration (SAXS) (nm)
PEG ₁₁₄ -PCL ₃₂	5	6.6	9.3
PEG ₁₁₄ -PCL ₅₃	5	9.8	12.2
PEG ₄₅ -b-PLA ₁₆₉	1	14.5	10.9
PEG ₇₅ -b-PLA ₁₆₇	1	10.6	8.1
PGMA ₆₈ -g-PEG ₁₆ /PLA ₁₇	0.2	7.0	5.7
PGMA ₇₂ -g-PEG ₄₅ /PLA ₃₃	0.27	8.2	6.9
PGMA ₇₂ -g-PEG ₄₅ /PLA ₃₃	2	8.8	7.0
PGMA ₇₂₁ -g-PEG ₄₅ /PLA ₂₉	0.27	15.9	17.8
PGMA ₇₂₁ -g-PEG ₄₅ /PLA ₂₉	2	14.3	18.3
PGMA ₆₄ -r-(PPEG ₂₂ Ma) ₅	0.27	6.2	4.3

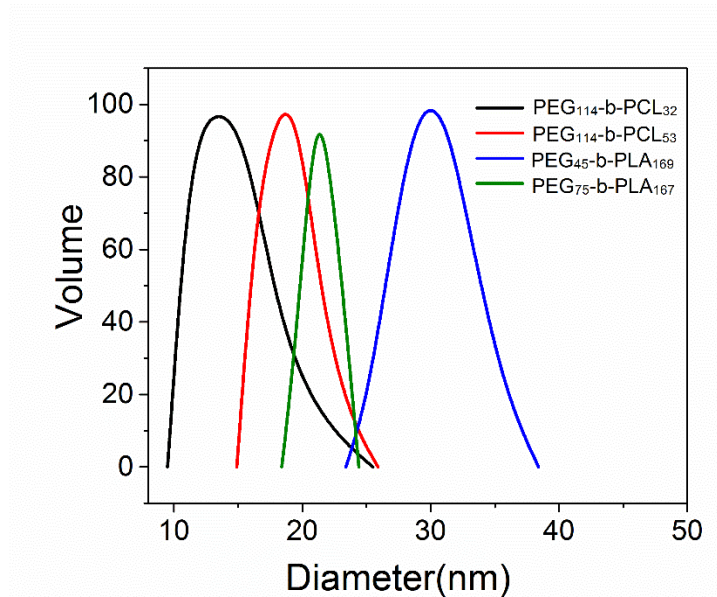


Figure 4-2. Size distribution (measured by the DLS) of polymeric micelles formed from linear diblock copolymers. The diameters were volume weighted.

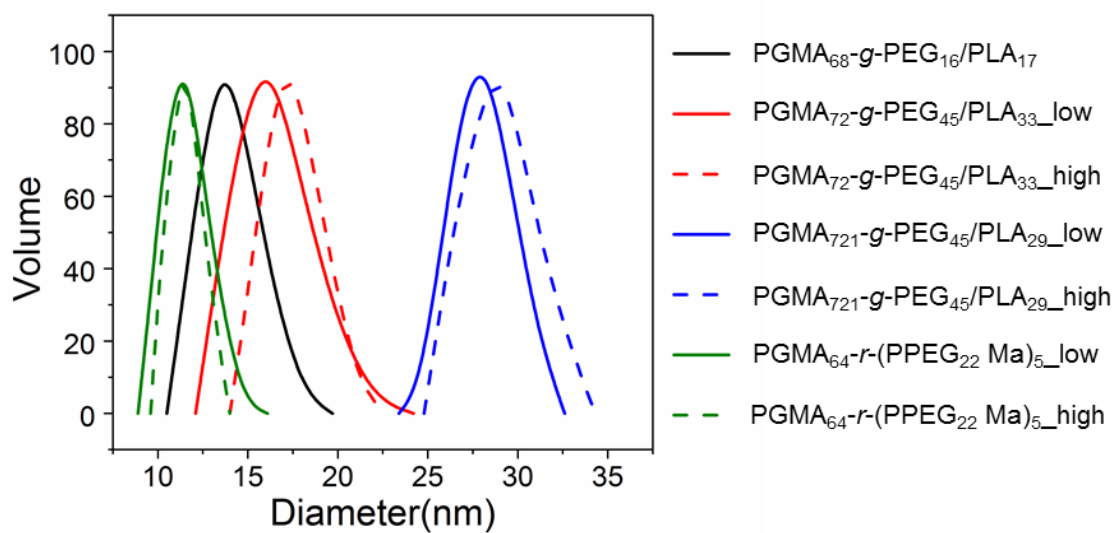


Figure 4-3. Size distribution of polymeric micelles formed from polymeric brushes. The measurements were performed by using the DLS and the diameters were volume weighted.

The core-shell modeling was first applied to the scattering data of the micelles composed of simple diblock copolymers such as PEG-*b*-PCL and PEG-*b*-PLA. The core-shell structures originated from these particular amphiphilic polymers had been previously studied by utilizing SANS or complementary SANS/SAXS techniques in which specifically the core-shell spherical morphology was captured.^{117, 125} Although the spherical morphology might be the majority of the cases, worm-like micelles and vesicles have been also reported.¹³⁵⁻¹³⁷ Here, the core-shell sphere model was found to fit the one-dimensional scattering data well for these micelles (**Figure 4-4A& C and 4-5A&C**). Furthermore, the spherical morphology was also confirmed by the typical bell shape of the pair-distance distribution function – $p(r)$. The $p(r)$ function is known to describe the paired-set of all distances between all points within the nanostructure. The following equation relates the $p(r)$ function of an individual micelle with the scattering intensity,

$$I_{micelle}(q) = \int p(r) \cdot \frac{\sin(q \cdot r)}{q \cdot r} dr$$

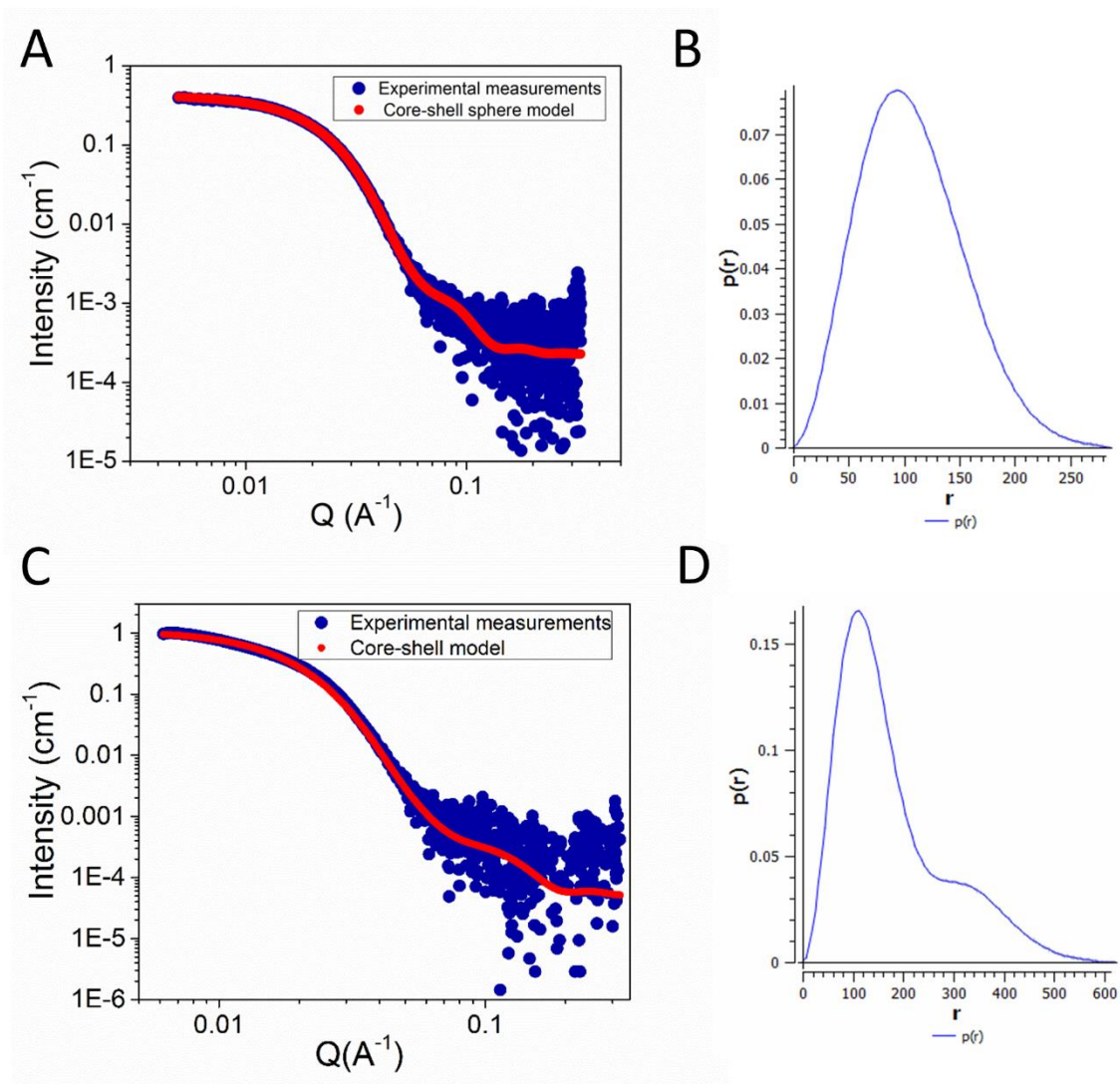


Figure 4-4. (A) SAXS data and model fitting for PEG₁₁₄-*b*-PCL₃₂. (B) The corresponding $p(r)$ distribution function for PEG₁₁₄-*b*-PCL₃₂. (C) SAXS data and model fitting for PEG₁₁₄-*b*-PLA₅₃. (D) The corresponding $p(r)$ distribution function for PEG₁₁₄-*b*-PLA₅₃.

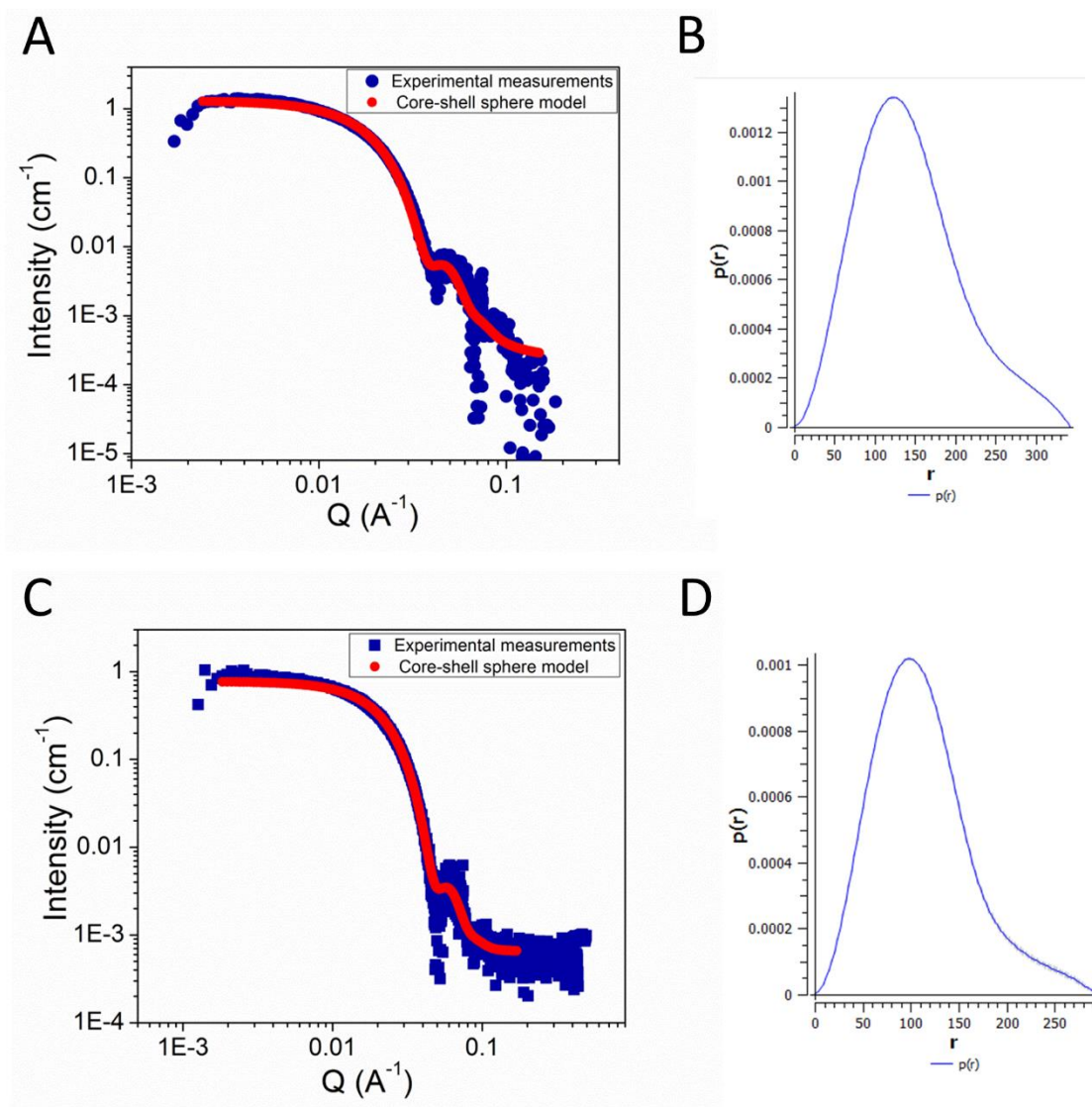


Figure 4-5. (A) SAXS data and model fitting for PEG₄₅-*b*-PLA₁₆₉. (B) The corresponding $p(r)$ distribution function for PEG₄₅-*b*-PLA₁₆₉. (C) SAXS data and model fitting for PEG₇₅-*b*-PLA₁₆₇. (D) The corresponding $p(r)$ distribution function for PEG₇₅-*b*-PLA₁₆₇.

The fitted parameters of these micelles made from linear diblock copolymers could be found in **Table 4-4**. For the PEG-*b*-PCL micelles with the same size of the PEG hydrophilic block, the core radius as well as the aggregation number increased with the increase of the

hydrophobic PCL length. This observation is consistent with the previous studies and predictions by the scaling and mean-field theories.^{125, 138} For PEG-*b*-PLA micelles, increasing the length of the PEG block while keeping the PLA block length the same resulted in the reduction of the nanoparticle core size and aggregation number. Longer PEG chains provided higher energy barrier and arrested the growth of the nanoparticle at a smaller core size.

Table 4-4. Parameters obtained from fitting the SAXS data into the core-shell sphere model.

Polymer	R_{core} (Å)	T_{shell} (Å)	χ^2	Agg#	% PEG _{shell}	SLD	SLD	Diff. (%)
						calc. ρ_{shell} (Å ⁻²)	fitted ρ_{shell} (Å ⁻²)	
PEG ₁₁₄ - <i>b</i> -PCL ₃₂	52.6	48.3	1.10	114.86	22.97	9.69E-06	9.60E-06	0.90
PEG ₁₁₄ - <i>b</i> -PCL ₅₃	69.0	47.1	13.70	156.63	22.35	9.68e-06	9.61e-06	0.77
PEG ₄₅ - <i>b</i> -PLA ₁₆₉	107.4	33.9	2.63	331.2	14.6	9.61E-06	9.67E-06	0.58
PEG ₇₅ - <i>b</i> -PLA ₁₆₇	81.9	22.3	0.46	146.5	17.6	9.64e-06	9.96e-06	3.26

A similar approach was then taken for the micelles made from amphiphilic brush-copolymers. The internal structural information of the particles was extracted by fitting the SAXS data into core-shell models. The core-shell spherical model was first used to fit the SAXS data of PGMA₆₈-*g*-PEG₁₆/PLA₁₇ and PGMA₇₂-*g*-PEG₄₅/PLA₃₃ micelles. The polymers that were used for the micelle formation have equivalent lengths of the backbone polymer but differ in the lengths of the side polymers (PEG/PLA). The 1-D experimental scattering data as well as the best model fits to the data were reported in **Figure 4-6A** and **Figure 4-7A & C**. The spherical morphology was confirmed by the typical bell shape of the distance distribution functions $p(r)$

(Figure 4-6B and 4-7 B & D). The parameters obtained from the modeling were reported in Table 4-5. It was determined that the aggregation numbers of these brush polymers were close to 4 which is significantly lower compared with the linear block copolymers having aggregation numbers at least one order or two of magnitude larger. The concentration of the polymer varied in a small range did not have any influence on the size or other structural parameters of the micelles.

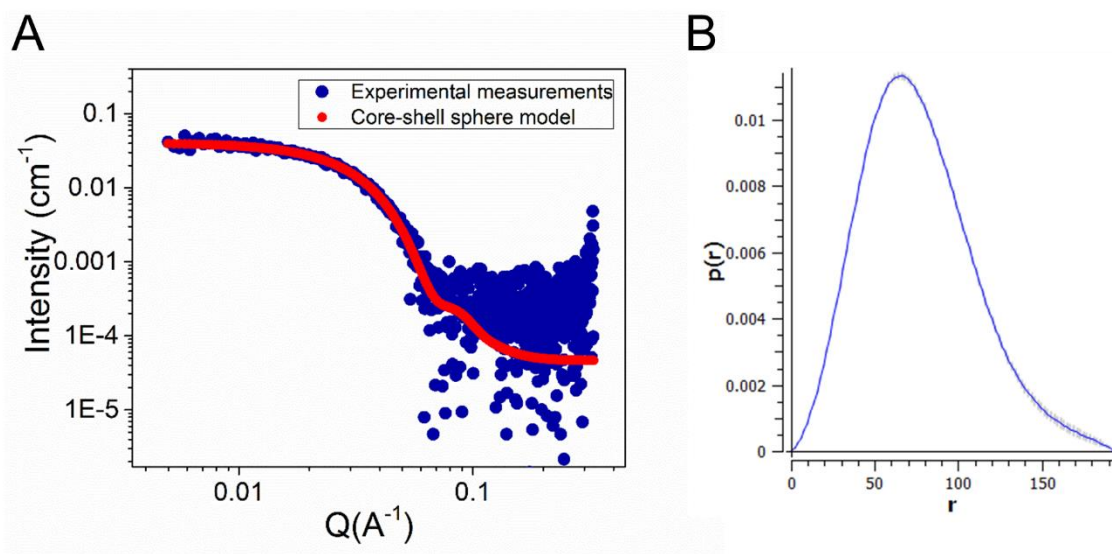


Figure 4-6. (A) SAXS data and model fitting for $\text{PGMA}_{68}\text{-g-PEG}_{16}/\text{PLA}_{17}$ nanoparticles produced at 0.2wt% polymer starting concentration. (B) The corresponding distance distribution function $p(r)$.

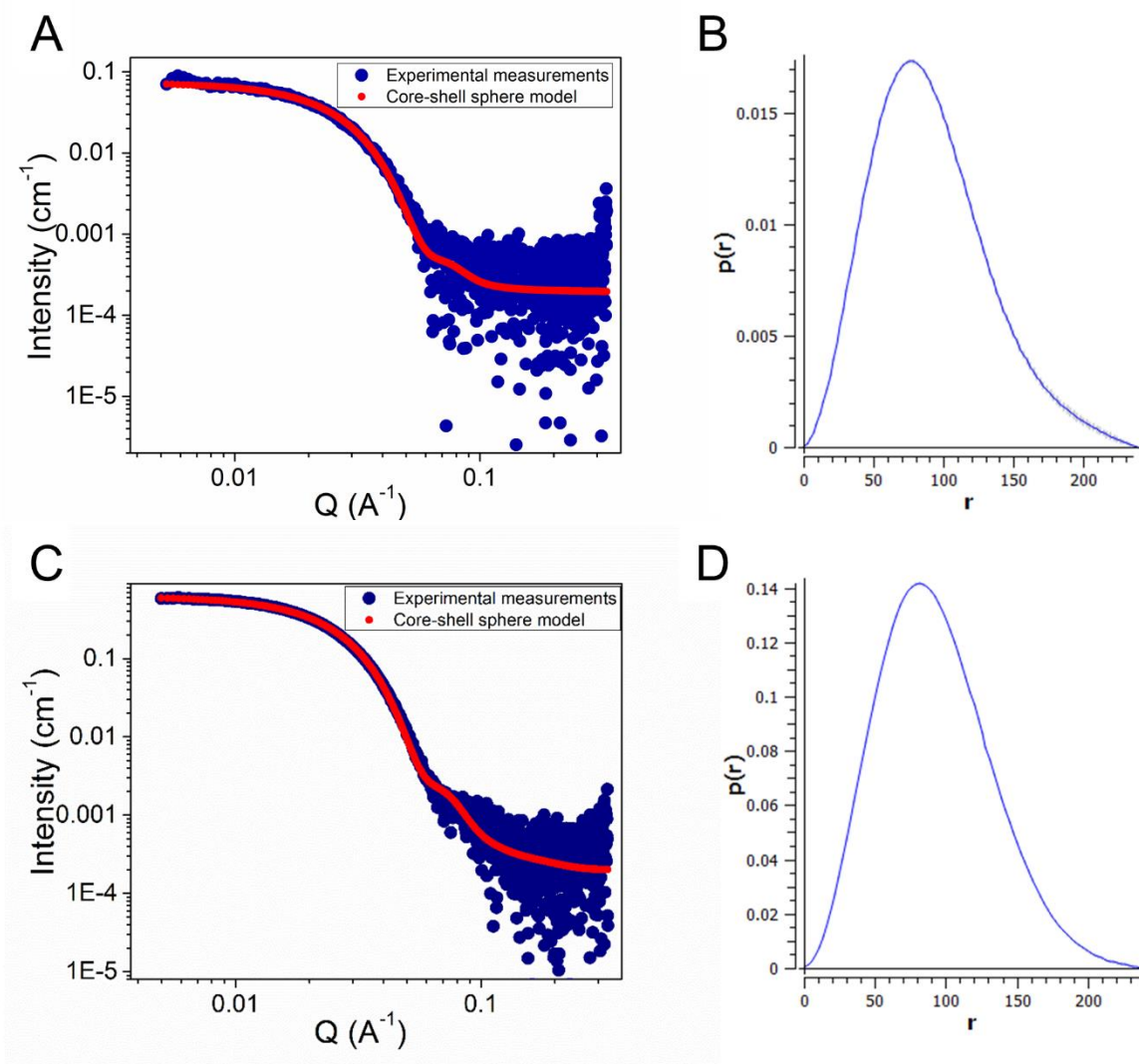


Figure 4-7. (A) SAXS data and model fitting for PGMA₇₂-g-PEG₄₅/PLA₃₃ nanoparticles produced at 0.27 wt% polymer starting concentration. (B) The corresponding $p(r)$ distribution function of (A). (C) SAXS data and model fitting for PGMA₇₂-g-PEG₄₅/PLA₃₃ nanoparticles produced at 2 wt% polymer starting concentration. (D) The corresponding $p(r)$ distribution function of (C).

The scattering data for micelles composed from the PGMA₇₂₁-g-PEG₄₅/PLA₂₉ polymers was well fitted into core-shell cylindrical model as presented in **Figure 4-8A & C**. The

pair distribution functions $p(r)$ with a very asymmetrical shape (**Figure 4-8B & D**) confirmed the presence of the more elongated structures. For an ideal rigid cylinder, the $p(r)$ is characterized by the initial bell shape at low r followed by the inflection point and a very linear decrease to 0 at larger r .¹³⁹ Therefore, the shape of the $p(r)$ (presented in **Figure 4-8B & D**) with the presence of another peak (shoulder) might indicate more flexible (worm-like) nature of the micelles. The obtained parameters from fitting the scattering data of PGMA₇₂₁-*g*-PEG₄₅/PLA₂₉ micelles were reported in **Table 4-5**. The analysis revealed that the aggregation number for this specific polymer in aqueous environment was close to 1 (1.36 for lower particle concentration and 1.55 for higher particle concentration). This interesting observation was an indication of the presence of unimolecular aggregates. The much longer hydrophobic PGMA backbone with densely grafted hydrophobic and hydrophilic components allowed for this intermolecular association.

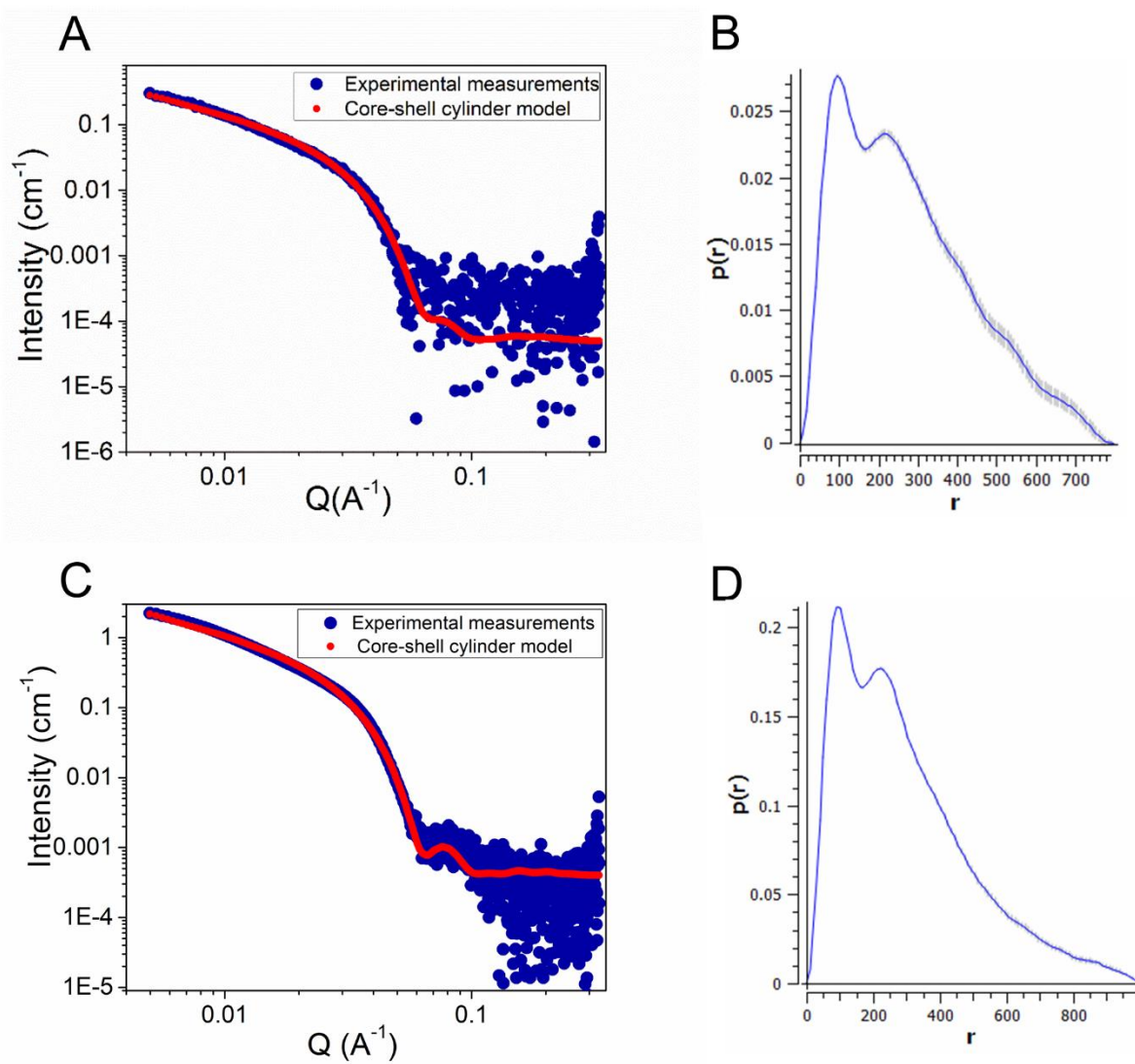


Figure 4-8. (A) SAXS data and model fitting for PGMA₇₂₁-g-PEG₄₅/PLA₂₉ nanoparticles produced at 0.27 wt% polymer starting concentration. (B) The corresponding p(r) distribution function of (A). (C) SAXS data and model fitting for PGMA₇₂₁-g-PEG₄₅/PLA₂₉ nanoparticles produced at 2 wt% polymer starting concentration. (D) The corresponding p(r) distribution function of (C).

Another brush-type polymer investigated here consisted of the repeating units of PGMA and P(PEGMA). The polymeric brushes were extending from the methacrylate groups that were

spaced between the PGMA repeating chains. The SAXS data indicated spherical particles (**Figure 4-9**). The aggregation number was in the range of 21-24, indicating that the brush polymer with less polymer brushes required more polymeric subunits to form the final micellar structure.

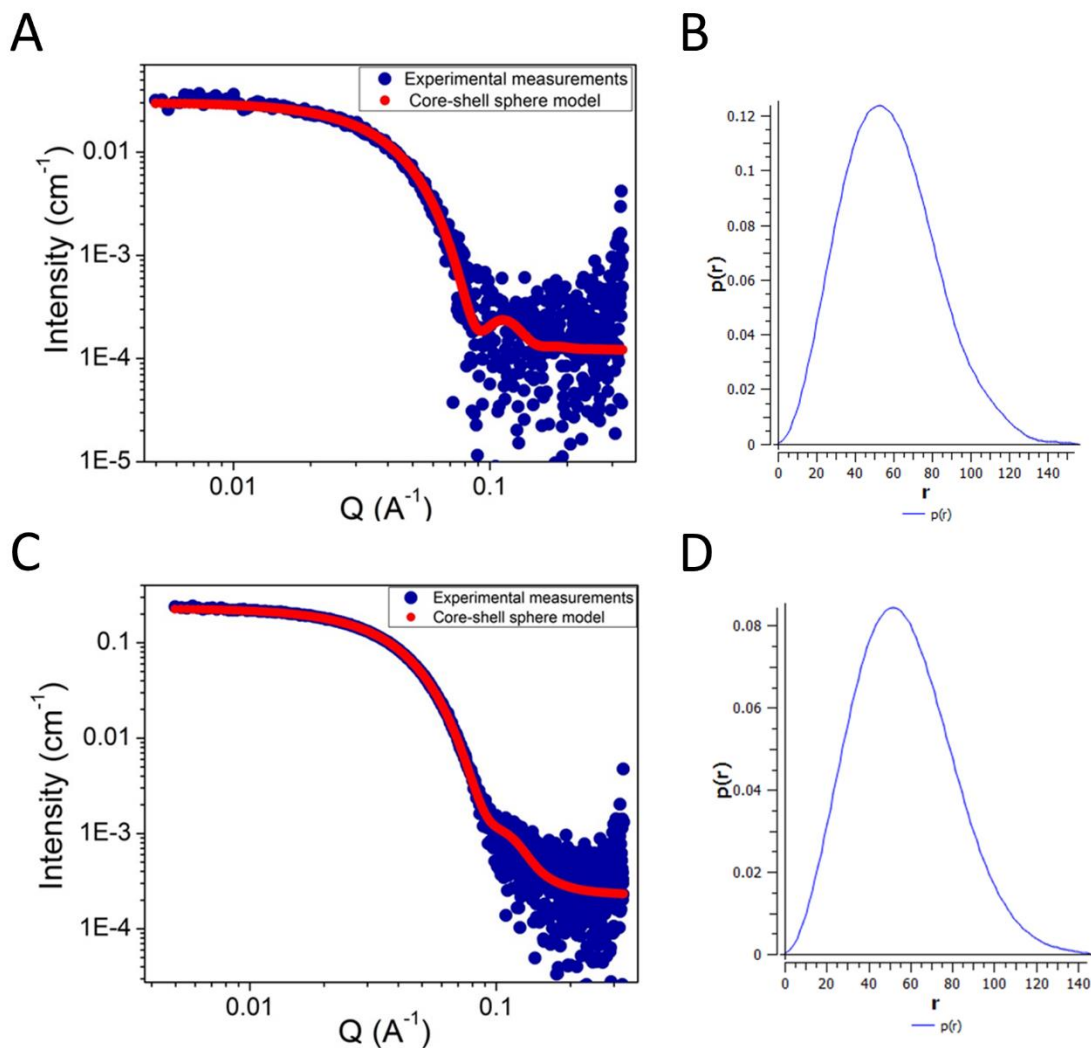


Figure 4-9. (A) SAXS data and model fitting for PGMA_{64-r}-(PPEG₂₂ Ma)₅ nanoparticles produced at 0.27 wt% polymer starting concentration. (B) The corresponding $p(r)$ distribution function of (A). (C) SAXS data and model fitting for PGMA_{64-r}-(PPEG₂₂ Ma)₅ nanoparticles produced at 2 wt% polymer starting concentration. (D) The corresponding $p(r)$ distribution function of (C).

Table 4-5. Parameters obtained from fitting the SAXS data of brush amphiphilics into the core-shell models.

Polymer	R_{core} (Å)	Th_{shell} (Å)	Length (Å)	χ^2	Agg#	% PEG _{shell}	SLD calc. ρ_{shell} (Å ⁻²)	SLD fitted ρ_{shell} (Å ⁻²)	Diff. (%)
PGMA _{68-g} -PEG ₁₆ /PLA ₁₇	55.40	8.07	-	0.93	3.91	33.24	9.80E-06	1.01E-05	2.81
PGMA _{72-g} - PEG ₄₅ /PLA _{33_low}	64.00	26.15	-	1.16	3.46	26.30	9.73E-06	9.64E-06	0.84
PGMA _{72-g} - PEG ₄₅ /PLA _{33_high}	66.68	30.46	-	2.78	3.91	22.57	9.69e-06	9.65e-06	0.34
PGMA _{721-g} - PEG ₄₅ /PLA _{29_low}	42.69	29.67	874.15	2.04	1.36	37.43	9.81e-06	1.03e-05	4.74
PGMA _{721-g} - PEG ₄₅ /PLA _{29_high}	42.53	28.14	1004.1	30.29	1.55	37.49	9.84e-06	1.03e-05	4.99
PGMA _{64-r} -(PPEG ₂₂ Ma) _{5_low}	48.36	13.69	-	1.398	23.96	30.13	9.77E-06	9.78E-06	0.187
PGMA _{64-r} -(PPEG ₂₂ Ma) _{5_high}	46.48	10.72	-	1.704	21.27	38.78	9.86e-06	9.67e-06	1.93

The morphology of some of the particles was also investigated by the TEM imaging technique (**Figure 4-10**). The spheres were observed for PGMA_{68-g}-PEG₁₆/PLA₁₇ and PGMA_{72-g}-PEG₄₅/PLA₃₃ micelles, consistent with the results revealed by SAXS. However, the spherical morphology that TEM captured for PGMA_{721-g}-PEG₄₅/PLA₂₉ nanoparticles contradicted with the

SAXS observations. The discrepancy might come from sample preparation for TEM images. The drying and/or staining processes that are required for TEM sample preparation, and/or particle-substrate interaction on the TEM grid, might fold the rod-like micelles into spheres.

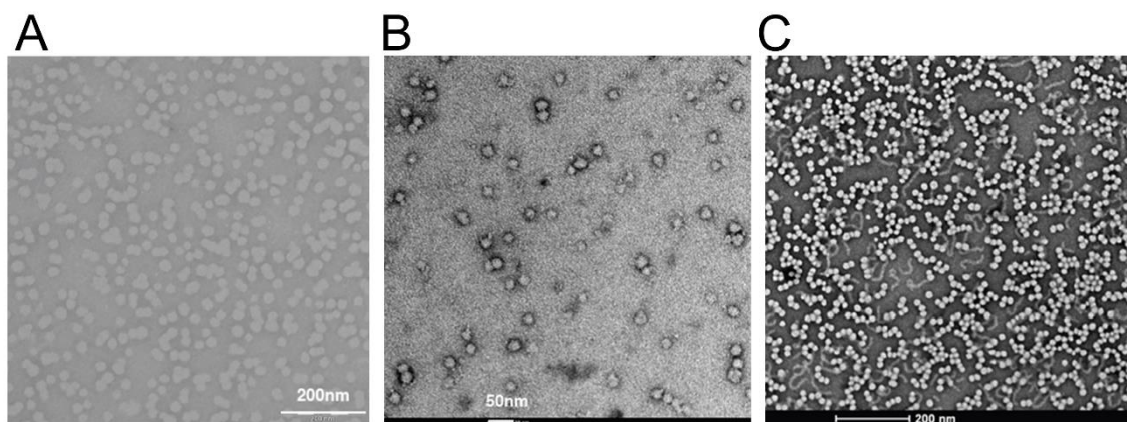


Figure 4-10. Typical TEM images of (A) $\text{PGMA}_{68}\text{-}g\text{-PEG}_{16}/\text{PLA}_{17}$, (B) $\text{PGMA}_{72}\text{-}g\text{-PEG}_{45}/\text{PLA}_{33}$, and (C) $\text{PGMA}_{721}\text{-}g\text{-PEG}_{45}/\text{PLA}_{29}$ micelles.

The overall micellar sizes (core radius plus shell thickness) obtained from SAXS were compared with the DLS data (**Figure 4-11**). A good agreement was found between these two techniques.

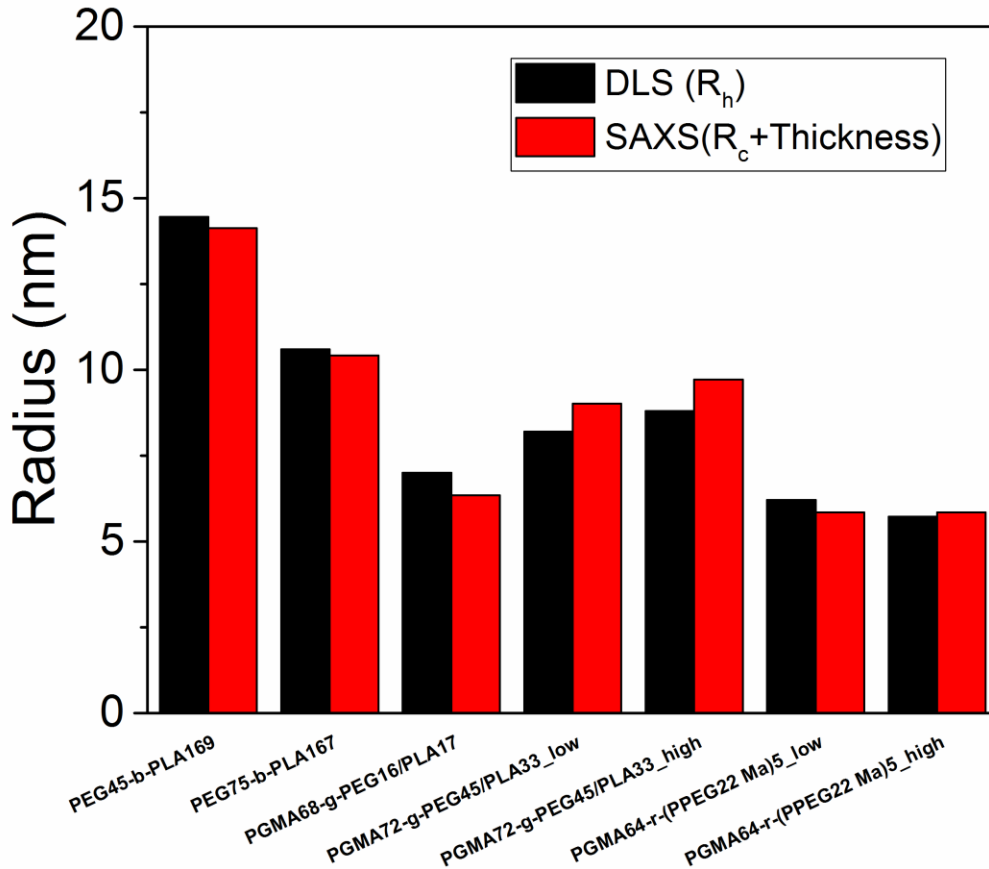


Figure 4-11. Comparison of the micelle sizes measured by the SAXS and by the DLS.

4.5 Conclusions

In this chapter, we investigated the internal structures of polymeric micelles composed of simple linear diblock copolymers and brush amphiphilics with complex molecular building blocks. The fitting parameters obtained from modeling the SAXS data revealed the essential internal structural parameters such as the radius and length (in case of rod-like structures) of the core as well as the shell thickness of the studied micelles. This information was further used to calculate the aggregation numbers of the micelles and the percent PEG content in the shell. The analysis revealed that for the simple diblock copolymer micelles the aggregation number was

relatively large (>100). Whereas, for the densely grafted polymers, the intermolecular association of the PLA on the PGMA backbone was favored, resulting in near unit aggregation numbers.

5 SURFACE CONJUGATION OF NANOPARTICLES WITH POLYPHOSPHATE

Reprinted with permission from Magdalena Szymusiak, Alexander J. Donovan, Stephanie A. Smith, Ross Ransom, Hao Shen, Joseph Kalkowski, James H. Morrissey and Ying Liu, Colloidal Confinement of Polyphosphate on Gold Nanoparticles Robustly Activates the Contact Pathway of Blood Coagulation, *Bioconjugate Chemistry*, 27 (1), 102–109, 2016. Copyright (2016) American Chemical Society.

5.1 Introduction

Polyphosphate (polyP) is an inorganic linear macromolecule consisting of orthophosphates connected by phosphoanhydride bonds.¹⁴⁰ The prevailing thought in the biochemistry community for decades contended that polyP was an early evolutionary casualty in nature's endeavor to design information-dense, multifunctional biomacromolecules.¹⁴¹ Arthur Kornberg and others¹⁴² in the last two decades have reasserted polyP's significant role in a multitude of organismal processes blurring across taxonomic boundaries: the polymer possesses potent hemostatic, inflammatory, and thrombotic properties,¹⁴³⁻¹⁴⁶ hinders tumor growth and angiogenesis,¹⁴⁷ modulates bacterial pathogenicity,¹⁴⁸ chelates toxic metals,¹⁴⁹ aids in DNA transport,¹⁵⁰ and directs histological differentiation,^{151, 152} among innumerable other functions. PolyP arguably performs its variegated cellular duties, even with its simple polyphosphoanhydride chemistry, by adopting different macrostructures depending on polymer length, local environment and incoming stimuli similar (but perhaps on a much more rudimentary level) to the plethora of possible tertiary structures encountered with polypeptides. Some prokaryotes surface-pattern long-chain polyPs at varying surface densities on their exterior, with the polymer projecting outward from the cell membrane into their surroundings. For example, the human infectious agents *N. meningitidis* and *N. gonorrhoeae*, responsible for bacterial meningitis and gonorrhea, respectively, derive their resilience and virulence in large

part from storing a significant fraction of their inorganic phosphate as high-molecular weight polyP on their capsules.¹⁵³ The intensely anionic charge density on the exterior is hypothesized to confer protection from a myriad of environmental insults. DoCampo and coworkers discovered condensed polyP on the nanometer-scale in several protozoan species known to infect insects, notably *T. cruzi* and *T. brucei*, in spherical, mildly acidic organelles called acidocalcisomes,¹⁵⁴ colocalized with concentrations of metal ions at levels orders of magnitude higher than in the cytosol. More recently, short-chain polyP has been found in nearly identical subcellular compartments called dense granules in human platelets.¹⁵⁵ We recently established that polyP spontaneously self-assembles into granular nanoparticles in aqueous media containing concentrations of divalent metal cations such as Ca^{2+} and Mg^{2+} , at levels normally found in human blood plasma.¹⁵⁶ The nanoprecipitation is a thermodynamic process governed by the polyP polymer size and the metal ion concentration, with the salt concentration controlling the nanoparticle diameter regardless of polymer supersaturation ratio.¹⁵⁶

Considerable effort in recent years has centered on implementing novel conjugation chemistries for modifying polyP with various moieties, e.g. fluorescent dyes, biotin, chromogenic substrates, or primary amines, and attaching the polymer to solid substrates for facilitating *in vitro* and *in vivo* detection, quantitating interactions with various binding partners like thrombin, Factor XIIa (FXIIa), Factor XIa (FXIa), and kallikrein, and preventing or slowing enzymatic degradation.^{157, 158} Phosphoramidation of the terminal phosphates does not abrogate polyP's physiological functionality, and polyP attached to solid supports retains robust procoagulant ability.¹⁵⁷

The fact that polyP can exist in a variety of physical manifestations, be it molecularly dissolved, surface-immobilized, granular, or even supported on a colloidal particle scaffold,

suggests that these forms might manifest differential procoagulant properties. The varied ability of inorganic polyP to initiate the contact pathway of blood coagulation could be interpreted to substantiate this hypothesis. It has been previously demonstrated that polyP exerts differential clotting effects as a function of polymer length,¹⁴⁵ with high molecular-weight polymers serving as powerful activators of the contact pathway, while intermediate and platelet-sized polyP are less potent contact activators. These shorter polymers are procoagulant through mechanisms impacting enzymes and inhibitors of other portions of the coagulation cascade.^{143, 146} It has been shown that negatively charged surfaces are necessary to initiate the contact pathway of blood coagulation.¹⁵⁹ Foreign colloidal particles like ellagic acid¹⁶⁰ and silicate minerals¹⁶¹ and highly anionic polymers of sufficient molecular weight like sulfated polysaccharides¹⁶² present the FXII zymogen and its enzymatic binding partners (i.e. high molecular weight kininogen (HMWK) and prekallikrein) a sufficiently large nanosurface to trigger clotting. Sulfated polysaccharides such as heparin are generally considered powerful anticoagulants because of binding to antithrombin; however, in the absence of this enzyme inhibitor, we have previously demonstrated that heparin in actuality is a robust procoagulant molecule in many respects similar to polyP.¹⁶³ FXII has a molecular weight of 80,000 Da,¹⁶⁴ so its radius of gyration would be ~2-5 nm. As such, long-chain polyP should possess significant ability to activate the contact pathway due its high molecular weight and large surface area, with both the molecularly dissolved and nanoprecipitated forms arguably being large enough to activate FXII. On the other hand, the ability of molecularly dissolved, short-chain polyP to initiate the contact pathway is a matter of some dispute.¹⁶⁵⁻¹⁶⁷ Recent work by Mutch and colleagues provides evidence that platelet-sized polyP autoactivates FXII *in vitro*, with activity catalyzed by the presence of zinc cations.¹⁶⁸

In the present investigation we demonstrate that polyP of approximately the size released from platelets conjugated to colloidal gold nanoparticles (GNPs) via phosphoramidate linkages is able to robustly activate the contact pathway of coagulation, with potency equivalent to that of molecularly dissolved, long-chain polyP like that predominately found in bacteria. With further functionalization, polyP-GNP conjugates may be potentially used for targeted delivery as procoagulant agents to the bleeding site, especially benefiting the first-aid treatment of internal hemorrhage. As polyP is already secreted upon platelet activation and naturally exists in the human body, it is anticipated that the introduction of a colloiddally-anchored polyP drug delivery vehicle would have minimal side effects compared to other foreign procoagulants. In order to achieve hemostasis, polyP concentrations typically approach the micromolar range in near vascular injury sites and could potentially be much higher within a platelet-dense thrombus.¹⁴⁵ PolyP-GNPs could potentially be of use in the management of bleeding episodes and provide further corroboration that polyP is able to wield its divergent effects by manifesting in a myriad of macrostructural forms.

5.2 Experimental Procedures

5.2.1 Materials and Reagents

Cystamine, EDAC (*N*-(3-Dimethylaminopropyl)-*N'*-ethylcarbodiimide hydrochloride), MES (2-(*N*-Morpholino)ethanesulfonic acid), 4-Morpholineethanesulfonic acid), NaCl, MOPS (3-(*N*-Morpholino)propanesulfonic acid, 4-Morpholinepropanesulfonic acid), imidazole, phosphorus standard solution, ammonium molybdate IV tetrahydrate, malachite green carbinol base, and poly(ethylene) glycol methyl ether thiol (Mn: 1000) were purchased from Sigma Aldrich (St. Louis, Mo, U.S.A.). Colloidal gold citrate nanoparticles (10 and 50 nm-diameter) were purchased from Ted Pella (Redding, CA). PolyP₇₀ ('Natrium polyphosphat,' range 20-125

orthophosphates) was a kind gift from BK Giulini GmbH (Ludwigshafen am Rhein, Germany). PolyP₈₀₀ (range 200-1600) was prepared as previously described.¹⁴⁵

5.2.2 Synthesis of PolyP₇₀-Cystamine Ligand

PolyP₇₀-cystamine ligand was conjugated via EDAC mediated reaction.¹⁵⁷ PolyP₇₀ (70 mM monophosphate) was added to cystamine (0.1 mM) in the presence of EDAC (300 mM) and MES or MOPS (300 mM) buffers at various pH values (ranging from 6-10) and allowed to mix for 72 h at room temperature (20°C). Control reactions containing all reagents except EDAC were also performed. The efficiency and stability of the reaction at different pH values (ranging from 6-10) were tested by the fluorescamine assay. Briefly, 10 µl of the reaction sample was added to 95 µl of 250 mM borate pH 10, and 45 µl of fluorescamine reagent in acetone (1 mg/ml) in a 96-well black plate. The fluorescamine reagent is known to rapidly bind to the unreacted primary amine group in cystamine, which was measured by using a fluorescence plate reader with excitation wavelength of 365 nm and emission wavelength of 470 nm. A calibration curve was prepared with known concentrations of free cystamine to quantify the amounts of unreacted cystamine in the reaction.

5.2.3 Conjugation of PolyP₇₀-Cystamine to GNPs

PolyP₇₀-cystamine ligand was allowed to react with GNPs in eight 4 ml reaction vials for 10nm GNPs and eight 2 ml reaction vials for 50nm GNPs. Depending on the nanoparticle size (supplied in different starting particle concentrations or pre-concentrated), the following reagent volumes and concentrations were chosen as indicated in **Table 5-1** below.

Table 5-1. Experimental conditions for conjugation of polyP₇₀-cystamine to GNPs.

GNP size (nm)	GNP starting concentration (nM)	GNP suspension Volume (μ l)	Ligand solution (0.1 mM) Volume (μ l)	MOPS buffer (pH 8) (μ l)
10	9.43	3850	30	120
50	0.374	1970	15	15

Control reactions of PEG-thiol (0.2 mM) with GNPs were also set up. The same reaction volumes were chosen for consistency. The ligands (polyP₇₀-cystamine or PEG-thiol) were used in a 2:1 excess ratio to GNP available binding sites. The reaction vials were first kept for 24 h at room temperature with constant slow mixing on a rotator. To increase binding efficiency, the salt addition was initiated to increase the ionic strength of the solution. 10 μ l of 5 M NaCl was added to the reaction vials while mixing. The procedure of salt addition was repeated eight times (two times a day with at least a 6 h break in between). The final concentration of salt was 0.1 M NaCl.

5.2.4 Removal of Unreacted PolyP70

Unreacted polyP₇₀ and ligands were removed by using centrifugation in a Labnet Spectrafuge 16M Microcentrifuge (Labnet International, Woodbridge, NJ). The samples from the polyP₇₀-cystamine ligand reactions with GNPs were distributed into 1.6 mL microcentrifuge tubes and centrifuged using optimized conditions (**Table 5-2**). After each centrifugation, the supernatant was collected and the GNP pellet was resuspended with the buffer (Imidazole, pH 7.2) by vortexing for 30 s. After final centrifugation for all GNP types, the pellets were

resuspended with a smaller amount of buffer in order to achieve desired concentrations of polyP₇₀ and GNP.

Table 5-2. Size-dependent centrifugation conditions.

GNP size (nm)	RPM	G-force	Pelleting time (min)	Centrifuge repeat
10	10000	8176	60	3x
50	8000	5223	10	3x

5.2.5 Determination of Number of PolyP₇₀ Chains per Particle

The number of polyP₇₀ chains per particle was calculated by quantifying the concentrations of polyP₇₀ and GNPs in the concentrated samples after completion of the purification step. To quantify the amount of polyP₇₀ present in the sample, 101 µl of sample was mixed with 9.1 µl of 12.1 M HCl and heated at 100 °C for 30 min to first hydrolyze the polyP₇₀ chains into monophosphate (monoP). Then 50 µl of hydrolyzed sample was mixed with 100 µl of malachite green reagent (mixing 0.1% malachite green and 42 mg/ml ammonium molybdate acid solution (5 M HCl) at 3:1 volume ratio) in a 96-well clear plate and allowed to react for 5 min. The amount of monoP present was quantified by measuring the absorbance at 620 nm using a plate reader and comparing the readings with the standardized curve. The amount of GNPs was determined by measuring the absorbance at 405 nm (for 10nm GNPs) and 492 nm wavelengths (for 50nm GNPs) and comparing it with the standard calibration. The final number of polyP₇₀ chains per particle was determined by the following formula:

$$\text{Number of polyP}_{70} \text{ chains per particle} = \frac{\text{monoP concentration} / \text{repeating unit}}{\text{gold nanoparticle concentration}}$$

5.2.6 Transmission Electron Microscopy (TEM)

PolyP₇₀-GNPs or unmodified Au citrate suspension (10 µl) was micropipetted onto a 300-mesh Formvar grid (Structure Probe Inc., West Chester, PA). After 10 min the liquid which had not evaporated was wicked away with the tip of a Kim Wipe®. The samples were examined in a JEM-3010 transmission electron microscope (JEOL Inc., Tokyo, Japan).

5.2.7 Zeta (ζ) Potential Measurements

Zeta potentials of the synthesized polyP₇₀-GNPs and PEG-GNPs were measured by using a Zetasizer Nano ZS instrument (Malvern Instruments, Worcestershire, U.K.) in DI water at 20 °C.

5.2.8 Clotting Assays

Contact pathway activity of polyP₇₀-GNPs was determined by coagulometric assay.¹⁴⁵ Clotting times of citrated human pooled normal plasma (PNP) (George King Biomedical, Overland Park, KS) were quantified at 37°C using a Start 4 coagulometer (Diagnostica Stago, France). Prewarmed polyP or polyP₇₀-GNPs in imidazole buffer was incubated in coagulometer cuvettes with prewarmed plasma for 3 minutes, after which clotting was initiated by addition of phospholipid and CaCl₂. Tests of the contact pathway of blood clotting were conducted using final concentrations of GNPs as indicated, 33% plasma, 25 µM phospholipid, 1.67 mM imidazole pH 7.0, and 8.33 mM CaCl₂.

5.2.9 A_{405} Turbidity Measurements

Turbidity measurements of the same GNPs used above in the coagulometric assays were performed in clear, medium-binding 96-well microplates. A_{405} was typically measured every min for 40-60 min at room temperature (20 °C). Each well contained 50 μ l of citrated human pooled normal plasma (George King Biomedical, Overland Park, KS) pre-warmed to 37°C containing 75 μ M phospholipid; 50 μ l of GNPs or polyP₇₀ (BKGP70) in solution in 5 mM imidazole, pH 7.2; and 50 μ l of 25 mM CaCl₂. GNPs and polyP₇₀ were pre-incubated in the citrated plasma on the microplate at 37°C for 3 min before recalcification to ensure FXII activation.

5.3 Results and Discussion

Binding of polyP₇₀ to GNPs was achieved by two-stage reaction: (1) PolyP₇₀ was first allowed to react with cystamine; (2) The polyP₇₀-cystamine conjugate was then reacted with GNPs by replacing the citrate groups (**Figure 5-1**).

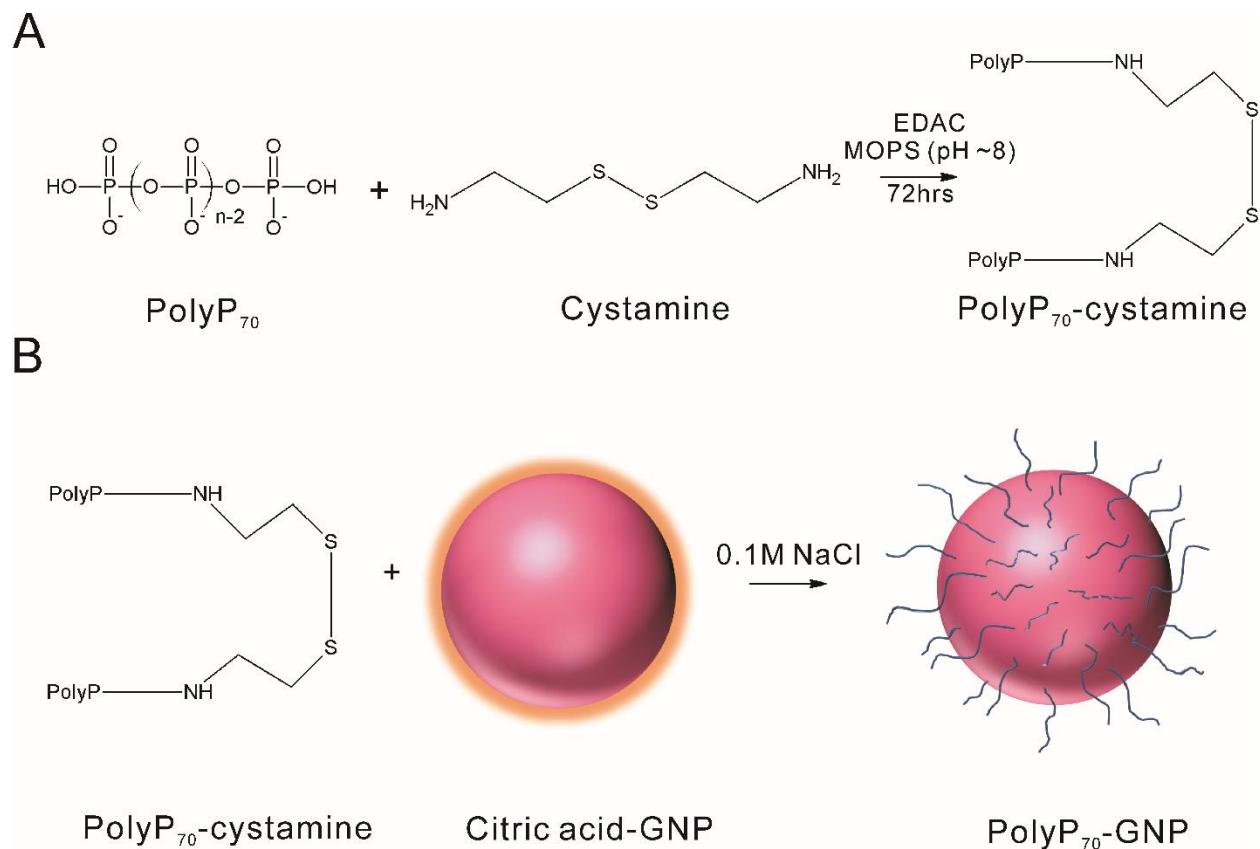


Figure 5-1. The process of synthesizing GNPs conjugated with polyP₇₀. (A) PolyP₇₀ is conjugated to cystamine. (B) PolyP₇₀-cystamine is attached to the surface of GNPs.

The primary amine-containing compounds like polyethylenimine, amine-PEG₂-biotin, and spermidine were used previously to study the covalent attachment of primary amine groups with the terminal phosphates of polyP via EDAC-mediated reaction.¹⁵⁷ We modified this method for the coupling of polyP₇₀ with cystamine – a disulfide molecule, containing two primary amine groups. Reduction of the disulfide moiety in cystamine then allowed for the attachment to the GNP surface. Reaction conditions (including temperature, reaction time, pH, and buffering environment) were optimized to control the coupling of polyP₇₀ with cystamine. For the optimal conditions, polyP₇₀ was allowed to react with cystamine at room temperature and pH around 8

for 48 to 72 h. Higher temperature (37 °C) did not improve the yield. A fluorescamine assay was used to test the amount of the unreacted primary amines on cystamine, which indicated the conjugation efficiency. The highest yield of the reaction was approximately 90% as seen in **Table 5-3**.

Table 5-3. Conjugation efficiency of polyP₇₀ and cystamine at various pH conditions.

Buffer	pH of reaction	Efficiency (24 h)	Efficiency (48 h)	Efficiency (72 h)
MOPS (100 mM)	7.1	61.5%	65.0%	71.1%
MOPS (100 mM)	7.6	72.7%	74.3%	78.7%
MOPS (100 mM)	8.1	79.6%	87.3%	88.1%
MOPS (100 mM)	8.5	83.5%	87.3%	88.6%
MES (100 mM)	7.8	81.4%	89.5%	-

An investigation of P-N bond hydrolysis was carried out to test the stability of the polyP₇₀-cystamine ligand. After 72 h of reaction, a fluorescamine assay was performed to detect the concentration of the unreacted cystamine. The samples were monitored for two weeks and hydrolysis of the P-N bonds was quantified. The P-N bond hydrolyzed in acidic conditions at pH 6.02. It was stable at pH above 7 as presented in **Table 5-4** below. These results were in good agreement with other literature data on P-N bond hydrolysis.¹⁶⁹⁻¹⁷³

Table 5-4. Free cystamine concentration (μM) before and after pH adjustment.

pH	Primary amine concentration (μM)				
	Before pH adjustment	After 1 day	After 5 days	After 8 days	After 13 days

6.02	16.4 ± 0.49	30.0 ± 0.68	26.4 ± 0.82	27.6 ± 0.17	37.18 ± 1.41
7.07	16.4 ± 0.49	18.6 ± 1.29	14.5 ± 0.31	12.9 ± 0.12	13.72 ± 0.78
9.05	16.4 ± 0.49	17.1 ± 0.85	14.8 ± 0.44	14.2 ± 0.26	15.31 ± 1.36
10.01	16.4 ± 0.49	17.2 ± 0.90	14.8 ± 0.28	12.7 ± 1.2	14.73 ± 0.10

The polyP₇₀-cystamine conjugate was allowed to react with GNPs of two different sizes (10nm and 50nm) by displacing the citrate group. After 24 h of reaction, salt addition was initiated to increase free GNP surface area available for polyP₇₀ attachment.¹⁷⁴ The slow increase in salt concentration in the reaction over a period of four days (0.1 M NaCl final concentration) allowed the already attached polyP₇₀ to extend, creating more space for the unreacted ligands to access the gold surface, thus resulting in an increase in the number of polyP₇₀ chains per particle. The reaction conditions were modified from the conditions used to conjugate DNA on the surface of gold nanoparticles¹⁷⁴ and their detailed description is presented in the Experimental Procedures. The full coverage is estimated from the theoretical calculations based on the ideal maximum ligand density of 0.22 per square nanometer^{175, 176} and found to be 69 and 1727 for 10nm and 50nm GNPs, respectively. The maximized conjugation efficiencies were found to be 24.7% and 46.0% for 10 nm and 50 nm GNPs respectively, comparing the number of conjugated ligands with the theoretical maxima.

Removal of excess, unreacted polyP₇₀ left in the solution was achieved via centrifugation. In order to find the most efficient centrifugation conditions, the pelleting time, t , was calculated using the following equation for Stokes sedimentation:^{177, 178}

$$t = \frac{k}{S}$$

where k is the pelleting efficiency of the rotor and S is the sedimentation coefficient. The pelleting efficiency (k) was calculated as:^{177, 178}

$$k = \frac{2.5 \times 10^{11} \ln\left(\frac{r_{max}}{r_{min}}\right)}{RPM^2}$$

where r_{max} and r_{min} are the maximum and minimum radii of the centrifuge respectively, and RPM is the speed in revolutions per minute. The sedimentation coefficient, S , can be calculated as:¹⁷⁷

$$S = \frac{2(\rho_s - \rho_l) \left(\frac{d}{2}\right)^2}{9\eta}$$

where ρ_s and ρ_l are the densities of GNPs and water, respectively, η is the viscosity of water, and d is the diameter of GNPs.

To further verify the calculated pelleting conditions, a set of control experiments was performed by mixing polyP₇₀ at different concentrations with 10nm GNPs and centrifuging them at different g-forces using the calculated pelleting time. G-force can be determined according to the following formula:

$$g_{force} = 11.18 r \left(\frac{RPM}{1000}\right)^2$$

where r is the radius of the centrifuge in cm and RPM is the speed in revolutions per minute.

Both recovery of the GNPs and removal of the unreacted polyP₇₀ can be maximized at a g-force between 4000 and 10000 (**Figure 5-2**). The optimized centrifugation conditions for nanoparticles of different sizes are described in the **Experimental Procedures section (Table 5-2)**. These control experiments were essential to determine the final optimal conditions for the efficient removal of unreacted polyP₇₀ and recovery of the GNPs without causing any significant aggregation within minimized centrifugation duration time. After each centrifugation, the

supernatant was removed and the pellets were re-suspended with a buffer at pH 7.2 to ensure the stability of the polyP₇₀-cystamine ligand and prevent polyP₇₀ hydrolysis.

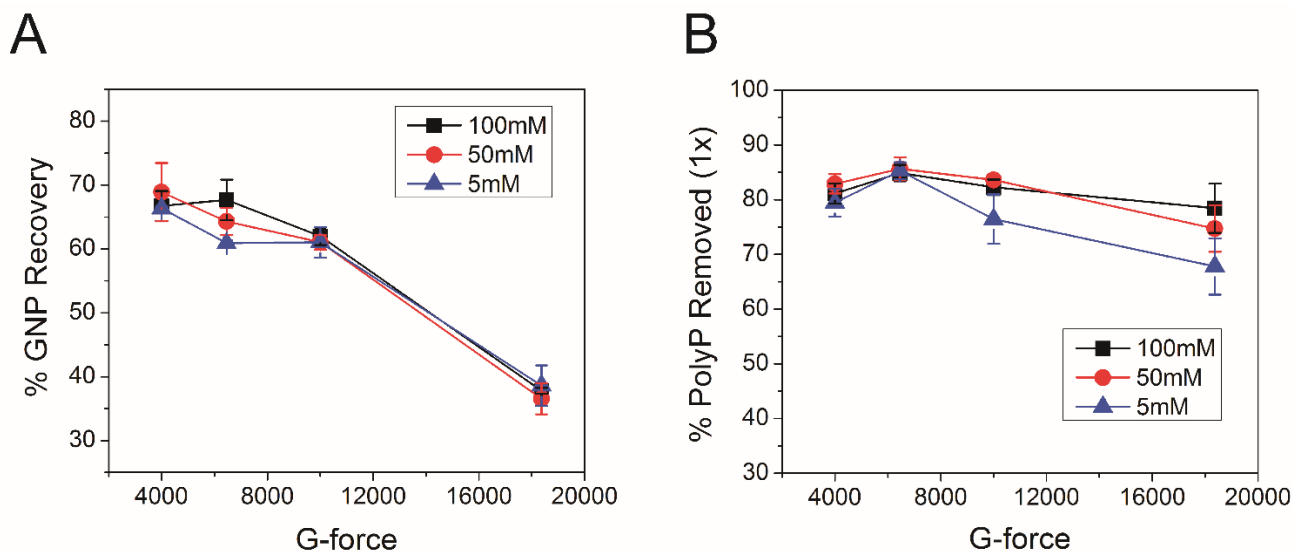


Figure 5-2. Control centrifugation experiments for 10nm GNPs: (A) Percent GNP recovery after one time (1x) centrifugation of a mixture of polyP₇₀ at different concentrations (100 mM, 50 mM, and 5 mM) with 10nm GNPs. (B) Percent polyP₇₀ removed after single centrifugation (1x). The values are reported as the mean \pm S.E. (n=3).

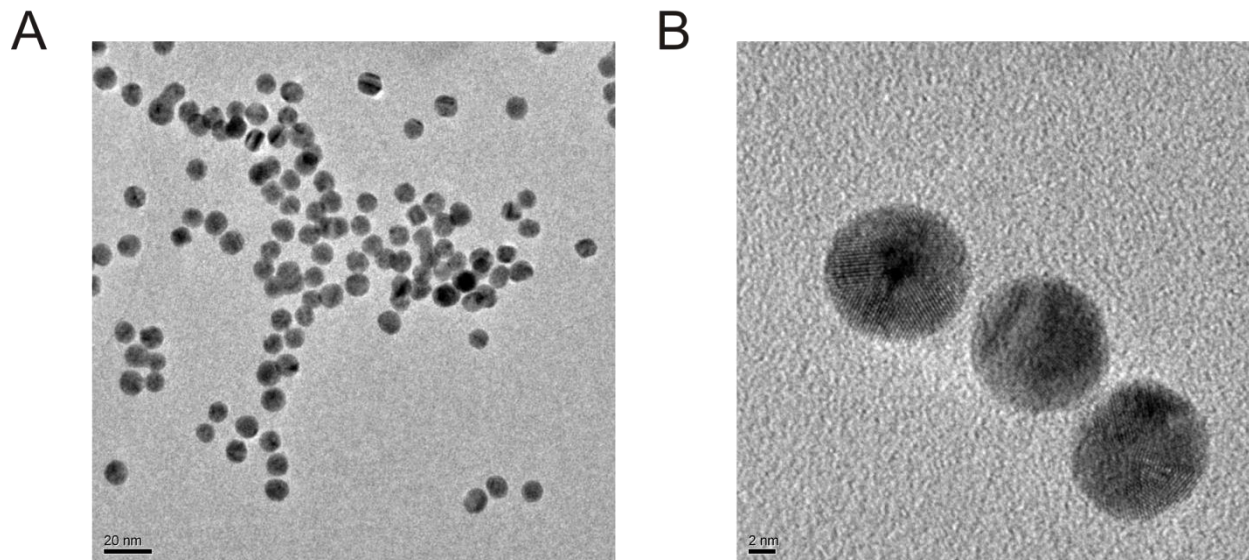


Figure 5-3. Typical transmission electron micrographs of 10nm polyP₇₀-GNPs. (A) polyP₇₀-GNPs are spherical and largely free of aggregation several days after synthesis. Scale bar: 20nm. (B) A trio of polyP₇₀-GNPs with the crystal lattices very apparent. Scale bar: 2nm.

Morphology and stability of the polyP₇₀-GNPs were confirmed by TEM (**Figure 5-3**), revealing that the polyP₇₀-GNP dispersion is largely free of aggregation, and the morphology of the GNPs is indistinguishable from commercially available citrated gold suspensions, that being spherical and uniformly electron dense. High magnification micrographs of 10nm polyP₇₀-GNPs reveal the recognizable atomic lattices of the particles, clearly suggesting that the GNPs are nanocrystals.

After purification using centrifugation, concentrations of polyP₇₀ were measured using the malachite green assay and concentrations of GNPs were obtained by UV-vis spectroscopy. The number of polyP₇₀ on the surface of GNPs was calculated based on the above measurements. The following polyP₇₀-GNPs were synthesized and characterized (**Table 5-5**) to investigate their ability to initiate the contact pathway of blood coagulation in a concentration-dependent manner.

Table 5-5. Synthesized polyP₇₀-GNPs.

Sample	MonoP conc. (μM)	GNP conc. (nM)	Number of polyP₇₀ chains per particle	UV-vis peak for bulk GNP	UV-vis peak after centrifuging
10nm polyP ₇₀ -GNP	90	75.399	17.052	519	521
50nm polyP ₇₀ -GNP	90	1.619	794.195	531	532

PolyP₇₀-GNPs markedly reduce the time of coagulation in human plasma when assayed for contact activity using a mechanical coagulometer, a standard technique to measure clotting of both whole blood and plasma (**Figure 5-4**). Molecularly dissolved polyP₇₀ and polyP₈₀₀ were added as a positive control to citrated pooled normal plasma (PNP) at monoP concentrations ranging from 0-30 μM. Clotting was initiated by adding excess CaCl₂. Concentration for polyP₇₀-GNPs is given in terms of moles of GNPs (not elemental gold). Reduction in clotting time for polyP₇₀-GNPs follows typical kinetics of a surface-modulated reaction mechanism,¹⁷⁹ suggesting that the polyP₇₀-GNPs provide a templating surface for FXII activation. PolyP₇₀-cystamine ligands conjugated to GNPs of 10- and 50nm diameter robustly activate the contact pathway of coagulation much more efficiently as compared to polyP₇₀ in solution.

The clotting activity of both 10nm and 50nm polyP₇₀-GNPs is comparable to that of much longer polyP (polyP₈₀₀) and even greater at monoP concentrations exceeding 20μM. These results raise the question that colloidal confinement of polyP may yield divergent outcomes in complex, nonlinear biological processes such as blood coagulation, where threshold concentrations of activators must be attained before a response is generated. In this instance, chemical conjugation of platelet-sized polyP, itself a mediocre activator of the contact pathway, to an essentially inert colloidal surface, transforms the small polymer into an excellent contact

activator comparable to polyP approximately ten times larger. Initiation of the contact pathway almost always necessitates a nanosurface of sufficient negative charge density and cross-sectional area to recruit the FXII zymogen. Subsequently, its fellow contact pathway components high molecular weight kininogen (HWMK) and prekallikrein must come in close proximity to FXII to accelerate and propagate the procoagulant stimulus. Anchoring highly anionic polyP₇₀ onto 10nm and 50nm GNPs likely generates such an activating surface for the triad of proteins, whereas short-chain polymers that are molecularly dissolved like platelet-sized polyP₇₀ do not have adequate radii of gyration to localize FXII, HMWK, and prekallikrein together into the primary complex and propagate the signal. As prekallikrein and HMWK have been found to have a complexed molecular weight of 285 kDa in plasma, a surface larger than 5 nm would most likely be required to properly anchor these proteins together with FXII.¹⁸⁰ Bacterial polyPs, typically several hundred to thousands of orthophosphate residues, have molecular weights and radii of gyration comparable to large globular proteins, suggesting that these polymers are already above this threshold size for anchoring the primary complex, given that they robustly initiate the contact pathway of clotting in a fashion similar to foreign colloidal procoagulant agents.¹⁴⁵ Long-chain polyP with robust contact-pathway activity can accordingly be used as a ruler for the measurement of hemostatic activity of polyP₇₀-GNPs and molecularly dissolved polyP₇₀ (**Figure 5-4A**).

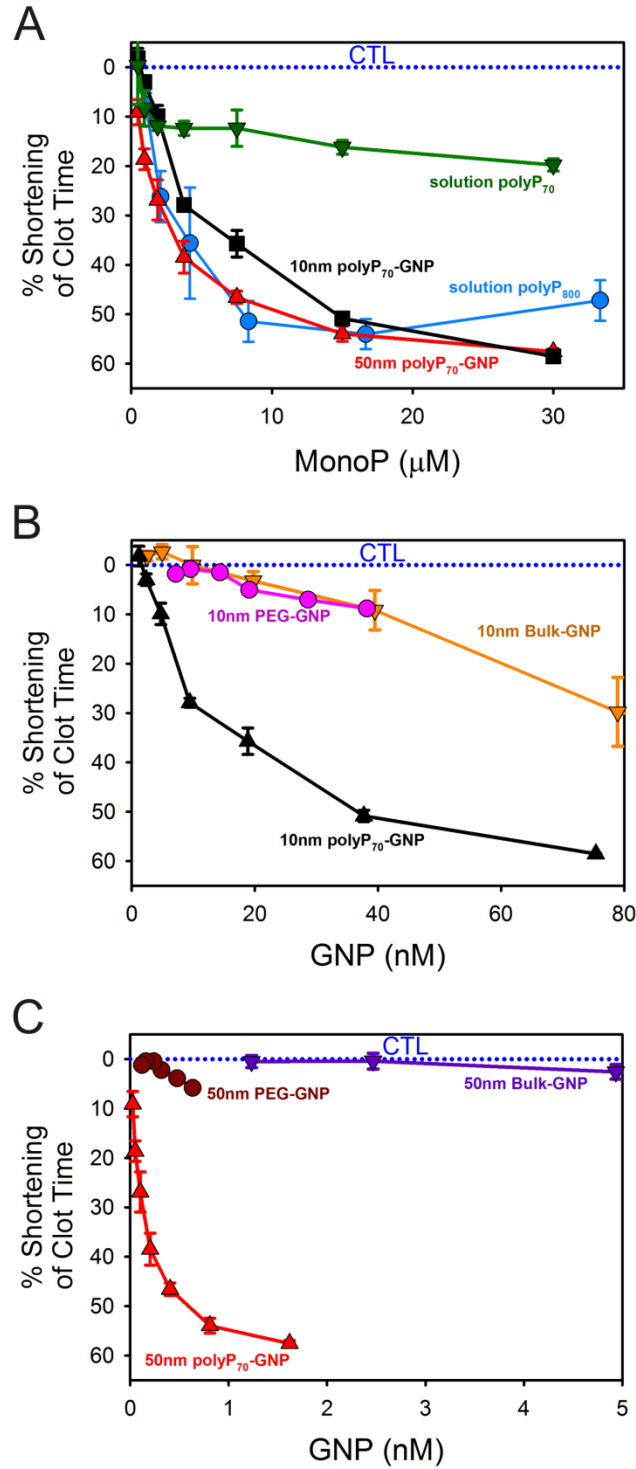


Figure 5-4. Shortening of clotting time of polyP70-GNPs in human plasma when assayed for contact activation as a function of monoP and GNP concentration. (A) Reduction in clotting time of 10nm polyP70-GNPs and 50nm polyP70-GNPs compared to equivalent concentration of

molecularly dissolved polyP70 and heterogeneous long-chain polyP800. (B) Reduction of clotting time of 10nm polyP70-GNPs compared to the equivalent concentration of 10nm bulk-GNPs and 10nm PEG-GNPs. (C) Shortening of clotting time of 50nm polyP₇₀-GNPs compared against the same concentration of 50nm bulk-GNPs and 50nm PEG-GNPs.

The reduction in clotting time elicited by the polyP₇₀-GNPs was further analyzed as a function of the GNP concentration (**Figure 5-4B** and **C**). 50nm polyP₇₀-GNPs are more procoagulant, as contrasted with the 10nm polyP₇₀-GNPs, at equivalent GNP concentration: the 50nm GNPs reduce the time to clot by 60% at less than 2 nM GNP concentration, whereas it takes approximately 80 nM for the equivalent drop with the 10nm GNPs. This effect can be attributed to the twenty-five fold increase in the surface area of the 50nm GNPs when compared with 10nm GNPs, indicating larger localization of polyP₇₀ that could lead to a better recruitment of active clotting factors above their threshold concentration. The curvature of the particles may also affect the structural change of FXII. It is reported by Kushida et al. that nanoparticles of larger size with low curvature effect facilitated higher degree of FXII denaturation, whereas smaller size nanoparticles (high curvature) led to little or no denaturation/unfolding of FXII resulting in much weaker effects on the intrinsic coagulation.¹⁸¹ Citrated (bulk) and PEGylated GNPs are used as controls to demonstrate that the GNPs themselves are not responsible for the marked reduction in clotting time. PEGylation of 10nm citrated GNPs after 3-4 days of reaction reveals that the zeta potential drops from -20 to -5 mV, implying that the negatively charged citrate is being replaced by the neutral PEG-thiol (see **Table 5-6**). The zeta potential of the synthesized polyP-GNPs is found to be -25mV to -30mV, which is comparable to silica particles with the zeta potential range from -25mV to -40mV and kaolin suspensions with the zeta

potentials ranging from -20mV to -30mV.^{182, 183} The silica particles and kaolin have been previously reported to be potent surfaces for contact pathway activation.^{184, 185}

Table 5-6. Zeta (ζ) Potential measurements of the synthesized samples.

Sample	ζ Potential (mV)
10nm bulk	-19.5
10nm polyP ₇₀ -GNPs	-27.5
10nm PEG-GNP	-3.49
50nm bulk	-22.3
50nm polyP ₇₀ -GNP	-26.53
50nm PEG-GNP	-2.30

The contact activity of the polyP₇₀-GNPs was further corroborated by A₄₀₅ turbidity assays in pooled normal plasma (PNP). 10nm and 50nm GNPs have intrinsic absorbance at 405nm; hence, changes in absorbance values must be interpreted cautiously. As the coagulometric assay measures the mechanical and viscous properties of the clotting plasma, the turbidity tests provide complementary information on the optical density of the polymerizing fibrin mesh. Although fibrin clot density is being directly observed, and is a consequence of thrombin kinetics, it is linked to activation of FXII from interaction with a contact surface. Therefore, these two techniques can be used synergistically to evaluate the efficacy of the polyP₇₀-GNPs at initiating the contact pathway of clotting.

Before proceeding with the turbidity tests a series of control experiments were performed to ensure that the absorbance of citrated and polyP₇₀ conjugated GNPs does not change after incubation in PNP, and that the absorbance detector does not reach a saturating value during or after coagulation. **Figure 5-5B, C & D** demonstrate that the GNPs are colloiddally stable in human plasma for at least 1 h, and that A₄₀₅ remains constant. These observations also provide evidence that the GNPs did not aggregate during the clotting assays and that the quantified procoagulant outcomes emerge from the physical parameters we measured in the laboratory. **Figure 5-5A, E & F** show that GNPs at considerably higher concentrations than used in the clotting tests still display a linear relationship with A₄₀₅ turbidity, implying that absorbance values after coagulation will be well below the saturation limit of the detector. Therefore, the absorbance traces can be normalized by subtracting their initial values and directly compared between samples to quantify their procoagulant efficacy. **Figure 5-5A** gives a representative raw absorbance trace of the polyP₇₀-GNPs at 5 μM monoP before normalization. The time to initial fibrin formation is typically determined by fitting a line to the point at which the absorbance begins to increase and subsequently finding the intersection with the baseline absorbance value.

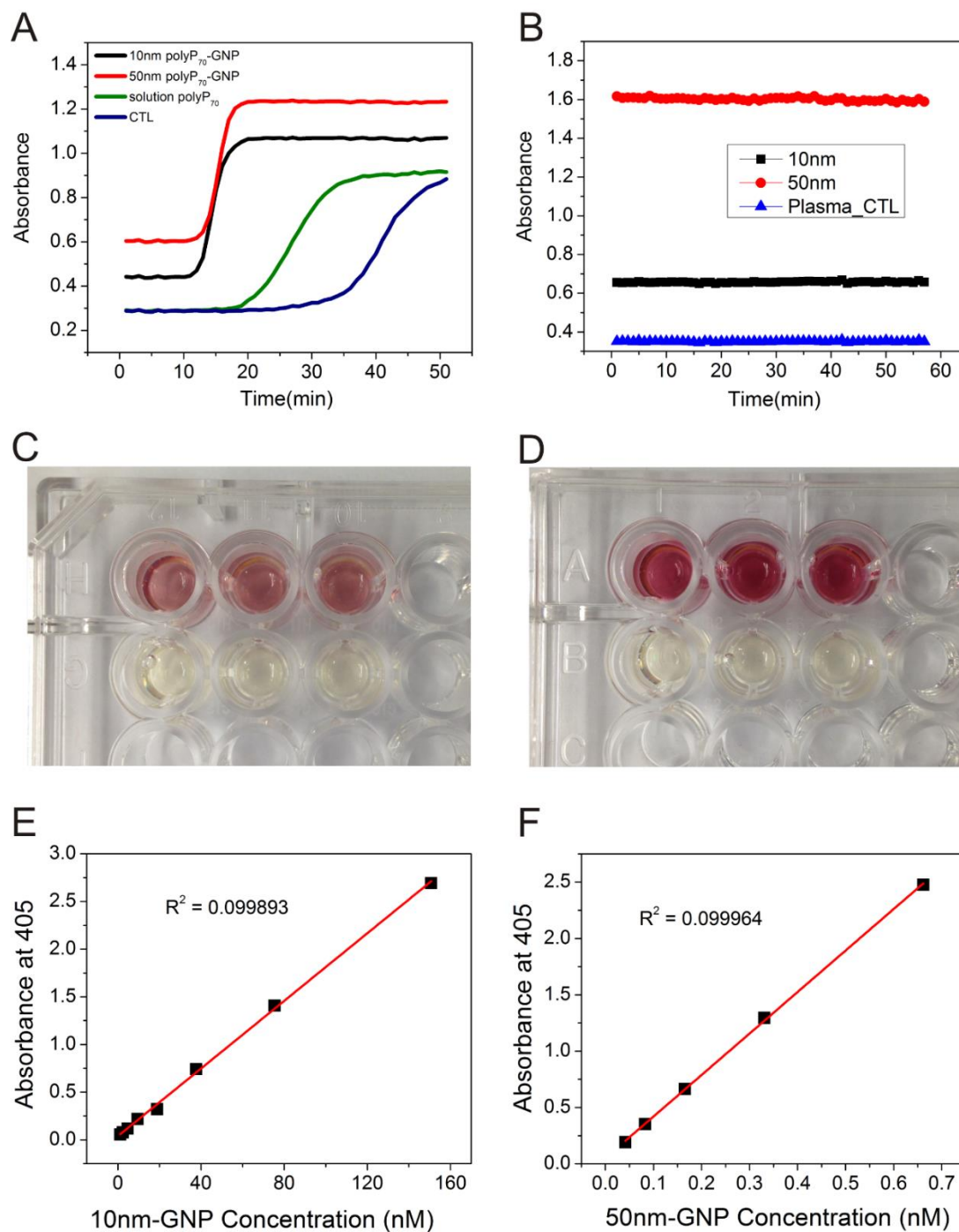


Figure 5-5. Control absorbance experiments: (A) Actual (not normalized) absorbance traces of 10nm and 50nm polyP₇₀-GNPs at 5 μ M monoP. (B) Absorbance traces (at 405nm) of 10nm and 50nm polyP₇₀-GNPs incubated at high concentration with plasma over time. (C) 50nm polyP₇₀-GNPs after one hour incubation in PNP (without CaCl₂). (D) 10nm polyP₇₀-GNPs after one hour

incubation in PNP (without CaCl_2). (E) Linearity of 10nm-GNP concentration with A_{405} . (F) Linearity of 50nm-GNP concentration with A_{405} .

Figure 5-6A shows the clotting outcomes (measured by increase in turbidity) of the 10nm polyP₇₀-GNPs. PolyP₇₀-GNPs manifest a marked increase in turbidity long before polyP₇₀ in solution or control with no activator present. Completely PEGylated GNPs likewise do not robustly initiate the contact pathway, with a clotting time between molecularly dissolved polyP₇₀ in solution and the control (with no activator present). The citrated 10nm GNPs (bulk), at the same GNP concentration as the 10nm polyP₇₀-GNP sample, possess some ability to initiate the contact pathway of clotting, but they are significantly less efficacious than the 10nm polyP₇₀-GNPs. **Figure 5-6A** depicts the clotting behavior of 10nm and 50nm polyP₇₀ -GNPs at 5 μM monoP. All GNPs conjugated with polyP₇₀ clot in approximately 10 min, while polyP₇₀ in solution coagulates at approximately 25 min, while the control (with no activator present) trails at 35-40 min. The turbidity measurements were all performed at room temperature, and the time to coagulation will in practice be much longer than those obtained by coagulometry at 37°C. Regardless, the equivalent trends in procoagulant efficacy between samples are apparent after short inspection. These data further corroborate coagulometric measurements presented above that nanoscale confinement of polyP₇₀ onto a colloidal surface transforms the weak contact activator polyP₇₀ into a robust agent, mimicking polyP chains more than ten times larger.

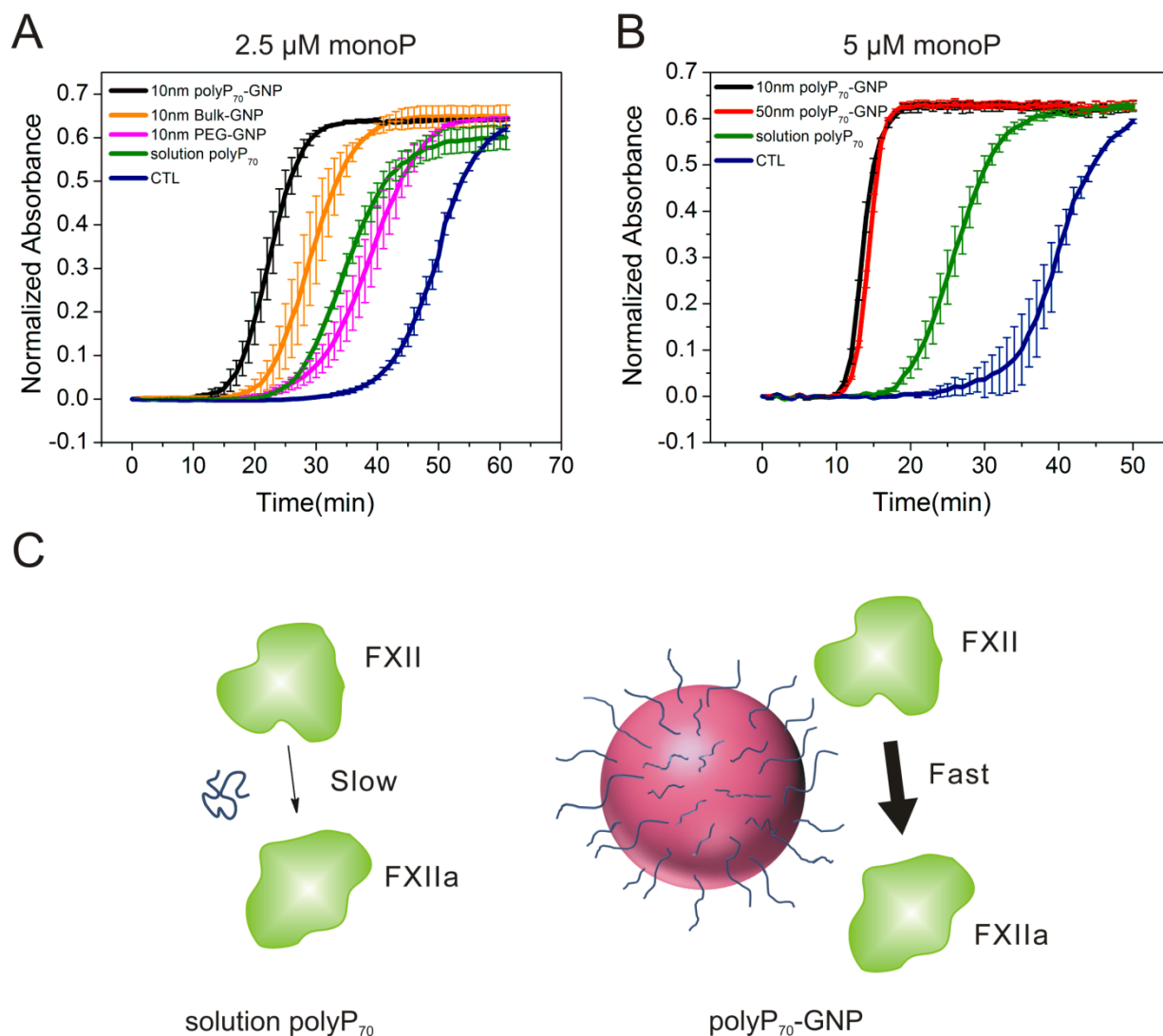


Figure 5-6. Procoagulant activity of polyP₇₀-GNPs assayed by A₄₀₅ turbidity in PNP. (A) Normalized absorbance traces of 10nm polyP₇₀-GNPs at 2.5 μM monoP (n=3, \pm S.E.) compared to PEGylated GNP and citrate GNP with the same GNP concentration, and molecularly dissolved polyP₇₀; (B) Normalized absorbance traces of 10nm and 50nm polyP₇₀-GNPs at 5 μM monoP (n=3, \pm S.E.) compared to molecularly dissolved polyP₇₀. (C) Differential clotting activation of colloiddally-anchored and solution-phase polyP₇₀. Colloidal clustering of polyP promotes rapid initiation of the contact pathway of clotting by serving as a surface for the

assembly of the primary complex, whereas polyP₇₀ in solution is only marginally capable of FXII zymogen activation.

5.4 Conclusions

In the present investigation we lay the groundwork for the implementation of a novel, potentially injectable hemostat for treating a constellation of internal and external hemorrhagic phenomena through the conjugation of platelet-sized polyP to colloidal GNPs, facilitated by phosphoramidation to the disulfide cystamine. Although many negatively charged moieties have been shown to initiate the contact pathway of blood clotting,¹⁸⁶ using polyP has the unique advantages, in that it is naturally secreted by human platelets and in addition to FXII, polyP also interacts with FXI, FV, and thrombin to accelerate clotting. Moreover, our data indicated that the procoagulant effect of polyP conjugated on gold nanoparticles is orders of magnitude greater than any other (as yet) identified anionic polymer.^{143, 145, 146} Procoagulant outcomes, measured by conventional contact activity assays in human blood plasma, indicate that they exert significant reductions in the time to clot. Covalent conjugation to the colloidal surface transforms platelet-sized polyP₇₀ into a very robust contact surface, similar to that of the potent activator long-chain polyP. These data offer strong support to the claim that clustering of shorter polymers at high local concentrations is equivalent to having much longer polymers dispersed in solution phase for modulation of blood coagulation and other threshold-switchable networks.

The procoagulant activity characteristic of the polyP₇₀-GNPs is a meaningful step forward in the development of an on-demand, minimally invasive, targeted hemostat, and surprisingly reminiscent of the threshold-switchable properties of the coagulation cascade itself. Localization of procoagulant activators above crucial threshold concentrations accomplished in physiological contexts allows for swift propagation of the hemostatic signal to achieve wound

healing. Organisms have adapted these nonlinear processes capable of exponential amplification, counterbalanced by negative feedback mechanisms, to harbor a rapid response to potentially catastrophic injury, always maintaining this delicate equilibrium of hemostasis essential for survival. The synthesis of polyP₇₀-GNPs therefore may fulfill a need for the treatment of a variety of bleeding phenomena, its methodology inspired by nature's nonlinear, threshold-switchable processes.

6 CONCLUSIONS

This thesis provides a perspective on the design, formation, and characterization of nanoparticles for enhanced drug bioavailability and functionality.

In chapter 2, we discussed the development of the FPaD process to produce polymeric nanoparticles encapsulating poorly water-soluble compounds with high drug loading, controllable size and surface properties, and long-term stability. The feasibility of the process was confirmed by successful polymeric formulations of several small-molecule hydrophobic compounds such as curcumin, N1-(3-chlorophenyl)-2-cycloheptylidenehydrazine-1-carbothioamide, 2-chlorobenzaldehyde 1-(4-phenyl-1,3-thiazol-2-yl)hydrazone hydrochloride, and larger-molecular weight peptides – anticoagulant Myr-FEEERA and anti-tuberculosis - ecumicin.

We next sought to investigate the potential biomedical applications of the synthesized nanoformulations that were generated by the method discussed in the previous chapter (Chapter 2). The biodistribution of curcumin and its major metabolite – curcumin glucuronide was investigated after oral delivery of nano-curcumin (curcumin encapsulated in PLGA nanoparticles). Pharmacokinetic analysis demonstrated approximately 20-fold reduction in dose requirement when compared to unformulated curcumin to achieve comparable curcumin plasma and central nervous system (CNS) tissue concentrations. Furthermore, the highly selective and validated liquid chromatography-mass spectrometry (LC-MS) method was developed to clearly distinguish curcumin from its major metabolite (curcumin glucuronide).

The characterization studies of a wide variety of potential polymeric drug carriers via state-of-the-art SAXS measurements were demonstrated in Chapter 4. This method of characterization revealed the internal features of the polymeric micelles synthesized by the FNP

process. The insightful structural information of the micelles is essential for the adequate design of the nanocarriers for drug delivery applications as the size of the core and the shell play an important role in tailoring nanoparticles properties and their biological fate. The complementary techniques such as dynamic light scattering (DLS) and transmission electron microscopy (TEM) were also used and compared.

The final set of studies in Chapter 5 demonstrated surface modification of nanoparticles for enhanced drug functionality. A facile phosphoramidate coupling chemistry was used to conjugate hydrophilic polymer – polyphosphate with inorganic gold nanoparticles. Colloidal confinement of this polymer (70 repeating phosphate units) on the surface of the nanoparticles resulted in enhanced procoagulant activity of polyphosphate with the ability of faster contact pathway activation. Furthermore, the efficacy of the newly synthesized nanoparticles was found to be equivalent to that of polymer chains more than ten times longer, lengths traditionally associated with being robust contact activators. With additional functionalization, these polyphosphate-functionalized gold nanoparticles (polyp-GNPs) can be effectively used to target internal hemorrhage.

REFERENCES

1. Cho, K.; Wang, X.; Nie, S.; Shin, D. M. *Clinical cancer research* **2008**, 14, (5), 1310-1316.
2. Zhou, J.; Patel, T. R.; Sirianni, R. W.; Strohhahn, G.; Zheng, M.-Q.; Duong, N.; Schafbauer, T.; Huttner, A. J.; Huang, Y.; Carson, R. E. *Proceedings of the National Academy of sciences* **2013**, 110, (29), 11751-11756.
3. Shenoy, D. B.; Amiji, M. M. *International journal of pharmaceutics* **2005**, 293, (1), 261-270.
4. de la Fuente, J. M. a. G. V., *Nanobiotechnology: Inorganic Nanoparticles vs. Organic Nanoparticles*. Elsevier: Oxford, U.K., 2012.
5. Rösler, A.; Vandermeulen, G. W.; Klok, H.-A. *Advanced drug delivery reviews* **2012**, 64, 270-279.
6. Antonietti, M.; Förster, S. *Advanced Materials* **2003**, 15, (16), 1323-1333.
7. Raghavan, S. R.; Fritz, G.; Kaler, E. W. *Langmuir* **2002**, 18, (10), 3797-3803.
8. Kelly, K. L.; Coronado, E.; Zhao, L. L.; Schatz, G. C. *The Journal of Physical Chemistry B* **2003**, 107, (3), 668-677.
9. Nehl, C. L.; Liao, H.; Hafner, J. H. *Nano letters* **2006**, 6, (4), 683-688.
10. Corot, C.; Robert, P.; Idée, J.-M.; Port, M. *Advanced drug delivery reviews* **2006**, 58, (14), 1471-1504.
11. Xu, Z.; Hou, Y.; Sun, S. *J Am Chem Soc* **2007**, 129, (28), 8698-8699.
12. Seo, W. S.; Jo, H. H.; Lee, K.; Kim, B.; Oh, S. J.; Park, J. T. *Angewandte Chemie International Edition* **2004**, 43, (9), 1115-1117.
13. Medintz, I. L.; Uyeda, H. T.; Goldman, E. R.; Mattoussi, H. *Nature materials* **2005**, 4, (6), 435-446.
14. Pinaud, F.; Michalet, X.; Bentolila, L. A.; Tsay, J. M.; Doose, S.; Li, J. J.; Iyer, G.; Weiss, S. *Biomaterials* **2006**, 27, (9), 1679-1687.
15. Noyes, A. A.; Whitney, W. R. *J Am Chem Soc* **1897**, 19, (12), 930-934.
16. Byrappa, K.; Ohara, S.; Adschiri, T. *Advanced Drug Delivery Reviews* **2008**, 60, (3), 299-327.
17. Reverchon, E.; Caputo, G.; De Marco, I. *Industrial & Engineering Chemistry Research* **2003**, 42, (25), 6406-6414.
18. Lee, L. Y.; Wang, C. H.; Smith, K. A. *Journal of Controlled Release* **2008**, 125, (2), 96-106.
19. York, P. *Pharmaceutical science & technology today* **1999**, 2, (11), 430-440.
20. Gurny, R.; Peppas, N.; Harrington, D.; Banker, G. *Drug Development and Industrial Pharmacy* **1981**, 7, (1), 1-25.
21. Leroux, J.-C.; Allémann, E.; Doelker, E.; Gurny, R. *European journal of pharmaceutics and biopharmaceutics* **1995**, 41, (1), 14-18.
22. Kwon, H.-Y.; Lee, J.-Y.; Choi, S.-W.; Jang, Y.; Kim, J.-H. *Colloids and Surfaces A: Physicochemical and Engineering Aspects* **2001**, 182, (1), 123-130.
23. Ibrahim, H.; Bindschadler, C.; Doelker, E.; Buri, P.; Gurny, R. *International journal of pharmaceutics* **1992**, 87, (1-3), 239-246.
24. Leroux, J.-C.; Allémann, E.; De Jaeghere, F.; Doelker, E.; Gurny, R. *Journal of Controlled Release* **1996**, 39, (2), 339-350.
25. Fessi, H.; Devissaguet, J. P.; Puisieux, F.; Thies, C. *French patent* **1986**, 2, 988.

26. Johnson, B. K.; Prud'homme, R. K. *Australian Journal of Chemistry* **2003**, 56, 1021-1024.
27. Liu, Y.; Cheng, C.; Prud'homme, R. K.; Fox, R. O. *Chemical Engineering Science* **2008**, 63, (11), 2829-2842.
28. Verma, A.; Simard, J. M.; Worrall, J. W.; Rotello, V. M. *J Am Chem Soc* **2004**, 126, (43), 13987-13991.
29. Liu, D.; Wu, W.; Ling, J.; Wen, S.; Gu, N.; Zhang, X. *Advanced Functional Materials* **2011**, 21, (8), 1498-1504.
30. Mitchell, G. P.; Mirkin, C. A.; Letsinger, R. L. *J Am Chem Soc* **1999**, 121, (35), 8122-8123.
31. Owens, D. E.; Peppas, N. A. *International journal of pharmaceutics* **2006**, 307, (1), 93-102.
32. Zhang, Y.; Kohler, N.; Zhang, M. *Biomaterials* **2002**, 23, (7), 1553-1561.
33. Kim, D.; Park, S.; Lee, J. H.; Jeong, Y. Y.; Jon, S. *J Am Chem Soc* **2007**, 129, (24), 7661-7665.
34. Feng, L.; Wang, Y.; Wang, N.; Ma, Y. *Polymer bulletin* **2009**, 63, (3), 313-327.
35. Hermanson, G. T., *Bioconjugate techniques*. Academic press: 2013.
36. Ghosh, P.; Han, G.; De, M.; Kim, C. K.; Rotello, V. M. *Advanced drug delivery reviews* **2008**, 60, (11), 1307-1315.
37. Wang, F.; Wang, Y.-C.; Dou, S.; Xiong, M.-H.; Sun, T.-M.; Wang, J. *Acs Nano* **2011**, 5, (5), 3679-3692.
38. Kievit, F. M.; Wang, F. Y.; Fang, C.; Mok, H.; Wang, K.; Silber, J. R.; Ellenbogen, R. G.; Zhang, M. *Journal of controlled release* **2011**, 152, (1), 76-83.
39. Kalmodia, S.; Vandhana, S.; Rama, B. T.; Jayashree, B.; Seethalakshmi, T. S.; Umashankar, V.; Yang, W.; Barrow, C. J.; Krishnakumar, S.; Elchuri, S. V. *Cancer nanotechnology* **2016**, 7, (1), 1.
40. Brown, S. D.; Nativo, P.; Smith, J.-A.; Stirling, D.; Edwards, P. R.; Venugopal, B.; Flint, D. J.; Plumb, J. A.; Graham, D.; Wheate, N. J. *J Am Chem Soc* **2010**, 132, (13), 4678-4684.
41. Nobs, L.; Buchegger, F.; Gurny, R.; Allémann, E. *Journal of pharmaceutical sciences* **2004**, 93, (8), 1980-1992.
42. Cheng, J.; Teply, B. A.; Sherifi, I.; Sung, J.; Luther, G.; Gu, F. X.; Levy-Nissenbaum, E.; Radovic-Moreno, A. F.; Langer, R.; Farokhzad, O. C. *Biomaterials* **2007**, 28, (5), 869-876.
43. Chu, B. **1991**.
44. Schmitz, K. S. **1990**.
45. Mayer, A.; Antonietti, M. *Colloid and Polymer Science* **1998**, 276, (9), 769-779.
46. Serizawa, T.; Takehara, S.; Akashi, M. *Macromolecules* **2000**, 33, (5), 1759-1764.
47. Srnová-Šloufová, I.; Lednický, F.; Gemperle, A.; Gemperlová, J. *Langmuir* **2000**, 16, (25), 9928-9935.
48. Won, Y.-Y.; Brannan, A. K.; Davis, H. T.; Bates, F. S. *The Journal of Physical Chemistry B* **2002**, 106, (13), 3354-3364.
49. Almgren, M.; Edwards, K.; Karlsson, G. *Colloids and Surfaces A: Physicochemical and Engineering Aspects* **2000**, 174, (1), 3-21.
50. Wang, C.; Qiao, Q.; Shokuhfar, T.; Klie, R. F. *Advanced Materials* **2014**, 26, (21), 3410-3414.
51. Pedersen, J. S.; Svaneborg, C. *Current opinion in colloid & interface science* **2002**, 7, (3), 158-166.

52. A. Guinier, G. F., *Small-angle scattering of x-rays*. John Wiley and Sons: New York, 1955.
53. Willner, L.; Poppe, A.; Allgaier, J.; Monkenbusch, M.; Richter, D. *EPL (Europhysics Letters)* **2001**, 55, (5), 667.
54. Lund, R.; Willner, L.; Monkenbusch, M.; Panine, P.; Narayanan, T.; Colmenero, J.; Richter, D. *Physical review letters* **2009**, 102, (18), 188301.
55. Loftsson, T.; Brewster, M. E. *Journal of Pharmacy and Pharmacology* **2010**, 62, (11), 1607-1621.
56. Gursoy, R. N.; Benita, S. *Biomedicine & Pharmacotherapy* **2004**, 58, (3), 173-182.
57. Lipinski, C. A. *American Pharmaceutical Review* **2002**, 5, 82-85.
58. Kumari, A.; Yadav, S. K.; Yadav, S. C. *Colloids and Surfaces B: Biointerfaces* **2010**, 75, (1), 1-18.
59. Soppimath, K. S.; Aminabhavi, T. M.; Kulkarni, A. R.; Rudzinski, W. E. *Journal of controlled release* **2001**, 70, (1), 1-20.
60. Shen, H.; Hong, S.; Prud'homme, R.; Liu, Y. *Journal of Nanoparticle Research* **2011**, 13, (9), 4109-4120.
61. Lin, J.-K.; Lin-Shiau, S.-Y. *Proceedings of the National Science Council, Republic of China. Part B, Life Sciences* **2001**, 25, (2), 59-66.
62. Kim, M. K.; Choi, G. J.; Lee, H. S. *Journal of Agricultural and Food Chemistry* **2003**, 51, (6), 1578-1581.
63. Lubbad, A.; Oriowo, M. A.; Khan, I. *Molecular and Cellular Biochemistry* **2009**, 322, (1-2), 127-135.
64. Shen, H.; Hu, X. Y.; Szymusiak, M.; Wang, Z. J.; Liu, Y. *Molecular Pharmaceutics* **2013**, 10, (12), 4546-4551.
65. Hu, X. H. F. S., M.; Liu, Y.; Wang, Z.J.; *The Journal of Pharmacology and Experimental Therapeutics* **2015**, 352, 1-9.
66. Shen, H.; Banerjee, A. A.; Mlynarska, P.; Hautman, M.; Hong, S.; Kapetanovic, I. M.; Lyubimov, A. V.; Liu, Y. *Journal of Pharmaceutical Sciences* **2012**, 101, (10), 3877-3885.
67. Chow, S. F.; Sun, C. C.; Chow, A. H. L. *European Journal of Pharmaceutics and Biopharmaceutics* **2014**, 88, (2), 462-471.
68. Zhu, Z. *Molecular pharmaceutics* **2014**, 11, (3), 776-786.
69. Zhu, Z.; Anacker, J. L.; Ji, S.; Hoyer, T. R.; Macosko, C. W.; Prud'homme, R. K. *Langmuir* **2007**, 23, (21), 10499-10504.
70. Liu, Y.; Tong, Z.; Prud'homme, R. K. *Pest management science* **2008**, 64, (8), 808-812.
71. Teagarden, D. L.; Baker, D. S. *European Journal of Pharmaceutical Sciences* **2002**, 15, (2), 115-133.
72. Abdelwahed, W.; Degobert, G.; Stainmesse, S.; Fessi, H. *Advanced drug delivery reviews* **2006**, 58, (15), 1688-1713.
73. Saez, A.; Guzman, M.; Molpeceres, J.; Aberturas, M. *European Journal of Pharmaceutics and Biopharmaceutics* **2000**, 50, (3), 379-387.
74. Quintanar-Guerrero, D.; Ganem-Quintanar, A.; Allémann, E.; Fessi, H.; Doelker, E. *Journal of microencapsulation* **1998**, 15, (1), 107-119.
75. Sameti, M.; Bohr, G.; Kumar, M. R.; Kneuer, C.; Bakowsky, U.; Nacken, M.; Schmidt, H.; Lehr, C.-M. *International journal of pharmaceutics* **2003**, 266, (1), 51-60.
76. Abdelwahed, W.; Degobert, G.; Fessi, H. *International journal of pharmaceutics* **2006**, 309, (1), 178-188.

77. Nemati, F.; Cavé, G.; Couvreur, P. *Assoc. Pharm. Galenique Ind., Chatenay Malabry* **1992**, 3, 487-493.
78. Oh, K. S.; Lee, K. E.; Han, S. S.; Cho, S. H.; Kim, D.; Yuk, S. H. *Biomacromolecules* **2005**, 6, (2), 1062-1067.
79. Chacon, M.; Molpeceres, J.; Berges, L.; Guzman, M.; Aberturas, M. *European Journal of Pharmaceutical Sciences* **1999**, 8, (2), 99-107.
80. Crowe, L. M.; Reid, D. S.; Crowe, J. H. *Biophysical journal* **1996**, 71, (4), 2087.
81. Crowe, J. H.; Hoekstra, F. A.; Crowe, L. M. *Annual Review of Physiology* **1992**, 54, (1), 579-599.
82. Chow, S. F.; Wan, K. Y.; Cheng, K. K.; Wong, K. W.; Sun, C. C.; Baum, L.; Chow, A. H. L. *European Journal of Pharmaceutics and Biopharmaceutics* **2015**, 94, 436-449.
83. Sharma, O. P. *Biochemical Pharmacology* **1976**, 25, (15), 1811-1812.
84. Jefremov, V.; Zilmer, M.; Zilmer, K.; Bogdanovic, N.; Karelson, E. *Signal Transduction Pathways, Pt C* **2007**, 1095, 449-457.
85. Reddy, R. C.; Vatsala, P. G.; Keshamouni, V. G.; Padmanaban, G.; Rangarajan, P. N. *Biochemical and Biophysical Research Communications* **2005**, 326, (2), 472-474.
86. Cole, G. M.; Teter, B.; Frautschy, S. A. *Molecular Targets and Therapeutic Uses of Curcumin in Health and Disease* **2007**, 595, 197-212.
87. Liu, A. C.; Lou, H. X.; Zhao, L. X.; Fan, P. H. *Journal of Pharmaceutical and Biomedical Analysis* **2006**, 40, (3), 720-727.
88. Tapal, A.; Tiku, P. K. *Food Chemistry* **2012**, 130, (4), 960-965.
89. Shoba, G.; Joy, D.; Joseph, T.; Majeed, M.; Rajendran, R.; Srinivas, P. S. S. R. *Planta Medica* **1998**, 64, (4), 353-356.
90. Grill, A. E.; Koniar, B.; Panyam, J. *Drug Delivery and Translational Research* **2014**, 4, (4), 344-352.
91. Tsai, Y. M.; Chang-Liao, W. L.; Chien, C. F.; Lin, L. C.; Tsai, T. H. *International Journal of Nanomedicine* **2012**, 7, 2957-2966.
92. Khalil, N. M.; do Nascimento, T. C. F.; Casa, D. M.; Dalmolin, L. F.; de Mattos, A. C.; Hoss, I.; Romano, M. A.; Mainardes, R. M. *Colloids and Surfaces B-Biointerfaces* **2013**, 101, 353-360.
93. Tsai, Y. M.; Jan, W. C.; Chien, C. F.; Lee, W. C.; Lin, L. C.; Tsai, T. H. *Food Chemistry* **2011**, 127, (3), 918-925.
94. Xie, X. X.; Tao, Q.; Zou, Y. N.; Zhang, F. Y.; Guo, M.; Wang, Y.; Wang, H.; Zhou, Q.; Yu, S. Q. *Journal of Agricultural and Food Chemistry* **2011**, 59, (17), 9280-9289.
95. Takahashi, M.; Uechi, S.; Takara, K.; Asikin, Y.; Wada, K. *Journal of Agricultural and Food Chemistry* **2009**, 57, (19), 9141-9146.
96. Li, L.; Braiteh, F. S.; Kurzrock, R. *Cancer* **2005**, 104, (6), 1322-1331.
97. Li, L.; Ahmed, B.; Mehta, K.; Kurzrock, R. *Molecular Cancer Therapeutics* **2007**, 6, (4), 1276-1282.
98. Banerjee, A. A.; Shen, H.; Hautman, M.; Anwer, J.; Hong, S.; Kapetanovic, I. M.; Liu, Y.; Lyubimov, A. V. *Current Pharmaceutical Biotechnology* **2013**, 14, (4), 464-469.
99. Tang, L.; Shukla, P. K.; Wang, L. X.; Wang, Z. J. *J Pharmacol Exp Ther* **2006**, 317, (2), 901-9.
100. Yang, C.; Chen, Y.; Tang, L.; Wang, Z. J. *J Pharmacol Exp Ther* **2011**, 338, (1), 164-72.
101. Shen, H.; Hong, S. Y.; Prud'homme, R. K.; Liu, Y. *Journal of Nanoparticle Research* **2011**, 13, (9), 4109-4120.

102. Wahlstrom, B.; Blennow, G. *Acta Pharmacologica Et Toxicologica* **1978**, 43, (2), 86-92.
103. Hoehle, S. I.; Pfeiffer, E.; Metzler, M. *Molecular Nutrition & Food Research* **2007**, 51, (8), 932-938.
104. Sasaki, H.; Sunagawa, Y.; Takahashi, K.; Imaizumi, A.; Fukuda, H.; Hashimoto, T.; Wada, H.; Katanasaka, Y.; Kakeya, H.; Fujita, M.; Hasegawa, K.; Morimoto, T. *Biological & Pharmaceutical Bulletin* **2011**, 34, (5), 660-665.
105. Kanai, M.; Imaizumi, A.; Otsuka, Y.; Sasaki, H.; Hashiguchi, M.; Tsujiko, K.; Matsumoto, S.; Ishiguro, H.; Chiba, T. *Cancer Chemotherapy and Pharmacology* **2012**, 69, (1), 65-70.
106. Pal, A.; Sung, B.; Prasad, B. A. B.; Schuber, P. T.; Prasad, S.; Aggarwal, B. B.; Bornmann, W. G. *Bioorganic & Medicinal Chemistry* **2014**, 22, (1), 435-439.
107. Ireson, C.; Orr, S.; Jones, D. J. L.; Verschoyle, R.; Lim, C. K.; Luo, J. L.; Howells, L.; Plummer, S.; Jukes, R.; Williams, M.; Steward, W. P.; Gescher, A. *Cancer Research* **2001**, 61, (3), 1058-1064.
108. Antony, B.; Merina, B.; Iyer, V. S.; Judy, N.; Lennertz, K.; Joyal, S. *Indian journal of pharmaceutical sciences* **2008**, 70, (4), 445-9.
109. Cheng, K. K.; Yeung, C. F.; Ho, S. W.; Chow, S. F.; Chow, A. H. L.; Baum, L. *Aaps Journal* **2013**, 15, (2), 324-336.
110. Sharma, R. A.; Euden, S. A.; Platton, S. L.; Cooke, D. N.; Shafayat, A.; Hewitt, H. R.; Marczylo, T. H.; Morgan, B.; Hemingway, D.; Plummer, S. M.; Pirmohamed, M.; Gescher, A. J.; Steward, W. P. *Clinical Cancer Research* **2004**, 10, (20), 6847-6854.
111. Chen, Y.; Yang, C.; Wang, Z. J. *The Journal of neuroscience : the official journal of the Society for Neuroscience* **2010**, 30, (1), 38-46.
112. Shoji, M.; Nakagawa, K.; Watanabe, A.; Tsuduki, T.; Yamada, T.; Kuwahara, S.; Kimura, F.; Miyazawa, T. *Food Chemistry* **2014**, 151, 126-132.
113. Ishisaka, A.; Kawabata, K.; Miki, S.; Shiba, Y.; Minekawa, S.; Nishikawa, T.; Mukai, R.; Terao, J.; Kawai, Y. *Plos One* **2013**, 8, (11).
114. Shimoi, K.; Nakayama, T. *Phase II Conjugation Enzymes and Transport Systems* **2005**, 400, 263-272.
115. Sperker, B.; Werner, U.; Murdter, T. E.; Tekkaya, C.; Fritz, P.; Wacke, R.; Adam, U.; Gerken, M.; Drewelow, B.; Kroemer, H. K. *Naunyn-Schmiedebergs Archives of Pharmacology* **2000**, 362, (2), 110-115.
116. Marshall, T.; Shult, P.; Busse, W. W. *Journal of Allergy and Clinical Immunology* **1988**, 82, (4), 550-555.
117. Riley, T.; Heald, C. R.; Stolnik, S.; Garnett, M. C.; Illum, L.; Davis, S. S.; King, S. M.; Heenan, R. K.; Purkiss, S. C.; Barlow, R. J.; Gellert, P. R.; Washington, C. *Langmuir* **2003**, 19, (20), 8428-8435.
118. Gaucher, G.; Dufresne, M.-H.; Sant, V. P.; Kang, N.; Maysinger, D.; Leroux, J.-C. *Journal of Controlled Release* **2005**, 109, (1), 169-188.
119. Stolnik, S.; Illum, L.; Davis, S. S. *Adv Drug Deliver Rev* **1995**, 16, (2-3), 195-214.
120. Kwon, G. S.; Okano, T. *Adv Drug Deliver Rev* **1996**, 21, (2), 107-116.
121. Hu, K.; Li, J.; Shen, Y.; Lu, W.; Gao, X.; Zhang, Q.; Jiang, X. *Journal of controlled release* **2009**, 134, (1), 55-61.
122. Agrawal, S. K.; Sanabria-DeLong, N.; Coburn, J. M.; Tew, G. N.; Bhatia, S. R. *Journal of controlled release* **2006**, 112, (1), 64-71.

123. Peracchia, M. T.; Gref, R.; Minamitake, Y.; Domb, A.; Lotan, N.; Langer, R. *Journal of Controlled Release* **1997**, 46, (3), 223-231.
124. Batrakova, E. V.; Kabanov, A. V. *Journal of Controlled Release* **2008**, 130, (2), 98-106.
125. Vangeyte, P.; Leyh, B.; Heinrich, M.; Grandjean, J.; Bourgaux, C.; Jerome, R. *Langmuir* **2004**, 20, (20), 8442-8451.
126. Jada, A.; Hurtrez, G.; Siffert, B.; Riess, G. *Macromol Chem Physic* **1996**, 197, (11), 3697-3710.
127. Jensen, G. V.; Shi, Q.; Hernansanz, M. J.; Oliveira, C. L.; Deen, G. R.; Almdal, K.; Pedersen, J. S. *Journal of Applied Crystallography* **2011**, 44, (3), 473-482.
128. Du, J.-Z.; Tang, L.-Y.; Song, W.-J.; Shi, Y.; Wang, J. *Biomacromolecules* **2009**, 10, (8), 2169-2174.
129. Luo, H. Y.; Santos, J. L.; Herrera-Alonso, M. *Chem Commun* **2014**, 50, (5), 536-538.
130. Konarev, P. V.; Volkov, V. V.; Sokolova, A. V.; Koch, M. H.; Svergun, D. I. *Journal of applied crystallography* **2003**, 36, (5), 1277-1282.
131. Kline, S. R. *Journal of applied crystallography* **2006**, 39, (6), 895-900.
132. Orthaber, D.; Bergmann, A.; Glatter, O. *J Appl Crystallogr* **2000**, 33, 218-225.
133. Hagan, S.; Coombes, A.; Garnett, M.; Dunn, S.; Davies, M.; Illum, L.; Davis, S.; Harding, S.; Purkiss, S.; Gellert, P. *Langmuir* **1996**, 12, (9), 2153-2161.
134. Shen, H.; Hong, S.; Prud'homme, R. K.; Liu, Y. *Journal of Nanoparticle Research* **2011**, 13, (9), 4109-4120.
135. Giacomelli, C.; Borsali, R. In *Morphology of Poly (ethylene oxide) - block - Polycaprolatone Block Copolymer Micelles Controlled via the Preparation Method*, Macromolecular Symposia, 2006; Wiley Online Library: pp 147-153.
136. Schuetz, P.; Greenall, M. J.; Bent, J.; Furzeland, S.; Atkins, D.; Butler, M. F.; McLeish, T. C.; Buzza, D. M. A. *Soft Matter* **2011**, 7, (2), 749-759.
137. Cai, S.; Vijayan, K.; Cheng, D.; Lima, E. M.; Discher, D. E. *Pharmaceutical Research* **2007**, 24, (11), 2099-2109.
138. Nagarajan, R.; Ganesh, K. *The Journal of Chemical Physics* **1989**, 90, (10), 5843-5856.
139. Glatter, O. *J Appl Crystallogr* **1979**, 12, (2), 166-175.
140. Brown, M. R. W.; Kornberg, A. *P Natl Acad Sci USA* **2004**, 101, (46), 16085-16087.
141. Morrissey, J. H.; Choi, S. H.; Smith, S. A. *Blood* **2012**, 119, (25), 5972-5979.
142. Kornberg, A. *J Bacteriol* **1995**, 177, (3), 491-496.
143. Smith, S. A.; Mutch, N. J.; Baskar, D.; Rohloff, P.; Docampo, R.; Morrissey, J. H. *P Natl Acad Sci USA* **2006**, 103, (4), 903-908.
144. Smith, S. A.; Morrissey, J. H. *Blood* **2008**, 112, (7), 2810-2816.
145. Smith, S. A.; Choi, S. H.; Davis-Harrison, R.; Huyck, J.; Boettcher, J.; Reinstra, C. M.; Morrissey, J. H. *Blood* **2010**, 116, (20), 4353-4359.
146. Choi, S. H.; Smith, S. A.; Morrissey, J. H. *Blood* **2011**, 118, (26), 6963-6970.
147. Han, K. Y.; Hong, B. S.; Yoon, Y. J.; Yoon, C. M.; Kim, Y. K.; Kwon, Y. G.; Gho, Y. S. *Biochem J* **2007**, 406, 49-55.
148. Rashid, M. H.; Rumbaugh, K.; Passador, L.; Davies, D. G.; Hamood, A. N.; Iglewski, B. H.; Kornberg, A. *P Natl Acad Sci USA* **2000**, 97, (17), 9636-9641.
149. Keasling, J. D. *Ann Ny Acad Sci* **1997**, 829, 242-249.
150. Reusch, R. N.; Sadoff, H. L. *P Natl Acad Sci USA* **1988**, 85, (12), 4176-4180.
151. Gezelius, K. *Archives of microbiology* **1974**, 98, (4), 311-29.

152. Zhang, H.; Gomez-Garcia, M. R.; Brown, M. R.; Kornberg, A. *Proceedings of the National Academy of Sciences of the United States of America* **2005**, 102, (8), 2731-5.
153. Noegel, A.; Gotschlich, E. C. *J Exp Med* **1983**, 157, (6), 2049-2060.
154. Docampo, R.; Moreno, S. N. J. *Parasitol Today* **1999**, 15, (11), 443-448.
155. Ruiz, F. A.; Lea, C. R.; Oldfield, E.; Docampo, R. *The Journal of biological chemistry* **2004**, 279, (43), 44250-7.
156. Donovan, A. J.; Kalkowski, J.; Smith, S. A.; Morrissey, J. H.; Liu, Y. *Biomacromolecules* **2014**.
157. Choi, S. H.; Collins, J. N. R.; Smith, S. A.; Davis-Harrison, R. L.; Rienstra, C. M.; Morrissey, J. H. *Biochemistry-Us* **2010**, 49, (45), 9935-9941.
158. Hebbard, C. F. F.; Wang, Y.; Baker, C. J.; Morrissey, J. H. *Biomacromolecules* **2014**, 15, (8), 3190-3196.
159. Renne, T. *Blood* **2010**, 116, (21), 1759-1759.
160. Bock, P. E.; Srinivasan, K. R.; Shore, J. D. *Biochemistry-Us* **1981**, 20, (25), 7258-7266.
161. Heimark, R. L.; Kurachi, K.; Fujikawa, K.; Davie, E. W. *Nature* **1980**, 286, (5772), 456-460.
162. Tans, G.; Rosing, J.; Griffin, J. H. *J Biol Chem* **1983**, 258, (13), 8215-8222.
163. Smith, S. A.; Morrissey, J. H. *Thromb Haemostasis* **2008**, 100, (1), 160-162.
164. Griffin, J. H. *P Natl Acad Sci USA* **1978**, 75, (4), 1998-2002.
165. Faxalv, L.; Boknas, N.; Strom, J. O.; Tengvall, P.; Theodorsson, E.; Ramstrom, S.; Lindahl, T. L. *Blood* **2013**, 122, (23), 3818-24.
166. Nickel, K. F.; Spronk, H. M.; Mutch, N. J.; Renne, T. *Blood* **2013**, 122, (23), 3847-9.
167. Muller, F.; Mutch, N. J.; Schenk, W. A.; Smith, S. A.; Esterl, L.; Spronk, H. M.; Schmidbauer, S.; Gahl, W. A.; Morrissey, J. H.; Renne, T. *Cell* **2009**, 139, (6), 1143-56.
168. Engel, R.; Brain, C. M.; Paget, J.; Lionikiene, A. S.; Mutch, N. J. *J Thromb Haemost* **2014**, 12, (9), 1513-1522.
169. Haake, P.; Ossip, P. S. *Tetrahedron Lett* **1970**, (55), 4841-&.
170. Garisson, A. W., Boozer, C. E. *J Am Chem Soc* **1968**, 80, (13), 3486-3494.
171. Mucha, A.; Grembecka, J.; Cierpicki, T.; Kafarski, P. *Eur J Org Chem* **2003**, (24), 4797-4803.
172. Mucha, A.; Kunert, A.; Grembecka, J.; Pawelczak, M.; Kafarski, P. *Eur J Med Chem* **2006**, 41, (6), 768-772.
173. Jacobsen, N. E.; Bartlett, P. A. *J Am Chem Soc* **1981**, 103, (3), 654-657.
174. Demers, L. M.; Mirkin, C. A.; Mucic, R. C.; Reynolds, R. A., 3rd; Letsinger, R. L.; Elghanian, R.; Viswanadham, G. *Analytical chemistry* **2000**, 72, (22), 5535-41.
175. Corbierre, M. K.; Cameron, N. S.; Lennox, R. B. *Langmuir* **2004**, 20, (7), 2867-2873.
176. Liu, Y. L.; Shipton, M. K.; Ryan, J.; Kaufman, E. D.; Franzen, S.; Feldheim, D. L. *Anal Chem* **2007**, 79, (6), 2221-2229.
177. Roca, M.; Pandya, N. H.; Nath, S.; Haes, A. J. *Langmuir* **2010**, 26, (3), 2035-2041.
178. Rickwood, D., *Centrifugation: A Practical Approach*. 2nd ed.; IRL press: Oxford, U.K. and Washington, D.C, 1984.
179. Jackson, C. M.; Nemerson, Y. *Annu Rev Biochem* **1980**, 49, 765-811.
180. Mandle, R. J.; Colman, R. W.; Kaplan, A. P. *P Natl Acad Sci USA* **1976**, 73, (11), 4179-4183.
181. Kushida, T.; Saha, K.; Subramani, C.; Nandwana, V.; Rotello, V. M. *Nanoscale* **2014**, 6, (23), 14484-14487.

182. Kim, K. M.; Kim, H. M.; Lee, W. J.; Lee, C. W.; Kim, T. I.; Lee, J. K.; Jeong, J.; Paek, S. M.; Oh, J. M. *Int J Nanomed* **2014**, 9, 29-40.
183. Greenwood, R.; Lapcikova, B.; Surynek, M.; Waters, K.; Lapcik, L. *Chem Pap* **2007**, 61, (2), 83-92.
184. Margolis, J. *The Australian journal of experimental biology and medical science* **1961**, 39, 249-58.
185. Zhu, S.; Diamond, S. L. *Thromb Res* **2014**, 134, (6), 1335-1343.
186. Oslakovic, C.; Cedervall, T.; Linse, S.; Dahlback, B. *Nanomed-Nanotechnol* **2012**, 8, (6), 981-986.

APPENDIX

Permission for use of published materials.



Thank You For Your Order!

Dear Dr. Magdalena Szymusiak,

Thank you for placing your order through Copyright Clearance Center's RightsLink service. Elsevier has partnered with RightsLink to license its content. This notice is a confirmation that your order was successful.

Your order details and publisher terms and conditions are available by clicking the link below:
<http://s100.copyright.com/CustomerAdmin/PLF.jsp?ref=932c675c-a047-4ca5-aaab-8186990fd461>

Order Details
Licensee: Magdalena Szymusiak
License Date: Jul 21, 2016
License Number: 3913661401706
Publication: International Journal of Pharmaceutics
Title: Bioavailability of Curcumin and Curcumin Glucuronide in the Central Nervous System of Mice after Oral Delivery of Nano-Curcumin
Type Of Use: reuse in a thesis/dissertation
Total: 0.00 USD

To access your account, please visit <https://myaccount.copyright.com>.

Please note: Online payments are charged immediately after order confirmation; invoices are issued daily and are payable immediately upon receipt.

To ensure that we are continuously improving our services, please take a moment to complete our [customer satisfaction survey](#).

B.1:v4.2

Title: Colloidal Confinement of
Polyphosphate on Gold
Nanoparticles Robustly Activates
the Contact Pathway of Blood
Coagulation

Author: Magdalena Szymusiak,
Alexander J. Donovan,
Stephanie A. Smith, et al

Publication: Bioconjugate Chemistry

Publisher: American Chemical Society

Date: Jan 1, 2016

Copyright © 2016, American Chemical Society

LOGIN

If you're a [copyright.com](#)
user, you can login to
RightsLink using your
copyright.com credentials.
Already a [RightsLink](#) user or
want to [learn more?](#)

PERMISSION/LICENSE IS GRANTED FOR YOUR ORDER AT NO CHARGE

This type of permission/license, instead of the standard Terms & Conditions, is sent to you because no fee is being charged for your order. Please note the following:

- Permission is granted for your request in both print and electronic formats, and translations.
- If figures and/or tables were requested, they may be adapted or used in part.
- Please print this page for your records and send a copy of it to your publisher/graduate school.
- Appropriate credit for the requested material should be given as follows: "Reprinted (adapted) with permission from (COMPLETE REFERENCE CITATION). Copyright (YEAR) American Chemical Society." Insert appropriate information in place of the capitalized words.
- One-time permission is granted only for the use specified in your request. No additional uses are granted (such as derivative works or other editions). For any other uses, please submit a new request.

BACK

CLOSE WINDOW

VITA

NAME: Magdalena Szymusiak

EDUCATION:

B.S., Major: Chemical Engineering, University of Illinois at Chicago, Chicago, USA, 2010

Ph.D., Major: Chemical Engineering, University of Illinois at Chicago, Chicago, USA, 2016

PUBLICATIONS:

1. Vishal Sharma, **Magdalena Szymusiak**, Hao Shen, Ludwig C. Nitsche, and Ying Liu, Formation of Polymeric Toroidal-Spiral Particles, *Langmuir*, 28(1), 729–735, 2012.
2. **Magdalena Szymusiak**, Vishal Sharma, Ludwig C. Nitsche and Ying Liu, Interaction of sedimenting drops in a miscible solution – formation of heterogeneous toroidal-spiral particles, *Soft Matter*, 8, 87556-7559, 2012.
3. Hao Shen, Xiaoyu Hu, **Magdalena Szymusiak**, Jim Wang, Ying Liu, Orally Administered Nano-curcumin to Attenuate Morphine Tolerance: Comparison between Negatively Charged PLGA and Partially and Fully PEGylated Nanoparticles, *Molecular Pharmaceutics*, 10 (12), 4546-4551, 2013.
4. Vishal Sharma, Melanie Kollmer, **Magdalena Szymusiak**, Ludwig C. Nitsche, Richard A. Gemeinhart, and Ying Liu, Toroidal-spiral particles for co-delivery of anti-VEGFR-2 antibody and irinotecan - a potential impant to hinder recurrence of glioblastoma multiforme, *Biomacromolecules*, 15 (3), 756-762, 2014.
5. Xiaoyu Hu, Fang Huang, **Magdalena Szymusiak**, Ying Liu and Zaijie Jim Wang, Curcumin attenuates opioid tolerance and dependence by inhibiting CaMKII α activity, *Journal of Pharmacology and Experimental Therapeutics*, 352 (3): 420-428, 2015.
6. **Magdalena Szymusiak**, Alexander J. Donovan, Stephanie A. Smith, Ross Ransom, Hao Shen, Joseph Kalkowski, James H. Morrissey and Ying Liu, Colloidal Confinement of Polyphosphate on Gold Nanoparticles Robustly Activates the Contact Pathway of Blood Coagulation, *Bioconjugate Chemistry*, 27 (1), 102–109, 2016.
7. Xiaoyu Hu, Fang Huang, **Magdalena Szymusiak**, Xuebi Tian, Ying Liu, Zaijie Jim Wang, PLGA-Curcumin Attenuates Opioid-Induced Hyperalgesia and Inhibits Spinal CaMKII α , *PLoS ONE* 11(1): e0146393. doi:10.1371/journal.pone.0146393.
8. **Magdalena Szymusiak**, Xiaoyu Hu, Paola A. Leon Plata, Paulina Ciupinski, Zaijie Jim Wang, and Ying Liu, Bioavailability of Curcumin and Curcumin Glucuronide in the Central Nervous System of Mice after Oral Delivery of Nano-curcumin, *International Journal of Pharmaceutics*, 2016, doi:10.1016/j.ijpharm.2016.07.027
9. **Magdalena Szymusiak**, Hanying Luo, Joseph Kalkowski, Weifeng Shang, Thomas Irving, Margarita Herrera-Alonso and Ying Liu, Small-Angle X-ray Scattering Measurements of Polymeric Micelles Formed from Novel Amphiphilic Brushes, *in preparation*.